Space Charge Effects in Energy Recovery Linacs

Raumladungseffekte in energierückgewinnenden Beschleunigern
Zur Erlangung des Grades eines Doktors der Naturwissenschaften (Dr. rer. nat.)
genehmigte Dissertation von Aamna Khan aus Nabha, Indien
Tag der Einreichung: 11.09.2019, Tag der Prüfung: 25.11.2019
Darmstadt — D 17

1. Gutachten: Prof. Dr. Oliver Boine-Frankenheim
2. Gutachten: Prof. Dr. Kurt Aulenbacher

TECHNISCHE UNIVERSITÄT DARMSTADT

Fachbereich Elektrotechnik und Informationstechnik
Institut für Teilchenbeschleunigung und elektromagnetische Felder

Space Charge Effects in Energy Recovery Linacs
Raumladungseffekte in energierückgewinnenden Beschleunigern

Genehmigte Dissertation von Aamna Khan aus Nabha, Indien

1. Gutachten: Prof. Dr. Oliver Boine-Frankenheim
2. Gutachten: Prof. Dr. Kurt Aulenbacher

Tag der Einreichung: 11.09.2019
Tag der Prüfung: 25.11.2019

Darmstadt — D 17

Erklärung zur Dissertation

Hiermit versichere ich, die vorliegende Dissertation ohne Hilfe Dritter und nur mit den angegebenen Quellen und Hilfsmitteln angefertigt zu haben. Alle Stellen, die aus Quellen entnommen wurden, sind als solche kenntlich gemacht. Diese Arbeit hat in gleicher oder ähnlicher Form noch keiner Prüfungsbehörde vorgelegen.

Darmstadt, den 11.09.2019

(Aamna Khan)

Kurzfassung

Die jüngsten technologischen Fortschritte bei energierückgewinnenden Linearbeschleunigern (Energy Recovery Linear Accelerators, ERLs) haben es uns ermöglicht, auf hochenergetische und hochintensive Elektronenstrahlen zuzugreifen, wodurch wir enorme Einblicke in die Grundlagen der Physik gewinnen und gleichzeitig vielfältige und robuste Anwendungen für Elektronenstrahlen entwickeln können. ERLs sind rezirkulierende Linearbeschleuniger, die Elektronenstrahlen von hoher Qualität erzeugen, deren Energie bei mehreren Durchgängen durch einen supraleitenden Beschleuniger-Resonator erhöht wird. Nachdem der vollbeschleunigte Strahl seine Interaktion, z.B. mit einem internen Target, abgeschlossen hat, werden die Elektronen im Linearbeschleuniger wieder abgebremst und übertragen ihre Energie zurück auf die Hochfrequenzfelder im Hohlraumresonator. Mit zunehmender Strahlintensität beeinflussen jedoch kollektive Effekte wie die Raumladung die Strahlqualität erheblich. Die Raumladung verändert die Elektronenstrahldynamik in dispersiven Bereichen entlang der strahlführenden Elemente. Darüber hinaus kann die longitudinale Raumladung zusammen mit der Dispersion zu einer Verstärkung des anfänglichen Schrotrauschens durch Dichtemodulation entlang der Strahlführung führen. Dies wird als Microbunching-Instabilität bezeichnet.

In den letzten zwei Jahrzehnten wurde die Microbunching-Instabilität in Speicherringen und Linearbeschleunigern intensiv untersucht. Aufgrund der zunehmenden Komplexität der Maschinenkonfiguration von ERLs im Vergleich zu Linacs muss jedoch die bestehende Analyse der Microbunching Instabilität erweitert werden, um die hohe Intensität des Elektronenstrahls in einem ERL unter durch Raumladung veränderter Dispersion mit zu berücksichtigen.

Diese Dissertation konzentriert sich auf die theoretische Untersuchung der Strahlanpassung mit Raumladung und der raumladungsinduzierten Microbunching-Instabilität in den Rezirkulationsbögen eines ERL. Es wird gezeigt, dass Strahl -Enveloppen und -Dispersion entlang der Rezirkulationsbögen eines ERL, einschließlich der Raumladungskräfte, angepasst werden können, um den Strahl an die Parameter der nachfolgenden HF-Struktur anzupassen. Es wird auch gezeigt, dass die durch Raumladungs modifizierte Dispersion ei-

ne Schlüsselrolle bei der Anpassung der des Momentum Compaction Faktors, sowohl für den isochronen als auch für den nicht-isochronen Rezirkulationsmodus eines ERL, spielt.

Ein Matrix-Ansatz, jedoch unter Berücksichtigung der transversal - longitudinalen Kopplung, wird zur Anpassung mit Raumladung und zur Berechnung der Instabilitätsverstärkung durch Microbunching verwendet. Der Strahlmatrixansatz wird mit Teilchen-Tracking Simulationen verglichen. Für eine qualitative Analyse wird gezeigt, dass man die Approximation der glatten Fokussierung verwenden kann, jedoch mit Längs-Quer-Kopplung. In diesem vereinfachten Modell wird die Skalierung der durchschnittlichen Dispersion, des Momentum Compaction Faktors und der Impulsabweichung unter Berücksichtigung der Raumladung untersucht.

Als Beispiel wird das obige Modell auf die Rezirkulationsbögen des mehrfach rezirkulierenden Mainzer Energy-recovery Superconducting Accelerator (MESA) angewandt, der einen kontinuierlichen Elektronen Strahl mit einer Strahlenergie von 105 MeV für physikalische Experimente mit einem pseudo internen Target bereitstellen soll. Zunächst wird ein niederenergetischer (5 MeV), 180° Injektionsbogen, der auch als Bunch-Kompressor arbeitet, an die nachfolgende erste HF-Struktur des geplanten MESA angepasst. Anschließend werden Start-to-End Simulationen entlang der strahlführenden Elemente von MESA mit Raumladung durchgeführt. Schließlich werden Einschränkungen der Strahlintensität durch Raumladungseffekte analysiert und Modelle zur Umgehung dieser Limitierungen implementiert.

Abstract

Recent technological advances in energy recovery linear accelerators (ERLs) have enabled us to access high energy and high brightness electron beam, allowing us to gain tremendous insights into fundamental physics while also envisioning diverse and robust applications for electron beams. ERLs are recirculating linacs that generate high quality electron beams, with these beams, energy is gained via multiple passes through a superconducting accelerating cavity. After the fully accelerated beam completes its interaction, for example, with an internal target, the electrons are decelerated in the linac, transferring their energy back to the cavity radio-frequency (RF) fields. However, as the beam brightness is increased, collective effects such as space charge considerably affect the beam quality. Space charge modifies the electron beam dynamics in dispersive regions along the beamline. Further, longitudinal space charge together with dispersion can lead to the amplification of the initial shot noise by density modulation along the beamline. This is known as microbunching instability.

In the past two decades, the microbunching instability has been intensively studied for storage rings and linac-based facilities. However, due to the increased intricacy of the machine configuration of ERLs compared to linacs, the existing microbunching instability analysis needs to be extended to maintain the high brightness of the electron beam in an ERL where space-charge-modifies the dispersion.

This dissertation focuses on the theoretical investigation of beam matching with space charge and space-charge-induced microbunching instability in the recirculation arcs of an ERL. It is shown that beam envelopes and dispersion along the recirculation arcs of an ERL, including space charge forces, can be matched to adjust the beam to the parameters of the subsequent RF structure. It is also shown that the space-charge-modified dispersion plays a key role in the adjustment of the momentum compaction required for both the isochronous and the non-isochronous recirculation mode of an ERL.

A coupled transverse-longitudinal beam matrix approach is used for matching with space charge and computing microbunching instability gain. The

beam matrix approach is compared with particle tracking simulations. For a qualitative analysis, it is shown that one can use the smooth focusing approximation but with longitudinal-transverse coupling. Within this simplified model, the scaling of average dispersion, momentum compaction, and momentum deviation with space charge is investigated.

As an example case, the above model is applied to the recirculation arcs of the multi-turn Mainz Energy-recovering Superconducting Accelerator (MESA), so as to deliver a continuous wave beam at 105 MeV for physics experiments with a pseudo-internal target. Initially, a low-energy (5 MeV), 180° injection arc, which also works as a bunch compressor, is matched to the subsequent first RF structure of the projected MESA. Then, start to end simulations along the MESA beamline with space charge are conducted. Finally, limitations on beam intensity due to space charge effects are analyzed and models to circumvent these limitations are implemented.

Contents

1 Introduction

Particle accelerators have long been employed as resourceful tools for science and technology. They are used to probe the most fundamental questions about the fundamental forces of nature and the basic building blocks of matter. Apart from applications in basic and applied sciences, they are also used to address security, environmental, medical and energy-related concerns. Traditionally, circular and linear accelerators have been employed for these applications. Over the years, these have increasingly been used to accelerate particles with time-varying radio-frequency (RF) fields.

One of the main advantages of a circular particle accelerators like the storage ring and its variants is the ability to store particles without acceleration for various applications. However, because of existence of equilibrium state between radiation damping and quantum excitation, there is a limit on the obtainable beam intensity, emittance and beam quality [1]. Therefore, in a circular machine, beam properties are independent of the electron source or any pre-accelerator.

One of the main advantages of the linear accelerator (linac) is its potential to produce high-energy, and high-intensity charged-particle beams of high brilliance. High brilliance means highly efficient production of beams with small beam radii and momentum deviation [2]. In a linac, there is no power loss because of synchrotron radiation as a beam travels in a straight line, unlike high-energy electron beams in circular accelerators. Because of a single pass, there is also no equilibrium state that needs to be achieved. Therefore, in a linac, all beam properties depend on the low-energy electron source and are well preserved during acceleration. However, linacs are limited to achieving a small average beam current because of the expensive RF power required for high energy acceleration.

An energy recovery linac (ERL) is a powerful alternative for generating brilliant electron beams by combining the best of storage rings and linacs, such as high current and energy of storage rings and high beam quality of a linac. ERLs are an emerging generation of electron accelerators with the potential of high beam power in continuous wave (CW) operation at moderate operational costs as compared to linacs. They are set up as recirculating linacs, allow-

ing for multiple passes through superconducting accelerating cavities. After the experimental use of the fully accelerated beam, the electrons are decelerated in the linac, transferring their energy back to the cavity RF fields. The recovery of beam energy can yield a high energy efficiency of ERLs. Several high-current, high-brilliance ERL facilities with short pulses have been recently proposed for various applications, for example, to achieve high optical beam power in free-electron laser sources; advancement of photon brilliance in light sources; electron cooling devices that would benefit from both high average current and good beam quality; or, possibly, as the electron accelerator in an electron-ion collider intended to achieve an operating luminosity beyond that provided by existing, storage-ring-based-colliders [3, 4, 5]. Some ERL facilities around the world are JLab IR FEL Upgrade, JAEA FEL, Novosibirsk High Power THz FEL, cERL, BERLinPro, CBETA, PERLE, and MESA [6].

This dissertation focuses on addressing the intensity limitation due to space charge effects in an intermediate energy (few MeV) ERL. For example, beam matching with space charge of an arc of an ERL to the subsequent RF structure is found to be necessary to maintain beam quality [7]. On the other hand, longitudinal space charge together with dispersion can lead to the amplification of the initial shot noise by density modulation along the beamline, also known as microbunching instability [8, 9]. This chapter enlightens the reader with the history and background of ERLs, and their applications in section 1.1. Challenges related to the lattice and the beam dynamics in an ERL are discussed in section 1.2 followed by the short introduction of the Mainz Energy-recovering Superconducting Accelerator (MESA) project in section 1.3. Finally, a brief overview of this dissertation is described in section 1.4.

1.1 Energy Recovery Linacs

The idea of an ERL was first proposed in 1965 by M. Tigner [10] for application in a collider, and has gained tremendous interest since the 21st century due to the development of superconducting RF (SRF) linacs, which are ideal for the energy recovery process because of their low loss rates. Figure 1.1 shows a simplified outline for a generic single turn ERL. The electron source generates a high brightness electron beam and injects it into the linac with a selective RF phase at energy E_{in} for acceleration during the first pass. To decelerate the beam during the second pass through the linac, the recirculation path must be equal to an integer plus half the RF wavelength, which means that there is an RF phase difference of 180° between the first and second pass. Thus only a low energy beam ($E_{\text{out}} = E_{\text{in}}$) go to the beam dump.

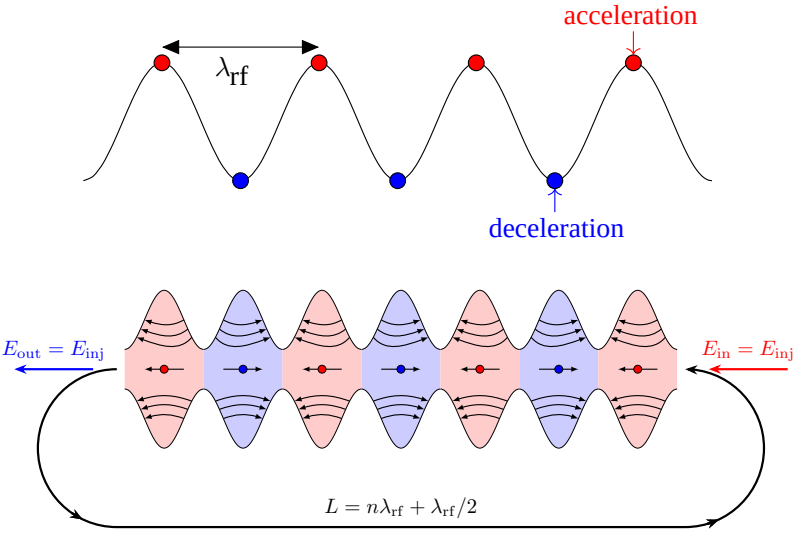

Figure 1.1.: Schematic view of an energy recovery linear accelerator. If the beam enters on the crest of the RF field (red dot), there is energy transfer from the cavities to the beam. If the beam enters on the trough of RF fields (blue dot), there is energy transfer from the beam to the cavity RF field. Here E_{in} and E_{out} are the injection and exit beam energy, E is the total beam energy, ΔE is the energy gain through the linacs, λ_{rf} is the RF wavelength, L is the recirculation arc length, β is the relativistic factor, and n is an integer.

In an ERL beam loading effects of the accelerated beam are cancelled by the decelerated beam. In other words, during the recirculation loop within cavities, energy transfers directly, via the RF field, from the decelerating beam to the accelerating beam. Thus, an ERL can accelerate a high average current with only a moderate amount of RF power as compared to a linac. Since ERLs are single or few multi-turn machines, inevitable intensity limitation due to equilibrium state of storage rings is not relevant here, as the passage time is much too short to reach equilibrium. Further, an electron source determines the beam quality in an ERL, which makes ERL upgrades much easier than conventional circular and linear machines. ERLs have the potential to overcome beam quality limitations of third-generation light sources based on modern

storage rings by using high brightness electron sources that are established on laser-induced photoemission from a cathode gun. The combination of high average current, higher flexibility in interaction region design and flexible modes of operation, for example, high brilliance, short pulse and different pulse patterns makes the ERL a versatile machine [3, 11]. Moreover, ERL beam dump designs are much simpler and safer because the beam energy at the dump is low.

1.2 Challenges in Energy Recovery Linacs

Energy recovery linacs are of growing interest as they overture the potential to boost the science limits farther than the modern storage rings and linacs. However, ERLs are not free from their construction, technical or scientific challenges. Depending upon the machine beam optics, beam energy, recirculations and target beam parameters, several challenges arise in various parts in design and operation of an ERL. For example, there are several proposed and under construction ERL facilities with multi-turn recirculation and split linac to achieve the high energy at a reasonable cost [6, 12, 13, 14]. The advantages of using split linacs is its ability to achieve the lower peak envelopes due to a short linac and relatively stronger focusing on higher passes because of the higher injection energy at the entrance of the second linac [15]. However, it comes with the cost of a complex magnetic set up with the multi-recirculation arcs [16, 17]. Also, advances in technology have allowed phenomenal increases in beam energy and beam brightness in an ERL for fundamental physics research and various accelerator applications. However, as the beam intensity is increased, collective effects due to the beam-induced forces turn into increasingly significant.

The goal of an ERL design is to preserve the high beam quality and brilliance delivered from the particle source throughout the machine. Therefore, emittance growth and beam loss should be well controlled to achieve the required efficiency of the energy recovery process [3, 6, 18].

High bunch charge coupled with relatively low initial energy and final energy (few MeV) implies that both transverse and longitudinal space charge needs to be considered throughout the machine. Particularly, current dependent matching of an arc into subsequent RF structure is essential to preserve beam quality. It is found that at low energy space-charge-modified dispersion plays a key role for the adjustment of the momentum compaction required for both the isochronous and the non-isochronous recirculation mode of an ERL,

which also affects the efficiency of the energy recovery process [7]. Space-charge-induced distortions of beam envelopes in ERLs have been discussed in [19, 20].

The studies of microbunching instability induced by longitudinal space charge and coherent synchrotron radiation have been an interesting research area, particularly with emphasis on the design of magnetic bunch compressors for short-wavelength free electron lasers or linear colliders, and recirculation arcs of ERLs [8, 21, 22]. Microbunching instability acts like a high-gain klystron-like amplifier [23, 24, 25]. In high intensity electron beams a small amount of density modulation can create longitudinal self-fields that lead to beam energy modulation. A recirculation arc with bends introduces the path length dependence on energy. Because of this dependence, energy modulations convert to additional density modulations much larger than the initial density modulations, which can degrade beam quality in high intensity accelerators [26]. Coherent synchrotron radiation is not prominent in low energy ERLs like MESA (discussed in section 1.3). Therefore, our study is focused only on space-charge-induced microbunching instability in ERLs.

In this dissertation, a coupled transverse-longitudinal beam matrix approach is used for beam matching with space charge and to compute space-charge-induced microbunching instability gain. The beam matrix approach is compared with particle tracking simulations using ELEGANT [27]. The present work is applied to the MESA project to investigate the space charge effects in ERLs.

1.3 The MESA Project

MESA is a small-scale, multi-turn, double-sided recirculating linac with vertical stacking of the return arcs operating in CW mode under construction at the Johannes Gutenberg-Universität Mainz. MESA will recirculate multiple beams of different energies around the split linac at one time. MESA project was first proposed in 2009 [28], and it has continuously undergone through several changes in the lattice layout and experiments requirements [29, 30]. An overview of the proposed MESA facilities is shown in Fig. 1.2. The electron source of MESA will provide up to 1 mA of polarized beam at 100 keV in the first experimental stage of MESA. In the next planned stage it will be upgraded to provide 10 mA of unpolarized beam current. This electron source is followed by a spin manipulation system containing two Wien filters. A chopper and two buncher cavities prepare the bunches for the normal-conducting milliampere

booster (MAMBO), which accelerates them to 5 MeV. All RF devices of MESA operate at 1.3 GHz or higher harmonics.

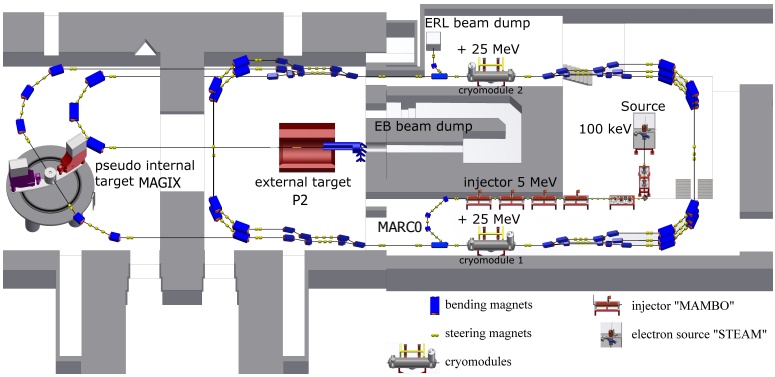

Figure 1.2.: A schematic layout of MESA.

In MESA electrons will be accelerated by two ELBE-type [31] RF structures each housing two superconducting TESLA-type cavities with an accelerating gradient of 12.5 MeV/m, which results in energy gain of 25 MeV per pass. Figure 1.3 shows the beam energy along the MESA beamline after each pass through the RF structures. There are four spreader sections for separating and recombining the beam and two chicanes for injection and extraction of the 5 MeV beam.

MESA is planned to operate in two modes: external beam (EB) mode and energy-recovery (ER) mode. In EB mode, the electron beam will gain 155 MeV with up to 150 μA beam current by circulating thrice around the accelerator. The beam is planned to be used for high-precision fixed-target experiments. The main experiment in the EB mode will be the measurement of the electroweak mixing angle at the P2 setup [32]. Similarly in ER mode, the electron beam will gain 105 MeV with 1(10) mA beam current by circulating twice around the accelerator. The main experiments in the ER mode will be pseudo-internal target (PIT) experiments in a search for dark photons with high luminosity [33]. In ER mode, 100 MeV of the beam energy can be recovered by decelerating the beam in the superconducting cavities. Further bunches are accelerated using this recovered energy [4]. Both operational modes demand high beam quality and stability. Mainly, a low momentum deviation is required to achieve higher precision of experiments. The prerequisite for sustaining beam quality is proper beam transport through the injection arc

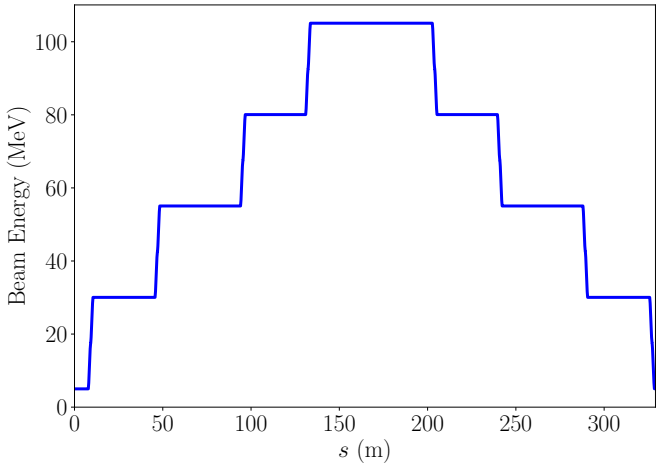

Figure 1.3.: Beam energy profile along the MESA beamline.

Parameters [unit]	Symbol	value
Initial beam energy [MeV]	E_{in}	5
RF frequency [GHz]	f_{rf}	1.3
Current [mA]	I	1/10
Initial beta functions [m]	β_{x0}, β_{y0}	1.30, 0.90
Initial alpha functions	α_{x0}, α_{y0}	−0.17, −0.57
Initial rms momentum deviation [%]	σ_δ	0.01 / 0.4
Initial half bunch length [ps]	z_m	4.2
Final beta functions [m]	β_x, β_y	1.57, 1.57
Final alpha functions	α_x, α_y	0.12, 0.12
Normalized emittance [π mm mrad]	$\epsilon_{nx,ny}$	2/6
Momentum compaction [m]	R_{56}	0.14

Table 1.1.: Beam parameters at the injection arc of MESA.

(MARC0), which will be discussed in chapter 5. The proposed beam parameters for MESA are listed in Table 1.1.

In this dissertation, our discussions will be limited to the ER mode, wherein the beam passes each cavity four times (two times for acceleration and two

times for declaration) and then goes to 5 MeV beam dump. The advantage of the PIT in an ERL is that high luminosity is achievable at low energies, which is impractical at storage rings because of inevitable emittance growth. The single pass ER-mode operation at MESA degenerates the beam emittance only negligibly, hence providing optimized background conditions during the PIT experiment. This allows for searching low rate processes, for instance, the production of new hypothetical particles, e.g. “dark photons” [16].

1.4 Overview of the Dissertation

The dissertation is organized as follows: the fundamentals of charged beam dynamics starting from single particle dynamics to multi-particle dynamics and then general matrix formalism which is used throughout the thesis are explained in chapter 2. Chapter 3 discusses the beam intensity effects of space charge and microbunching instability in ERLs and the analytical and numerical methods used to study them. In chapter 4, we discuss simulations tools used in this dissertation. A beam matrix model with space charge is briefly discussed, referred to as “beam matrix approach” throughout the dissertation and compared with ELEGANT particle tracking simulations. Results and parameter adjustments for beam matching with the space charge from the MESA injection arc (MARC0) into the first RF structure are discussed in chapter 5 followed by the application chapter 6 with the intensity limitations in MESA. Finally, the results of this dissertation are briefly summarized in chapter 7.

2 Fundamentals

This chapter presents the fundamentals of charged particle beam dynamic in an ERL required as a prerequisite for the following chapters. The chapter starts with section 2.1, which gives a brief description of single and multi-particle beam dynamics in an ERL. The general matrix formalism for a number of individual components of an ERL beamline is discussed to describe the coupled first-order dynamics of particles. Further, it is outlined how a dispersive beamline plays an important role in a bunch compressor section of an ERL in section 2.2.

2.1 Beam Dynamics in Energy Recovery Linacs

The main goal of beam dynamics is to describe the precise motion of charged particles under the influence of electromagnetic fields in the particle accelerators. The motion of a charged particle of charge q, rest mass m moving with velocity $\vec{v}$ in an electromagnetic field is described by the Lorentz force $\vec{F}$:

$$\vec{F} = \frac{\mathrm{d}\vec{p}}{\mathrm{d}t} = q\left(\vec{E} + \vec{v} \times \vec{B}\right), \tag{2.1}$$

where $\vec{p} = \gamma m \vec{v}$ is the relativistic momentum. c is the speed of light in vacuum. $\beta = v/c$ and $\gamma = 1/\sqrt{1-\beta^2}$ are the relativistic factor.

Here, the electric field strength $\vec{E}$ and magnetic flux density $\vec{B}$ can be represented in terms of scalar potential ϕ and vector potential $\vec{A}$ as follows:

$$\vec{E} = -\nabla\phi - \frac{\partial \vec{A}}{\partial t}, \quad \vec{B} = \nabla \times \vec{A}.$$

A charged particle accelerates or decelerates by interacting with an $\vec{E}$ field and moves in a circular trajectory under the influence of magnetic field $\vec{B}$ because

the magnetic part of $\vec{F}$ is perpendicular to both $\vec{v}$ and $\vec{B}$. In particular, when $\vec{B}$ is perpendicular to $\vec{v}$ the following relation is satisfied:

$$B\rho = \frac{p}{q}, \tag{2.2}$$

where ρ is the radius of curvature. $B\rho$ is known as magnetic rigidity. It measures the angular deflection of a charged particle passing through a magnetic field. For a specific magnetic field, the greater is the momentum of a particle, the less it will be deflected and vice versa. Thus, the bending radius for different energy recirculation arcs of an ERL is computed using Eq. (2.2).

In a particle accelerator, the magnets, RF cavities, and other components of the machine are positioned along the reference trajectory with design momentum p_0. Here, reference trajectory is the ideal 'design' trajectory followed by a charged particle as it moves along the beamline. But due to various errors, such as misalignment errors, momentum errors, field errors, fringe fields, and so on, the particles do not follow the reference trajectory. Thus, it is convenient to use a co-moving coordinate system (x, y, s) for beam dynamic studies. Note that here (x, y, z) are the local coordinates of a particle relative to the reference trajectory. Here, coordinates x and y are the horizontal and vertical coordinates, respectively, in a plane perpendicular to independent variable s at any point along the beamline, and z is the longitudinal coordinate as shown in Fig. 2.1.

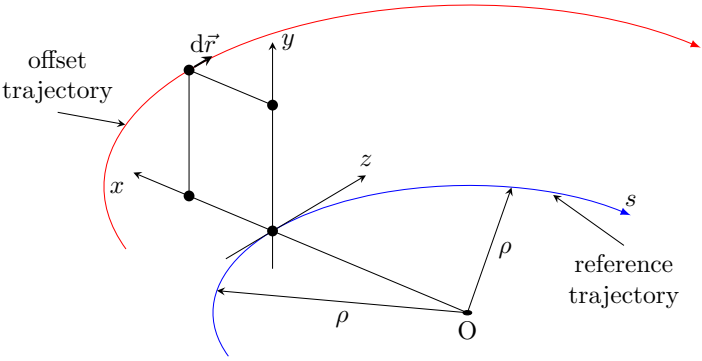

Figure 2.1.: Co-moving coordinate system in an accelerator.

For systems with very small beam sizes and rather uniform electromagnetic fields, it is sufficient to account only for the first-order transport maps. In such cases, the system can be modeled by means of linear algebra which allows to perform complicated analysis at low computational costs. Thus in this dissertation, the discussions will be limited to linear beam dynamics only. In subsection 2.1.1, the general matrix formalism to solve Hamilton's equation and the symplectic conditions are discussed. For simplicity, we shall consider a curvature of the reference trajectory in the horizontal plane. Subsection 2.1.2 explains the single-particle transverse equations of motion. The definitions of Twiss parameters, and emittance and how to apply the general matrix formalism to a multi-particle beam are discussed in subsection 2.1.3. The basic relations for the beam centroid, rms beam size, and path length in the presence of dispersion, and second moments of beam distribution are explained in subsection 2.1.4. Finally, the longitudinal equations of motion for a dispersive beamline with coupling to the transverse plane are given in subsection 2.1.5.

2.1.1 General Matrix Formalism

The single-particle dynamics in a co-moving coordinate system can be described in terms of six-dimensional phase space coordinate

$$\mathbf{x} = \left(x, x', y, y', z, \delta\right),$$

whose components are the beam dynamical variables. Here, $x' = dx/ds$, $y' = dy/ds$ denote the transverse angular deflections which are the derivatives of x and y with respect to distance s along the particle trajectory, respectively, $\delta = \left(p - p_0\right)/p_0$ is the relative momentum deviation of a particle moving with the offset momentum p with respect to the reference momentum p_0, and $z = s - \beta ct$ is the local longitudinal bunch coordinate of a particle with respect to the reference particle. The first-order evaluation of the 6-dimensional phase space coordinate from $s = s_\mathrm{i}$ to $s = s_\mathrm{f}$ can be written in the following matrix equation

$$\mathbf{x}(s_\mathrm{f}) = \mathbf{R}\left(s_\mathrm{i} \rightarrow s_\mathrm{f}\right)\mathbf{x}(s_\mathrm{i}), \tag{2.3}$$

where $\mathbf{R}$ is a 6×6 transport matrix from the initial point (index i) to the final point (index f) along a beamline. A transport matrix is simply a relationship between the dynamical variables for a particle at different positions along a beamline. An important property of matrix formalism is that repeated multiplication of the transport matrices of individual beamline components compute

the trajectory of a single particle through an accelerator beamline. For an arbitrary n number of transport elements in a beamline, each with a constant but different focusing gradient, transport matrix is obtained as:

$$\mathbf{R}\left(s_n|s_0\right) = \mathbf{R}\left(s_n|s_{n-1}\right)...\mathbf{R}\left(s_3|s_2\right)\mathbf{R}\left(s_2|s_1\right)\mathbf{R}\left(s_1|s_0\right). \tag{2.4}$$

The first-order transport matrix $\mathbf{R}$ for each beamline element can be obtained analytically using the Hamiltonian of a charged particle system under the paraxial approximation. Here, paraxial approximation is the truncation of a power series expansion of the Hamiltonian at low order in horizontal and vertical momenta. The advantage of using Hamiltonian mechanics is that it makes possible to use of the conserved quantities that arise in Hamiltonian systems to develop powerful techniques for the study of the charged particle dynamics in accelerator beam lines. The explicit expression of Hamiltonian for a particle moving in a co-moving coordinate system is (see also [34]):

$$H = -\left(1+\frac{x}{\rho}\right)\sqrt{\left(\delta+\frac{1}{\beta}-\frac{q\phi}{cp_0}\right)^2-\left(x'-\frac{qA_x}{p_0}\right)^2-\left(y'-\frac{qA_y}{p_0}\right)^2-\frac{1}{\beta^2\gamma^2}} + \frac{\delta}{\beta}-\left(1+\frac{x}{\rho}\right)a_s. \tag{2.5}$$

Here, A_x and A_y are the horizontal and vertical components of the vector potential, respectively, and a_s is the component of the vector potential in the direction of increasing of s. The momenta x' and y' are given by:

$$x' = \frac{\gamma_0 m\dot{x}+qA_x}{p_0}, \quad y' = \frac{\gamma_0 m\dot{y}+qA_y}{p_0},$$

where $\dot{x}$ and $\dot{y}$ are the derivatives of x and y with respect to time t.

Hamilton's equations of motion for the six-dimensional phase space coordinate $\mathbf{x}$ can be written as

$$\frac{\mathrm{d}\mathbf{x}}{\mathrm{d}s} = \mathbf{S}\frac{\partial H}{\partial \mathbf{x}}. \tag{2.6}$$

Here, $\mathbf{S}$ is the 6×6 antisymmetric matrix:

$$\mathbf{S} = \begin{pmatrix} 0 & 1 & 0 & 0 & 0 & 0 \\ -1 & 0 & 0 & 0 & 0 & 0 \\ 0 & 0 & 0 & 1 & 0 & 0 \\ 0 & 0 & -1 & 0 & 0 & 0 \\ 0 & 0 & 0 & 0 & 0 & 1 \\ 0 & 0 & 0 & 0 & -1 & 0 \end{pmatrix}. \tag{2.7}$$

Substituting the electromagnetic potentials in a particular element of beamline into the Hamiltonian Eq. (2.5) allows us to write down the equations of motion for a charged particle moving through that element. Linear approximations to nonlinear dynamical systems can be made in a number of different ways. Substituting a second-order Hamiltonian into Hamilton's equations (Eq. (2.6)) produces linear equations of motion. The advantage of this approach is that although we have made an approximation to the system, but still the dynamics can be described using a Hamiltonian. The solution therefore retains properties (in particular, the existence of conserved quantities) that prove to be very useful when investigating particle dynamics in accelerator beam lines. The transport matrices for the typical beamline elements in an ERL, for example, drift, quadrupole, bending dipole, and RF cavity are summarized as follows. For detailed derivations, see Refs. [34, 35].

The transport matrix $\mathbf{R}_{\text{drift}}$ for a drift space of length L:

$$\mathbf{R}_{\text{drift}} = \begin{pmatrix} 1 & L & 0 & 0 & 0 & 0 \\ 0 & 1 & 0 & 0 & 0 & 0 \\ 0 & 0 & 1 & L & 0 & 0 \\ 0 & 0 & 0 & 1 & 0 & 0 \\ 0 & 0 & 0 & 0 & 1 & \dfrac{L}{\beta^2\gamma^2} \\ 0 & 0 & 0 & 0 & 0 & 1 \end{pmatrix}. \tag{2.8}$$

In an accelerator beamline, a dipole magnet produces a constant magnetic field that can be used to bend the particle trajectory. A dipole magnet is also referred as a weak focusing magnet. Consider a horizontal sector dipole magnet with horizontal focusing gradient $\kappa_x = 1/\rho^2$, vertical focusing gradient $\kappa_y = 0$. The transport matrix $\mathbf{R}_{\text{SB}}$ for such a sector dipole in which entrance and exit angles are perpendicular to the edge of the dipole field:

$$\mathbf{R}_{\mathrm{SB}} = \begin{pmatrix} c_{dx} & \rho s_{dx} & 0 & 0 & 0 & \frac{\rho}{\beta}(1-c_{dx}) \\ -\frac{s_{dx}}{\rho} & c_{dx} & 0 & 0 & 0 & \frac{s_{dx}}{\beta} \\ 0 & 0 & 1 & L & 0 & 0 \\ 0 & 0 & 0 & 1 & 0 & 0 \\ -\frac{s_{dx}}{\beta} & -\frac{\rho}{\beta}(1-c_{dx}) & 0 & 0 & 1 & \frac{L}{\beta^2\gamma^2} + \rho s_{dx} - L \\ 0 & 0 & 0 & 0 & 0 & 1 \end{pmatrix}, \tag{2.9}$$

where $c_{dx} = \cos\theta$, and $s_{dx} = \sin\theta$, $\theta = L/\rho$, ρ is the bending radius and L is the arc length of the dipole. Transport matrix in Eq. (2.9) describes the dynamics of a particle that moves entirely within the field of the sector dipole.

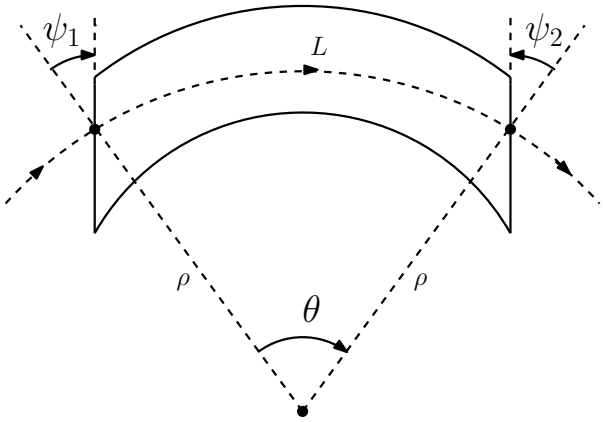

Figure 2.2.: Rotation angles of entrance and exit faces in a dipole magnet. If the pole face rotation angles are $\psi_1 = \psi_2 = 0$, then it is a sector dipole and the reference trajectory at the entrance and exit of the magnet is perpendicular to the pole face. If the pole faces angles are $\psi_1 = \psi_2 = \theta/2$, then it is a rectangular dipole and the pole faces are parallel. Here θ is the total bending angle of the reference trajectory in the dipole.

In a dipole the field cannot change abruptly from zero to the nominal dipole field, but must rise and fall smoothly over some distance at the entrance and at the exit of a dipole magnet, respectively. There are significant effects associated

with the edge focusing that a particle sees as it enters and exits a dipole. These effects can be described as horizontal and vertical focusing (or defocusing) in a linear approximation. The strength of these effects depends on a variety of factors, including the main field of the dipole, the extent of the edge field, and the angle of the entrance ψ_1 or exit ψ_2 face regarding the reference trajectory as shown in Fig. 2.2. If the pole faces angles are $\psi_1 = \psi_2 = \theta/2$, then it is a rectangular dipole in which the pole faces are parallel. Here θ is the total bending angle of the reference trajectory in a dipole.

The transport matrix $\mathbf{R}_{\text{edge}}$ for a dipole edge focusing:

$$\mathbf{R}_{\text{edge}} = \begin{pmatrix} 1 & 0 & 0 & 0 & 0 & 0 \\ k_0 \tan\psi_1 & 1 & 0 & 0 & 0 & 0 \\ 0 & 0 & 1 & 0 & 0 & 0 \\ 0 & 0 & -k_0 \tan\psi_1 & 0 & 0 & 0 \\ 0 & 0 & 0 & 0 & 1 & 0 \\ 0 & 0 & 0 & 0 & 0 & 1 \end{pmatrix}, \tag{2.10}$$

where $k_0 = qB_0/p_0$, p_0 is the reference momentum deviation, q is the particle charge, and B_0 is the magnetic strength. The edge focusing field has a focusing effect on a beam when the entrance face of a dipole is not perpendicular to the reference trajectory. The transport matrix $\mathbf{R}_{\text{bend}}$ for a dipole magnet with edge focusing is:

$$\mathbf{R}_{\text{bend}} = \mathbf{R}_{\text{edge}} \cdot \mathbf{R}_{\text{SB}} \cdot \mathbf{R}_{\text{edge}} \tag{2.11}$$

The horizontal (de)focusing effect of the dipole edge focusing is typically a geometric effect. When the entrance face of a dipole is rotated, the face is no longer perpendicular to the reference trajectory. Depending on the particle horizontal coordinate, a particle inside the dipole has to travel a longer or shorter distance. As a result, it changes the horizontal trajectory of the particle which also influences the particle path length or time of flight inside the dipole.

In an accelerator beam line, a quadrupole magnet imparts a force proportional to distance from the center which control the beam size by providing transverse focusing. A strong focusing quadrupole with $1/\rho = 0$ results in $\kappa = \kappa_x = -\kappa_y$. κ_x and κ_y are the horizontal and vertical focusing strengths, respectively. This concludes that a horizontally focusing quadrupole is also a vertically defocusing quadrupole and vice versa. The transport matrix $\mathbf{R}_{\text{QF}}$ for a vertical focusing quadrupole $\kappa_x > 0$ is:

$$\mathbf{R}_{\mathrm{QF}} = \begin{pmatrix} c_{qx} & \frac{1}{\sqrt{\kappa}} s_{qx} & 0 & 0 & 0 & 0 \\ -\sqrt{\kappa} s_{qx} & c_{qx} & 0 & 0 & 0 & 0 \\ 0 & 0 & c_{qy} & \frac{1}{\sqrt{\kappa}} s_y & 0 & 0 \\ 0 & 0 & \sqrt{\kappa} s_y & c_{qy} & 0 & 0 \\ 0 & 0 & 0 & 0 & 1 & \frac{L}{\beta^2\gamma^2} \\ 0 & 0 & 0 & 0 & 0 & 1 \end{pmatrix}, \tag{2.12}$$

where $c_{qx} = \cos\sqrt{\kappa}L$, $s_{qx} = \sin\sqrt{\kappa}L$, $c_{qy} = \cosh\sqrt{\kappa}L$, and $s_{qy} = \sinh\sqrt{\kappa}L$. The horizontal and vertical matrix blocks will exchange in Eq. (2.12) for a horizontally focusing quadrupole $\kappa_x < 0$.

In an accelerator beamline, the RF cavities produce time-dependent electromagnetic fields that control beam particles in several ways. For example, cavities can be used to accelerate or decelerate the particles within a bunch or to provide longitudinal focusing so that particles remain contained within a bunch or to provide transverse deflections dependent on the time when a particle arrives at the cavity. They are also used to modulate beam position or energy as a beam kicker. The transport matrix $\mathbf{R}_{\mathrm{rf}}$ based on a cylindrical cavity operating in the TM_{010} mode is [34]:

$$\mathbf{R}_{\mathrm{rf}} = \begin{pmatrix} c_\perp & s_\perp & 0 & 0 & 0 & 0 \\ -\omega_\perp^2 s_\perp & c_\perp & 0 & 0 & 0 & 0 \\ 0 & 0 & c_\perp & s_\perp & 0 & 0 \\ 0 & 0 & -\omega_\perp^2 s_\perp & c_\perp & 0 & 0 \\ 0 & 0 & 0 & 0 & c_\parallel & \frac{1}{\beta^2\gamma^2} s_\parallel \\ 0 & 0 & 0 & 0 & -\beta^2\gamma^2\omega_\parallel^2 s_\parallel & c_\parallel \end{pmatrix}. \tag{2.13}$$

The particular quantities appeared in transport matrix for $cos(\phi) > 0$ are:

$$c_\perp = \cos\left(\omega_\perp L\right), \quad s_\perp = \frac{\sin\left(\omega_\perp L\right)}{\omega_\perp}, \quad \omega_\perp = k\sqrt{\frac{\alpha\cos\phi}{2\pi}},$$

$$c_\parallel = \cos\left(\omega_\parallel L\right), \quad s_\parallel = \frac{\sin\left(\omega_\parallel L\right)}{\omega_\parallel}, \quad \omega_\parallel = \frac{k}{\beta\gamma}\sqrt{\frac{\alpha\cos\phi}{\pi}},$$

where $k = 2\pi/\beta\lambda_{\rm rf}$, $\alpha = qV_0/p_0c$, $\lambda_{\rm rf}$ is the RF wavelength, L is the cavity or cell length, ϕ is the phase, and V_0 is the peak cavity voltage. With $\cos\phi < 0$, the cosine and sine function in the transport matrix will change to hyperbolic cosine "cosh" and hyperbolic sine "sinh", respectively.

Dynamical systems that obey Hamilton's equation have an important property that the transport maps from one point to another are symplectic. One of the main reason for symplecticity is important is that symplectic transformations have conserved quantities associated with them. If a system satisfies the Hamilton's equations, then the following symplectic condition is also satisfied [34, 35]

$$\mathbf{R}^{\mathsf{T}}\mathbf{S}\mathbf{R} = \mathbf{S}. \tag{2.14}$$

Physically, symplectic matrices preserve areas in phase space. Using Eq. (2.14) and Eq. (2.7), the general constraints on the transport matrix elements are obtained:

$$R_{51} = R_{16}R_{21} - R_{26}R_{11}, \tag{2.15a}$$
$$R_{52} = R_{16}R_{22} - R_{26}R_{12}, \tag{2.15b}$$
$$R_{53} = R_{36}R_{43} - R_{46}R_{33}, \tag{2.15c}$$
$$R_{54} = R_{36}R_{44} - R_{46}R_{44}. \tag{2.15d}$$

It can be concluded from Eq. (2.15) that R_{56} has no constraint from the symplecticity condition. Therefore, it can be treated as a free parameter. Also, it is clear from Eq. (2.9) that R_{51} and R_{52} are non-zero in a horizontal dipole. Basically, these elements represent the variations in the path length depending on the horizontal trajectory. Because the field in a horizontal dipole is vertical, the bending of the trajectory is purely in the horizontal plane, and there is no vertical dispersion, the elements R_{36} and R_{46} are zero, and so are R_{53} and R_{54} (Eq. (2.15)).

2.1.2 Transverse Equations of Motion

Particles with transverse momentum deviations $(x', y') \neq 0$ need to be focused towards the reference trajectory to avoid the growth of a beamsize in x and y transverse plane. In a typical ERL beamline without RF elements, quadrupole magnets are used to provide the focusing and dipoles are used to bend the particles trajectories. The focusing force in a typical machine is a function of the local focusing strengths. Using a linear Hamiltonian for the co-moving

coordinate system [34], the linearized transverse equations of motion for a charged particle in the presence of external fields are (also referred as Hill's equations):

$$x'' + \kappa_x(s)\,x = \frac{\delta}{\rho(s)}, \quad \kappa_x = \frac{1}{\rho^2(s)} + K(s), \tag{2.16a}$$

$$y'' + \kappa_y(s)\,y = 0, \quad \kappa_y = -K(s), \tag{2.16b}$$

where $K(s)$ is the linearized focusing gradient, κ_x and κ_y are the horizontal and vertical focusing strengths, respectively, and ρ is the radius of curvature. $1/\rho^2$ is the weak focusing produced by the dipole fields. For simplicity, the bending is only assumed in the horizontal plane. The solution of Eq. (2.16) depends on the initial conditions $x(0), x'(0), y(0), y'(0)$ and $\kappa_{x,y}$. In paraxial approximation, it does not depend on the higher orders of $x(0)$, $x'(0)$, $y(0)$ and $y'(0)$ [35].

2.1.3 Twiss Parameters and Emittance

In terms of the action-angle variables, the phase space coordinates of a particle can be written [34]:

$$x(s) = \sqrt{2\beta_x J_x}\cos\phi_x, \tag{2.17}$$

$$x'(s) = -\sqrt{\frac{2J_x}{\beta_x}}\left(\sin\phi_x + \alpha_x\cos\phi_x\right). \tag{2.18}$$

Here, the action J_x is a variable that is used to describe the amplitude of the motion of a single particle:

$$2J_x = \left(\gamma_x x^2 + 2\alpha_x x x' + \beta_x x'^2\right), \tag{2.19}$$

where $\alpha_x(s), \beta_x(s)$, and $\gamma_x(s)$ are the Twiss parameters. The advantage of using action-angle variables is that, under symplectic transport, the action of a particle is constant. Similar equations hold for the vertical and longitudinal focusing.

Twiss parameters play an important role in the linear beam optics of charged particles beams. β_x is the betatron function, which describes the local ampli-

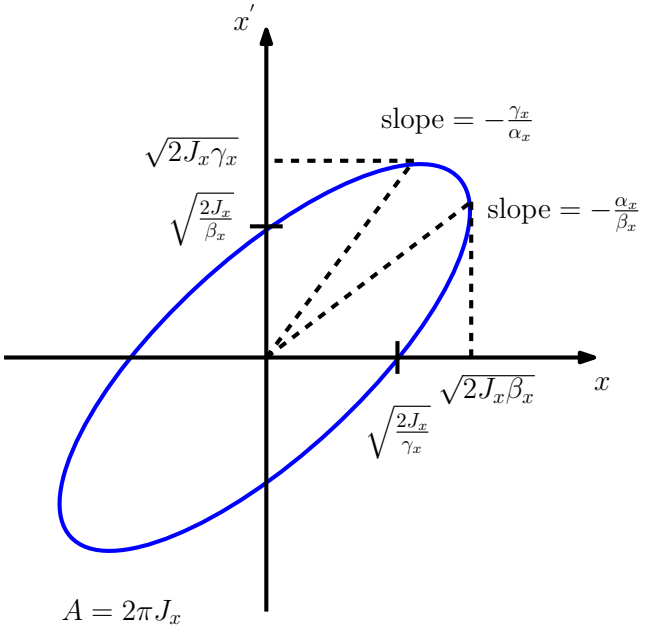

Figure 2.3.: Graphical representation of Twiss parameters. Any phase space ellipse can be defined by specifying: Area, shape and orientation. α_x is related to the beam tilt, β_x is related to the beam shape and size, J_x is related to the beam size and γ_x is dependent on α_x and β_x.

tude of betatron oscillation of the particles. Beta function $\beta_x(s)$, is determined exclusively by the lattice gradient $\kappa_x(s)$,

$$\frac{1}{2}\beta_x\beta_x'' - \frac{1}{4}\beta_x'^2 + \beta_x^2\kappa_x(s) = 1. \tag{2.20}$$

The other Twiss parameters are related to the beta function as follows

$$\alpha_x(s) = -\frac{1}{2}\beta_x', \quad \gamma_x(s) = \frac{1+\alpha_x^2}{\beta_x}. \tag{2.21}$$

$\phi_x(s)$ is the phase advance of the oscillation between point "0" to "s" in the beamline:

$$\phi_x(s) = \int_0^s \frac{\mathrm{d}s}{\beta_x(s)}. \tag{2.22}$$

In a real machine, there is rarely any information about a single-particle because a beam is usually a collection of particles distributed in the phase space. Therefore, we parameterize the entire particle distribution, and write the equations for the parameters. Thus we can write transport equations for the whole beam, not just for single particle. For a symplectic system, a good approximation for the beam shape in phase space is an ellipse. Any phase space ellipse can be defined by specifying: Area, shape and orientation as shown in Fig. 2.3. α_x is related to the beam tilt, β_x is related to the beam shape and size, J_x is related to the beam size and γ_x dependent on α_x and β_x. For a multi-particle bunch, we are interested in the evolution of particle distribution function $f(x, x', y, y', \delta, s)$ or evolution of its moments. Moments of a particle distribution are variable averages on phase space, weighted with respect to the distribution function. For example, the first moment of x is written as

$$\langle x \rangle = \frac{\int x f\left(x, x', y, y', \delta\right) \mathrm{d}\mu}{\int f\left(x, x', y, y', \delta\right) \mathrm{d}\mu}, \tag{2.23}$$

where $\mathrm{d}\mu = \mathrm{d}x\mathrm{d}x'\mathrm{d}y\mathrm{d}y'\mathrm{d}\delta$. The brackets $\langle\cdot\rangle$ denote the average over the phase space variables. Similarly, the second moments of the distribution are written as

$$\langle u_i u_j \rangle = \frac{\int u_i u_j f\left(x, x', y, y', \delta\right) \mathrm{d}\mu}{\int f\left(x, x', y, y', \delta\right) \mathrm{d}\mu}, \tag{2.24}$$

where u_i and u_j are any canonical variables.

Taking the statistical average of x^2 over all particles within a bunch at a particular position in a beamline, and using Eq. (2.17) we find:

$$\langle x^2 \rangle = 2\beta_x \langle J_x \cos^2 \phi_x \rangle. \tag{2.25}$$

If we make two assumptions: first, the angle variables are uncorrelated with the action variables within the bunch, and, second, the angle variables are

uniformly distributed from 0 to 2π. Then, we find that the average of the first moments is zero Eq. (2.23):

$$\langle x \rangle = 0, \tag{2.26}$$

and the mean square value of x turns from Eq. (2.25):

$$\langle x^2 \rangle = \beta_x \epsilon_x, \tag{2.27}$$

where the horizontal emittance ϵ_x is defined as the average action of all particles in a bunch:

$$\epsilon_x = \langle J_x \rangle. \tag{2.28}$$

Emittance is the most relevant property of a particle distribution besides the beam current. It is the measure of the phase-space areas occupied by the beam in each of the three projections of the position-momentum phase space. It is also an important measure of beam quality. The term beams quality in accelerator physics, although not precise, points out to a coherence property of the beam: the degree to which the beam particles have nearly the same coordinates as the reference particle, which travels on the accelerator axis with a specified energy and phase [2].

Similarly, using Eqs. (2.17) and (2.18), we find:

$$\langle x x' \rangle = -\alpha_x \epsilon_x, \quad \langle x'^2 \rangle = \gamma_x \epsilon_x. \tag{2.29}$$

Combining Eqs. (2.27), (2.29) with Eq. (2.21), the emittance can be characterized in terms of the beam distribution:

$$\epsilon_x = \sqrt{\langle x^2 \rangle \langle x'^2 \rangle - \langle x x' \rangle^2}. \tag{2.30}$$

If the parameters of a beam distribution are known at a particular position in a beamline, then the emittance can be determined from Eq. (2.30), and appropriate values of the Twiss functions are then found from Eqs. (2.27) and (2.29). The above equations are valid only for uncoupled motion, in other words, if the horizontal motion is treated separately from the vertical and longitudinal motion. Therefore, a bunch of particles has three conserved emittances for a symplectic transport system.

According to Liouville's theorem, the emittance between two points on a beamline is conserved, regardless of the change in beam shape and orientation. But in an accelerator beamline with RF cavities, there is a change in the

energy of particles and the transformation is not symplectic. In that case, the rms emittance will not conserve anymore. The change of the emittance and the Twiss parameters associated with the change in the energy is calculated as follows. A matrix Σ consisting of the second-order moments of the beam distribution using Eqs. (2.27) and (2.29) is constructed:

$$\Sigma = \begin{pmatrix} \langle x^2 \rangle & \langle xx' \rangle \\ \langle xx' \rangle & \langle x' \rangle^2 \end{pmatrix} = \epsilon_x \begin{pmatrix} \beta_x & -\alpha_x \\ -\alpha_x & \gamma_x \end{pmatrix}. \tag{2.31}$$

We can write Σ as:

$$\Sigma = \langle \vec{x} \cdot \vec{x}^{\mathsf{T}} \rangle, \tag{2.32}$$

where $\vec{x} = \left(x, x'\right)^{\mathsf{T}}$ is the phase space vector. As $\vec{x} \rightarrow R_x \vec{x}$, Σ transforms as:

$$\Sigma_{s_1} = R_x \Sigma_{s_0} R_x^{\mathsf{T}}. \tag{2.33}$$

In the case of a change of reference momentum, R_x is:

$$R_x = \begin{pmatrix} 1 & 0 \\ 0 & p_0/p_1 \end{pmatrix}, \tag{2.34}$$

where $p_0 = mc\beta_0\gamma_0$ and $p_1 = mc\beta_1\gamma_1$ are the values of reference momentum before and after the transport, respectively. Solving Eq. (2.33) using Eq. (2.21), the emittance transforms as:

$$\epsilon_{nx} = \beta_0\gamma_0\epsilon_{x_0} = \beta_1\gamma_1\epsilon_{x_1}. \tag{2.35}$$

Equation (2.35) implies that when there is a change in momentum, ϵ_x is not conserved, but the normalized emittance ϵ_{nx} is conserved. Note that β_0, γ_0, β_1, γ_1 are the relativistic parameters, and should not be confused with the Twiss parameters.

2.1.4 Dispersion and Momentum Compaction

In the presence of bending magnets, the horizontal displacement x of a particle from the reference particle is written as

$$x(s) = x_\beta(s) + D_x(s)\,\delta, \tag{2.36}$$

where x_β is the betatron oscillation amplitude, $D_x \equiv D_x(s)$ is the dispersion function, and $\delta = \Delta p/p_0$ is the fractional momentum deviation. The linear dispersion function without space charge $D_x(s)$ is the solution of the equation [36]:

$$D_x''(s) + \kappa_x(s) D_x(s) = \frac{1}{\rho(s)}, \tag{2.37}$$

which gives the local sensitivity of the particle trajectory to the fractional momentum deviation δ, and the prime denotes derivative with respect to distance s along the beamline.

For a multi-particle bunch, we are interested in the evolution of particle distribution moments in the presence of dispersion. The Hamiltonian for a non-interacting particle beam is [37]:

$$H = \frac{1}{2}\left(x'^2 + y'^2\right) + \frac{\kappa_x(s)}{2}x^2 + \frac{\kappa_y(s)}{2}y^2 - \frac{\delta}{\rho(s)}x. \tag{2.38}$$

The differential equations for the horizontal second moments of the beam distribution are derived as follows:

$$\frac{\mathrm{d}}{\mathrm{d}s}\langle x^2\rangle - 2\langle x x'\rangle = 0, \tag{2.39a}$$

$$\frac{\mathrm{d}}{\mathrm{d}s}\langle x'^2\rangle + 2\kappa_x(s)\langle x x'\rangle - \frac{2\langle x'\delta\rangle}{\rho} = 0, \tag{2.39b}$$

$$\frac{\mathrm{d}}{\mathrm{d}s}\langle x x'\rangle - \langle x'^2\rangle + \kappa_x(s)\langle x^2\rangle - \frac{\langle x\delta\rangle}{\rho} = 0, \tag{2.39c}$$

$$\frac{\mathrm{d}}{\mathrm{d}s}\langle x\delta\rangle - \langle x'\delta\rangle = 0, \tag{2.39d}$$

$$\frac{\mathrm{d}}{\mathrm{d}s}\langle x'\delta\rangle + \kappa_x(s)\langle x\delta\rangle - \frac{\langle\delta^2\rangle}{\rho^2} = 0. \tag{2.39e}$$

The Eqs. (2.39d) and (2.39e) can be combined into a single differential equation, then we get:

$$\frac{\mathrm{d}^2}{\mathrm{d}s^2}\langle x\delta\rangle + \kappa_x\langle x\delta\rangle - \frac{\langle\delta^2\rangle}{\rho} = 0. \tag{2.40}$$

Comparing Eqs. (2.37) and (2.40), we obtain:

$$\langle x\delta\rangle = D_x\langle\delta^2\rangle, \quad \langle x'\delta\rangle = D'_x\langle\delta^2\rangle. \tag{2.41}$$

Equation (2.41) shows that in the case of non-zero dispersion, the horizontal trajectory of a particle will depend on the momentum deviation. Therefore, the variation of the trajectory of a particle with respect to the beam energy can be used to determine appropriate values for the dispersion at some point in the beam line.

After substituting Eq. (2.41) into the Eqs. (2.39a)–(2.39c) we can verify that these equations are inhomogeneous linear equations, whose particular solution is given by

$$\langle x^2\rangle = D_x^2\langle\delta^2\rangle, \quad \langle x'^2\rangle = D'^2\langle\delta^2\rangle, \quad \langle xx'\rangle = D_xD'_x\langle\delta^2\rangle.$$

Therefore, we can write the general solution as a superposition of the particular solution and the homogeneous solution (with the subscript "0"):

$$\begin{aligned}
\langle x^2\rangle &= \langle x^2\rangle_0 + D_x^2\langle\delta^2\rangle,\\
\langle x'^2\rangle &= \langle x'^2\rangle_0 + D_x'^2\langle\delta^2\rangle,\\
\langle xx'\rangle &= \langle xx'\rangle_0 + D_xD'_x\langle\delta^2\rangle.
\end{aligned} \tag{2.42}$$

Here "0" stands for the betatron motion, this notation is used to avoid confusion between multi-conventions for β. Equation (2.42) shows that the dispersion function weights the dependence of the second moments of the beam distribution on $\langle\delta^2\rangle$. The linear homogeneous solution is obtained as follows:

$$x = \sqrt{2\beta_xJ_x}\cos\phi_x + D_x\delta. \tag{2.43}$$

Taking second moments of Eq. (2.43) and using Eq. (2.27), we obtain:

$$\langle x^2\rangle = \beta_x\epsilon_x + D_x^2\langle\delta^2\rangle. \tag{2.44}$$

For a Gaussian beam distribution with $\langle x\rangle = \langle\delta\rangle = 0$, Eq. (2.44) can be written in the rms form:

$$\sigma_x = \sqrt{\beta_x\epsilon_x + D_x^2\sigma_\delta^2}, \tag{2.45}$$

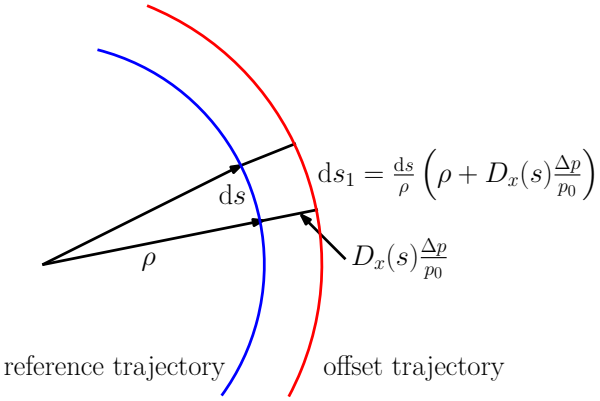

Figure 2.4.: Reference and offset particle trajectories.

where σ_x and σ_δ are the horizontal rms beam size and the rms momentum deviation. An addition of the dipole magnet will change the transport matrix across any section of the beamline that includes bending magnets. However, the structure of the transport matrix will always, for a horizontally bending magnet, be the same as Eq. (2.9). This implies that the horizontal trajectory will depend on the energy deviation, and the path length will depend on the horizontal trajectory. The vertical motion will remain independent of the horizontal and longitudinal motion unless time-dependent fields are not included. In that case, the dispersion along a beam line can be evolved in terms of a 2×2 matrix from one position to another position in the beamline:

$$\begin{pmatrix} D_x \\ D_x' \end{pmatrix}_{s_1} = \begin{pmatrix} R_{11} & R_{12} \\ R_{21} & R_{22} \end{pmatrix} \begin{pmatrix} D_x \\ D_x' \end{pmatrix}_{s_0} + \begin{pmatrix} R_{16} \\ R_{26} \end{pmatrix}. \tag{2.46}$$

Equation (2.46) is used to propagate the dispersion along a beamline when the initial values of dispersion are known.

The path length variation of particles with different momenta along a bend is needed to obtain the required bunch length at a subsequent cavity in an ERL. Consider a short section of the beamline of length in which the reference trajectory followed by an initial phase space vector $\mathbf{x} = 0$ has the radius of curvature ρ in the horizontal plane as shown in Fig. 2.4. The deviation of

the test particle trajectory with the radius of curvature $\rho + x$ from a reference particle trajectory is:

$$\frac{\mathrm{d}s_1}{\mathrm{d}s} = \frac{\rho + D_x\delta}{\rho}, \tag{2.47}$$

where $\mathrm{d}s$ and $\mathrm{d}s_1$ are the distances traveled by the reference particle and test particle, respectively. Introducing the local longitudinal coordinate with respect to the reference particle as z, we use the notation that a particle ahead of the reference particle has $z > 0$ and a particle behind the reference particle has $z < 0$, which implies that the momentum compaction of a bunch compression arc has a positive value. The path length difference between the reference particle and the test particle is obtained by integrating Eq. (2.47) along the beamline:

$$\Delta L = \delta \int \frac{D_x}{\rho}\mathrm{d}s. \tag{2.48}$$

The momentum compaction R_{56} is the variation of the path length with momentum deviation for a relativistic beam:

$$R_{56} = \frac{\Delta L}{\delta} = \int_0^L \frac{D_x}{\rho}\mathrm{d}s, \tag{2.49}$$

which also is the (5,6)th component of the 6×6 transport matrix of the beamline elements, where L is the total path length of the beamline. In the presence of both horizontal and vertical dispersion, R_{56} is defined as:

$$R_{56} = \frac{\Delta L}{\delta} = \int_0^L \frac{D_x + D_y}{\rho}\mathrm{d}s, \tag{2.50}$$

where D_y is the vertical dispersion.

By definition, $z(s) = R_{56}(s)\delta$. An additional expression for the individual particle momentum compaction is obtained by multiplying the last expression by δ and taking the average over the phase space distribution [7]:

$$R_{56} = \frac{\langle z\delta \rangle}{\langle \delta^2 \rangle}. \tag{2.51}$$

The above result can be used to obtain R_{56} from the beam matrix (discussed in chapter 4). Note that this result is only valid for the beamline without RF structures.

The momentum compaction describes the change in the length of a particle trajectory along a beamline resulting from a change in momentum. It is useful to know the variation of time of flight regarding momentum along a beamline described by the phase slip factor η:

$$\eta = \frac{1}{T_0}\frac{\mathrm{d}T}{\mathrm{d}\delta}\bigg|_{\delta=0}, \tag{2.52}$$

where T is the time taken for a particle to travel through two specified positions in a beamline. Using $T = L/\beta c$, Eqs. (2.48) and Eq. (2.49), for a relativistic beam we get:

$$\eta = \frac{R_{56}}{L}\bigg|_{s=L}. \tag{2.53}$$

In some situations it is desirable for the time of fight of a particle between two specified positions in a beam line to be independent of the momentum deviation, at least to first order. If the transport matrix between the specified positions has the property:

$$R_{56} = 0, \tag{2.54}$$

then the section of a beamline satisfying Eq. (2.54) is known as isochronous.

2.1.5 Longitudinal Equations of Motion

In a bunched beam, the particles are confined longitudinally by an RF field. Assuming a cosine longitudinal voltage is applied to the particles by means of an RF structure, the resulting longitudinal motion is called synchrotron motion. The details of this motion can be found in standard text books [2, 36], here our discussions are limited to the necessary parts required for the present work. In an ERL beamline with RF elements, there is coupling between the longitudinal and transverse plane of phase space due to the bending magnets dispersion. We will derive the equations of longitudinal dynamics in an ERL that show implicit coupling with the transverse plane through η.

Consider a single particle moving through an ERL. From the definition of z in subsection 2.1.2, the change in z for a particle travelling with speed βc in the beamline can be written as

$$\Delta z = \frac{L_0}{\beta_0} - \frac{L}{\beta}, \tag{2.55}$$

where L_0 is the length of the beamline along the reference trajectory, and $L = \beta c T$ is the actual path length in the time T that a particle takes to travel through the beamline. For a relativistic particle $\beta_0 \approx 1$. Assuming we can average the change in z over the entire length of the beamline, we get:

$$\frac{\mathrm{d}z}{\mathrm{d}s} \approx \frac{\Delta z}{L_0} = \left(1 - \frac{T}{T_0}\right) \tag{2.56}$$

Using Eqs. (2.52) and (2.56), the equation of motion for the longitudinal coordinate z can be written as

$$\frac{\mathrm{d}z}{\mathrm{d}s} = \eta\delta. \tag{2.57}$$

Now consider the change in momentum deviation $\Delta\delta$ over a beamline including RF structure is:

$$\Delta\delta = \frac{qE_{\mathrm{rf}}}{cp_0} \cos\left(\phi_{\mathrm{rf}} + \frac{\omega_{\mathrm{rf}} z}{c}\right), \tag{2.58}$$

where q is the particle charge, E_{rf} is the peak electric field, ω_{rf} is the RF frequency, p_0 is the reference momentum, ϕ_{rf} is the fixed RF phase of the cavity and z is the longitudinal position of a particle in the bunch.

Again, assuming that we can average the change in z over the entire length of the beamline, we obtain:

$$\frac{\mathrm{d}\delta}{\mathrm{d}s} = \frac{qE_{\mathrm{rf}}}{cp_0 L_0} \cos\left(\phi_{\mathrm{rf}} + \frac{\omega_{\mathrm{rf}} z}{c}\right). \tag{2.59}$$

Equations (2.57) and (2.59) describe the longitudinal dynamics of an electron in a RF linac. Taking the derivative of Eq. (2.57) with respect to s and substituting for $\mathrm{d}\delta/\mathrm{d}s$ from Eq. (2.59), and setting $\phi_{\mathrm{rf}} = \phi_{\mathrm{s}}$ results in [2, 36]:

$$\frac{\mathrm{d}^2 z}{\mathrm{d}s^2} + \kappa_z^2 z = 0, \tag{2.60}$$

with

$$\kappa_z^2 = \frac{qE_{\mathrm{rf}}\omega_{\mathrm{rf}}\eta \sin\phi_{\mathrm{s}}}{mc^3\beta^3\gamma^3}, \tag{2.61}$$

where ϕ_{s} is the synchronous particle phase. When the RF structure is operated at "on-crest" ($\phi_{\mathrm{rf}} = \phi_{\mathrm{s}} = 0$) there is maximum acceleration.

2.2 Bunch Compressor Transport Matrix

The purpose of a bunch compressor is to manipulate the longitudinal phase space distribution of a bunch. There are two main steps required for a compression of a relativistic bunch. The first step is to deduce a correlation between particle energy and longitudinal position within the bunch by accelerating it off-crest in an accelerating section. The second step is to establish a correlation between particle energy and path length by passing through a dispersive section of dipole magnets. In such kind of scheme, the accelerating section is phased such that the reference particle does not see any accelerating RF field while the electrons ahead of the reference particle are accelerated and the particles behind are decelerated. Following the accelerating section, the particles travel through a dispersive section with a finite value of momentum compaction R_{56}, which is required for the longitudinal phase space re-shaping. Early particles within a bunch, having been accelerated, follow a longer path than the reference particle in the center of the bunch while the decelerated particles being late regarding the bunch center follow a shortcut. As the bunch is relativistic, the early particles fall back toward the bunch center while late particles catch up with the bunch center. The bunch length will reach its minimum value at the entrance of the further section of the beamline if we correctly choose the parameters of the beam transport system. The schematic view of a bunch-compressor system is illustrated in Fig. 2.5.

In an RF section transport matrix element R_{65} converts a particle initial position z_{i} with respect to the reference particle to its final momentum deviation δ_{f} from the reference particle final energy $E_{\mathrm{c,f}}$ and R_{66} element reduces the initial

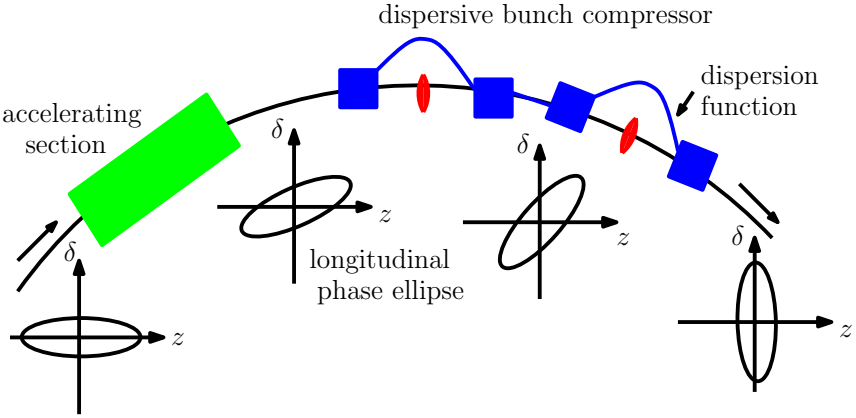

Figure 2.5.: Schematic view of a bunch-compressor system. First, the correlation between particle energy and longitudinal position within the bunch is inserted by accelerating it off-crest in the accelerating section. Second, the differential path-length among portions of the bunch is controlled to compress it by passing it through a dispersive beamline.

δ_i by the ratio of the final to initial energy [38, 39]. Consider an accelerating section with phase ϕ_rf, angular frequency ω_rf and peak RF voltage V_rf. The longitudinal transport matrix for such a system is:

$$\begin{pmatrix} z \\ \delta \end{pmatrix}_\mathrm{f} = \begin{pmatrix} 1 & 0 \\ R_{65} & R_{66} \end{pmatrix} \begin{pmatrix} z \\ \delta \end{pmatrix}_\mathrm{i} = \begin{pmatrix} 1 & 0 \\ h & \frac{E_\mathrm{c,i}}{E_\mathrm{c,f}} \end{pmatrix} \begin{pmatrix} z \\ \delta \end{pmatrix}_\mathrm{i}, \tag{2.62}$$

where h is the momentum chirp given as

$$h = -\frac{qV_\mathrm{rf}\omega_\mathrm{rf}}{cE_\mathrm{c,f}} \sin\phi_\mathrm{rf}.$$

It can be seen from Eq. (2.62) that acceleration has no effect on the longitudinal position of an individual particle with respect to the reference particle. $E_\mathrm{c,i}/E_\mathrm{c,f}$ is an additional term in the net momentum spread due to the initial intrinsic

momentum deviation within the beam. Then, the following set up of equations are obtained after the accelerating section:

$$z_{\mathrm{f}} = z_{\mathrm{i}}, \tag{2.63a}$$

$$\delta_{\mathrm{f}} = hz_{\mathrm{i}} + \frac{E_{\mathrm{c,i}}}{E_{\mathrm{c,f}}}\delta_{\mathrm{i}}. \tag{2.63b}$$

After the off-crest acceleration of a bunch in an accelerating section, it passes through a dispersive section in which R_{56} transport matrix element converts a particle's initial momentum deviation (with respect to the reference particle momentum) to its final z position with respect to the reference particle position as shown in Fig. 2.6. The typical value of R_{56} is a few cm in an ERL beamline. In principle, a single 180° bending magnet could be a bunch compressor, but dispersion is not desired throughout the beamline. The longitudinal transport matrix for such a system is:

$$\begin{pmatrix} z \\ \delta \end{pmatrix}_{\mathrm{f}} = \begin{pmatrix} 1 & R_{56} \\ 0 & 1 \end{pmatrix} \begin{pmatrix} z \\ \delta \end{pmatrix}_{\mathrm{i}}. \tag{2.64}$$

The final position of a particle after passing through a dispersive section is:

$$z_{\mathrm{f}} = z_{\mathrm{i}} + R_{56}\delta_{\mathrm{i}}. \tag{2.65}$$

The total change in the bunch length after passing through the dispersive section is:

$$\Delta z_{\mathrm{f}} = \Delta z_{\mathrm{i}} + R_{56}\Delta\delta_{\mathrm{i}}, \tag{2.66}$$

where Δz_{i} and Δz_{f} are the initial and final bunch length before and after compression respectively.

The ratio of final to initial bunch length by rearranging Eq. (2.66) can be written as:

$$\frac{\Delta z_{\mathrm{f}}}{\Delta z_{\mathrm{i}}} = 1 + R_{56}h, \tag{2.67}$$

where $h = \Delta\delta_{\mathrm{i}}/\Delta z_{\mathrm{i}}$ is the momentum chirp obtained from the off-crest acceleration in the accelerating section that inserts the linear correlation between $z - \delta$.

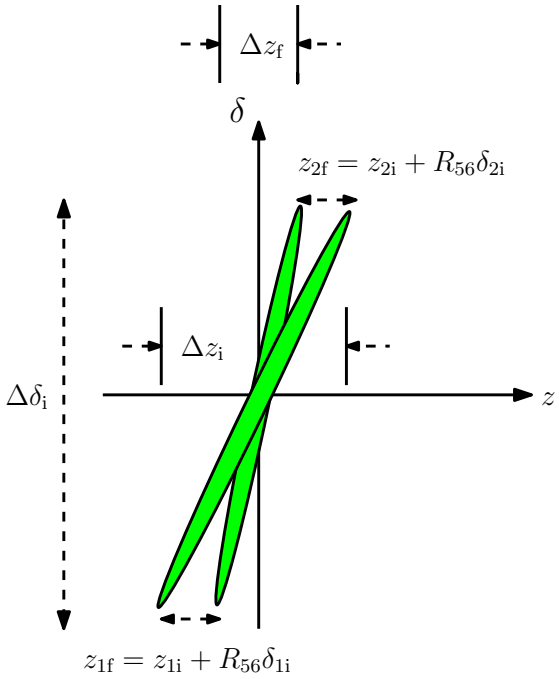

Figure 2.6.: Schematic view of a bunch compression while passing through a dispersive section of beamline with a positive value of R_{56}. Here, Δz_i and $\Delta\delta_\mathrm{i}$ are the initial bunch length and momentum deviation respectively. Δz_f is the final bunch length after bunch compression.

Usually, the goal of a bunch compressor in an ERL is to increase the peak current by reducing the bunch length. In an electron source at low energy, a high beam current can make the beam prone to collective effects that leads to the distortion of the beam quality. But low momentum deviation is required at the location of internal target experiment. The solution is to generate long bunches at the source and use a bunch compressor to increase the beam quality once the beam reached at high energy and becomes less sensitive to collective effects.

3 Beam Intensity Effects in Energy Recovery Linacs

The particle beams in an accelerator are focused and controlled by the electromagnetic fields of magnets, radio frequency cavities, and other accelerator components. The single-particle dynamics considers only the external forces on a particle. But a bunch of particles contains charged particles that have their own electromagnetic fields. Thus, adding up a lot of particles in a bunch creates intense electromagnetic fields that compete with the external controlling fields. This self-interaction of particles results in collective effects. Collective effects take into account the effects of the beam's own Coulomb force field on itself and on it's environment. The phenomena associated with collective effects are diverse, and their analysis is often quite complicated.

The detailed study of the origin of collective effects is important for a successful design of the accelerators, including corrective measures. These effects are responsible for the final intensity limit in most accelerators. These effects must be taken into account when significant beam intensities are desired. Most accelerator design and developments are conducted to exclude collective effects as much as possible through self-imposed limitation on the operation or by implanting other stabilizing control mechanisms [35].

One of the most important collective effects is the beam's own Coulomb force field on particles in the beam (beam-self interaction). In accelerator dialect, this is called as the "space charge" field, or the "space charge" effect. A generic particle in the bunch experiences the collective Coulomb force due to fields generated by all the other particles in the bunch. The space charge impact on the beam dynamics is generally proportional to the intensity, energy and current of the beam. In a dispersive beamline, space charge together with dispersion can lead to the amplification of the initial shot noise by density modulation along the beamline, which is known as microbunching instability.

This chapter introduces a basic theory of how the electric charge of a particle beam can become a major contribution to the forces encountered by individual particles while travelling along a low energy beam transport line in section 3.1. The numerical methods to calculate the linear space charge effects are

outlined in section 3.2 followed by the theoretical beam models and envelope equations to study space charge in section 3.3. In section 3.4, the theory of pervasive occurrence of microbunching instability in dispersive beamlines which potentially affects the beam performance and operation is explained. In its common explanation, this instability is driven by a longitudinal component of the beam self-fields originating from the space charge. Perturbations in the beam density like shot noise can seed self-fields on a microscale which then modify the energy profile along the bunch. As the beam travels through dispersive beamlines the modified energy profile causes differential longitudinal slippage and induces ripples in the current profile by further amplifying self-fields. The net result of this amplifying loop leads to the degradation of the beam quality [30]. The beam matrix approach with space charge will be used to compute the microbunching instability gain analytically.

3.1 Space Charge

For high intensity beams at low energy, the self-interaction between the charged particles becomes important. This self-interaction of charged particles in a bunch is the sum of the "collisional force", dominated by the binary collisions caused by immediate neighbors particle interactions, and "space-charge" collective force, which results from many particles that produce an average field. For particle accelerators beams, collisional force is a relatively small effect, and it usually undergoes Debye shielding [40]. Thus, the mutual interactions between particles can be described by the smoothed-space-charge field in which the granularity of the distribution of discrete particles is smoothed.

The total Coulomb field experienced by any single particle is the sum of the fields of all other particles in the bunch. For an intense beam, one can no longer neglect space charge fields compared to the applied external fields. The bunch charges produce a mutually repulsive electric fields that act opposite to the applied focusing force, and also a magnetic field that produces an attractive force. The magnetic forces are smaller than the electric forces for low energies and become important for relativistic beams. We illustrate this by considering a simple example of a long bunch, approximately represented by an infinitely long cylinder with charge density $\lambda(r) = qN(r)$ moving at velocity v. Using Gauss's law [41], the radially outward directed electric field is (see also Ref. [2]):

$$E_r = \int^{r} \frac{\lambda(r)}{\epsilon_0}\, \mathrm{d}r,$$

from Ampere's law [41], the azimuthal magnetic field is:

$$B_\theta = \int^{r} \upsilon \mu_0 \lambda(r)\, \mathrm{d}r.$$

The radial Lorentz force by using Eq. (2.1) is $F_r = q(E_r - \upsilon B_\theta) = qE_r/\gamma^2$. Thus, the transverse equation of motion in the paraxial approximation is:

$$\frac{\mathrm{d}^2 r}{\mathrm{d}t^2} = \frac{qE_r}{\gamma^3 m}. \tag{3.1}$$

While the magnetic-self force does not affect the longitudinal motion of the particles, but longitudinal motion is also affected by a factor of $\gamma^3 m$, which results in:

$$\frac{\mathrm{d}^2 z}{\mathrm{d}t^2} = \frac{qE_z}{\gamma^3 m}. \tag{3.2}$$

The attractive magnetic force tends to compensate for the repulsive electric force of electrons when the energy is higher than 100 MeV [19]. Therefore, space charge defocusing is a major concern at low energy for electron beams especially at the injection into the main RF system.

3.2 Numerical Methods for Space Charge Calculations

The mathematical analysis becomes considerably more complex than the single particle dynamics in the presence of space charge. One can solve the motion of a single particle with any desired accuracy by solving the Lorentz force equation in an applied field. However, it is not practical to find exact solutions of the equations of motion for the large number of particles interacting with each other in an intense bunch. In that case, tracking codes are crucial tools for the study of beam dynamics and the design of intense charged particle devices with self-fields. The simulated particles in tracking codes are known as macroparticles, and each macroparticle represents the total charge of many real particles. However, even the most advanced codes can use only some macroparticles compared to the actual number of particles in a bunch and require intensive computational power. Therefore, an analytical approach to estimate the effects of space charge at the initial stage of machine design and optimization is required.

Space-charge effects can be analysed generally by summing up the Coulomb force between all the particles in a bunch. However, a typical bunch contains $10^8 - 10^9$ particles, which makes this approach unrealistic for beam dynamics computation. Unlike a plasma, shielding effects are incomplete in a particle beam because the beam radius is comparable to the Debye length. The Space-charge fields can be categorized into linear and non-linear forces as a function of the displacement from the bunch centroid. In this thesis, we will limit our discussions to the linear space-charge forces only, which defocus the beam and lead to an increase in beam size.

We can solve only specific cases of uniform beam distributions analytically. However, it is possible to make a few generalizations following the Sacherer's approach [42] such that the linear part of the self-field depends only on the rms size of the distribution and only weakly on its exact form. This implies that for the computation of rms dynamics, an equivalent uniform beam, which has the same rms values, can replace the actual beam. Linear-space-charge forces allow the use of the beam matrix method. The equation to track rms second moments σ_{s_1} from s_0 to s_1 is [2]:

$$\sigma_{s_1} = R(s_0 \rightarrow s_1)\, \sigma_{s_0}\, R^{\mathsf{T}}(s_0 \rightarrow s_1), \tag{3.3}$$

where R is the transport matrix from s_0 to s_1 with a space-charge kick explained in the next section.

We cannot compute the space-charge-induced emittance growth in this linear space-charge calculations. However, the beam matrix approach is very useful for finding the beam size parameters with space charge which helps to match a non-periodic lattice into the subsequent section of the machine. It can also be used to calculate the required quadrupole gradients to match the beam with space charge.

Space charge calculations require particle tracking to include the space-charge-induced emittance growth effects and to illustrate the evaluation of the beam distribution. In this work, we use ELEGANT [27] for particle tracking with space charge (discussed in section 4.2).

3.3 RMS Envelope Equations with Space Charge

In this section, it is shown that within a beam described by the Kapchinsky–Vladimirsky, or KV distribution [43] in the transverse plane, the space-charge forces have a linear dependence on position within the beam. This allows

us to derive a set of envelope equations describing how the transverse beam sizes of a beam with a KV distribution evolve along a beam line, which can be modified for the Gaussian beam distribution by using the rms values of beam radii and emittance. Similarly, a beam distribution in the longitudinal plane is required which can treat space charge linearly. However, we cannot extend the 4D KV distribution to 6D because it yields a nonlinear space-charge field in the longitudinal direction because of hyper-ellipsoid symmetry [36]. But for a parabolic linear density, it is possible to derive a longitudinal envelope equation with a linear-space-charge kick [44].

3.3.1 The KV Distribution and Envelope Equations

The KV distribution is an important mathematical entity to study the effects of space charge in the family of elliptically symmetric beam distributions [36]. Specifically, the projection of KV distribution onto the x-y plane give a uniform particle density within a specific ellipse. The force seen by any individual particle in a continuous beam varies linearly with distance from the center of the uniform ellipse, and the beam dynamics can be treated using the techniques of linear dynamics. Mathematically, the KV distribution is defined by the particle density function Ψ [34]:

$$\Psi(\phi_x, \phi_y, J_x, J_y) = \Psi_0 \delta_D \left(1 - \frac{J_x}{J_{x_0}} - \frac{J_y}{J_{y_0}} \right). \tag{3.4}$$

Here, $\Psi_0 = n_q/(4\pi^2 J_{x_0} J_{y_0})$, $\delta_D(x)$ is the Dirac delta function, and J_{x_0} and J_{y_0} are the initial action variables with positive constant values. J_x is the horizontal action variable for the particle distribution in the horizontal phase space x and x' defined in Eq. (2.19). Similarly, J_y is the vertical action variable.

The number of particles per unit distance along the beamline n_q can be obtained by integrating Eq. (3.4) over the horizontal and vertical action-angle variables. Using the properties of the Dirac delta function, we find n_q:

$$\int_0^{2\pi} \mathrm{d}\phi_x \int_0^{2\pi} \mathrm{d}\phi_y \int_0^{J_{x_0}} \mathrm{d}J_x \int_0^{J_{y_0}} \mathrm{d}J_y \Psi = n_q. \tag{3.5}$$

For a KV distribution, the particle density in the x-y plane is uniform within an ellipse of half-axes $a_x = \sqrt{2\beta_x J_{x_0}}$ and $a_y = \sqrt{2\beta_y J_{y_0}}$. Using Eq. (2.18), this can be proved by calculating the beam moments for such a beam distribution [34]:

$$\langle x^{2m} \rangle = \frac{1}{2\pi} \int_0^{2\pi} \cos^{2m} \phi_x \mathrm{d}\phi_x \frac{\left(2\beta_x J_{x_0}\right)^m}{m+1}, \tag{3.6}$$

where m is any positive integer. A similar expression can be obtained for the vertical plane moments $\langle y^{2m} \rangle$. Now consider an ellipse with uniform charge density $\rho_\mathrm{u} = q n_\mathrm{q} / \pi a_x a_y$ defined as:

$$\frac{x^2}{a_x^2} + \frac{y^2}{a_y^2} = 1, \tag{3.7}$$

such that the particle density is zero outside this ellipse. The beam moments of this distribution are:

$$\langle x^{2m} \rangle = \frac{\iint \rho x^{2m} \mathrm{d}x\mathrm{d}y}{\iint \rho \mathrm{d}x\mathrm{d}y} = \frac{1}{\pi a_x a_y} \iint x^{2m} \mathrm{d}x\mathrm{d}y, \tag{3.8}$$

here the limits of integration are defined by the ellipse Eq.(3.7). Equation (3.8) can be rewritten in terms of r and θ by replacing x and y into the polar coordinates:

$$\langle x^{2m} \rangle = \frac{1}{2\pi} \int_0^{2\pi} \cos^{2m} \theta \mathrm{d}\theta \frac{a_x^{2m}}{m+1}. \tag{3.9}$$

It can be seen from the comparison of Eqs. (3.6) and (3.9) that beam moments $\langle x^{2m} \rangle$ for the KV distribution are the same as the moments for the uniform coordinate space distribution, if:

$$a_x = \sqrt{2\beta_x J_{x_0}}. \tag{3.10}$$

For a uniform elliptical charge density the electric and magnetic field in the laboratory frame are [45]:

$$E_x(x,y) = \frac{qn_q}{\pi\epsilon_0}\frac{x}{a_x\left(a_x+a_y\right)}, \quad E_y(x,y) = \frac{qn_q}{\pi\epsilon_0}\frac{y}{a_y\left(a_x+a_y\right)}, \tag{3.11}$$

$$B_x(x,y) = -\frac{\beta}{c}E_y, \quad B_y(x,y) = \frac{\beta}{c}E_x. \tag{3.12}$$

It can be seen from Eq. (3.11) that for a beam with a KV distribution, the electric field in the beam is directly proportional to the distance from the axis of the beam. It means that the space charge forces have a similar effect on the beam as the magnetic field in a quadrupole, and it is possible to describe the behaviour of the beam using the approaches of linear dynamics. Unlike quadruple fields, space charge forces are simultaneously defocusing in the horizontal and vertical planes and depend upon the size of the beam and particle density. Using the Lorentz force Eq.(2.1) and field expressions Eqs. (3.11) and (3.12), the space-charge force components in the laboratory frame are obtained as:

$$F_x = \frac{qE_x}{\gamma^2} = \frac{q^2n_q}{\pi\epsilon_0\gamma^2}\frac{x}{a_x\left(a_x+a_y\right)}, \tag{3.13}$$

$$F_y = \frac{qE_y}{\gamma^2} = \frac{q^2n_q}{\pi\epsilon_0\gamma^2}\frac{y}{a_y\left(a_x+a_y\right)}. \tag{3.14}$$

The resultant force for a high beam energy is equal to the electric force divided by γ^2 because the force from the electric field is nearly cancelled by the force from the magnetic field. If paraxial approximation is applied, the trajectory of a particle makes only a small angle with the axis, we can write:

$$x'' = \frac{F_x}{\beta^2\gamma mc^2} = \frac{2K_{sc}}{a_x(a_x+a_y)}x, \tag{3.15}$$

where K_{sc} is the space charge perveance, which measures the strength of transverse space charge [36]:

$$K_{sc} = \frac{2I}{\beta^3\gamma^3 I_A}, \tag{3.16}$$

where β and γ are the relativistic factors. The space charge perveance K_{sc} is a function of the beam energy and current, which can be assumed to be constant along the particular beam line. $I_A \approx 17.045\,\text{kA}$ is Alfvén current. I is the total beam current:

$$I = qn_q\beta c. \tag{3.17}$$

Including linear focusing of magnets and RF cavities in a beamline and using Eqs. (2.20) and (3.10), we get the envelope equations in the presence of linear-space-charge forces for a KV beam of action J_x having a maximum value $J_{x,\max}$ with horizontal radius a_x and vertical radius a_y:

$$a_x'' + \left(\kappa_x(s) - \frac{2K_{sc}}{a_x(a_x+a_y)}\right)a_x - \frac{4J_{x,\max}^2}{a_x^3} = 0, \tag{3.18a}$$

$$a_y'' + \left(\kappa_y(s) - \frac{2K_{sc}}{a_y(a_x+a_y)}\right)a_y - \frac{4J_{y,\max}^2}{a_y^3} = 0. \tag{3.18b}$$

Equivalent rms beam size and emittance are [34, 36]:

$$\sigma_x = \frac{a_x}{2}, \quad \epsilon_x = \langle J_x \rangle = \frac{J_{x,\max}}{2}. \tag{3.19}$$

The similar expressions are valid for vertical rms beam size and emittance by replacing x by y in Eq. (3.19).

For a beam with KV distribution, the emittance is conserved under the influence of linear focusing forces, including space-charge forces during the beam transportation along a beamline. This results because in coordinate space the particles are uniformly distributed inside an ellipse (the cross-section of the beam), so the horizontal and vertical components of the space-charge force vary linearly with distance from the centre of the ellipse. In other elliptical beam distributions, there will be some variation in the emittance along the beam line. But since the KV distribution represents a stationary distribution with the minimum electrical potential energy for an emittance, one can expect that the elliptical distribution will ultimately tend towards a KV distribution. Thus, equivalent rms envelope equations are valid for any equivalent distribution to KV distribution if it has the same Twiss parameters and emittances.

3.3.2 RMS Envelope Equations for a Dispersive Beamline

Following Sacherer's approach [42] for a given beam distribution such that the linear part of the self-field depends only on the rms size of the distribution and only very weakly on its exact form. The Venturini-Reiser (VR) [46] or Lee-Okamoto (LO) [47] envelope-dispersion equations can be applied to find a matched solution for a Gaussian beam distribution in a dispersive beamline. A set of rms envelope equations were presented by VR and LO in the presence of dispersion and longitudinal momentum deviation based on the canonical transformation of variables to a system on the off-momentum particle trajectories. The main motive of these theories is to find an invariant emittance for a beam passing through bends, as the standard rms emittance $\epsilon_x^2 = (\langle x^2\rangle\langle x'^2\rangle - \langle xx'\rangle^2)$ depends on dispersion because of the coupling between x and δ. The generalized invariant emittance with dispersion is (see [48])

$$\epsilon_{dx}^2 = (\epsilon_x^2 - \sigma_\delta^2\langle(x'D_x - xD_x')^2\rangle), \tag{3.20}$$

where $\sigma_\delta = \langle\sqrt{\delta^2}\rangle$ is the rms momentum deviation, and $\langle\cdot\rangle$ angular brackets denote phase space averages (Eq. (2.24)). ϵ_y is the vertical rms emittance. For simplicity, it is assumed that bending occurs only in the horizontal plane. We use the envelope-dispersion equations written in symmetric form by Okamoto and Machida [49]:

$$D_x'' + \left(\kappa_x(s) - \frac{K_{sc}}{2X(X+Y)}\right)D_x - \frac{1}{\rho} = 0, \tag{3.21a}$$

$$\sigma_x'' + \left(\kappa_x(s) - \frac{K_{sc}}{2X(X+Y)}\right)\sigma_x - \frac{\epsilon_{dx}^2}{\sigma_x^3} = 0, \tag{3.21b}$$

$$\sigma_y'' + \left(\kappa_y(s) - \frac{K_{sc}}{2Y(X+Y)}\right)\sigma_x - \frac{\epsilon_y^2}{\sigma_y^3} = 0. \tag{3.21c}$$

Here, $\kappa_{x,y}$ are the linearized external focusing gradients, $\sigma_x = \sqrt{\langle x^2\rangle}$, $\sigma_y = \sqrt{\langle y^2\rangle}$ are the rms betatron amplitudes. X and Y are the effective transverse rms beam radii including dispersion:

$$X^2 = \sigma_x^2 + D_x^2\sigma_\delta^2, \quad Y = \sigma_y. \tag{3.22}$$

K_{sc} is the space charge perveance defined in Eq. (3.16).

A numerical analysis is required to solve the rms envelopes equations together with the dispersion function (Eqs. (3.21a)-(3.18b)) along a beamline, including space charge. In this work we will not solve the envelope equation directly, but will make use of the beam matrix approach (see section 4.1).

3.3.3 Longitudinal Envelope Equation with Space Charge

In an ERL one can expect longitudinal-transverse coupling due to the space charge force and dispersion. The longitudinal space-charge forces lead to a modification of the focusing potential, which in turn leads to a change in the longitudinal profile of an equilibrium particle distribution within a bunch. However, if we assume that beam radius is shorter than the bunch length and bunch length is short compared to the RF wavelength, so that the short-bunch approximation is valid and the applied longitudinal force is linear. It is valid to use the longitudinal envelope equation for a quantitative analysis of longitudinal beam dynamics. The detailed derivation of Neuffer's envelope equation for a parabolic line-charge density profile can be found in Refs. [34, 36, 50].

The longitudinal envelope equation for half-bunch length $z_{\mathrm{m}}(s)$ is [44]:

$$z_{\mathrm{m}}'' + \kappa_z^2 z_{\mathrm{m}} - \frac{K_l}{z_{\mathrm{m}}^2} - \frac{\epsilon_{\mathrm{l}}^2}{z_{\mathrm{m}}^3} = 0. \tag{3.23}$$

K_{l} is the longitudinal perveance:

$$K_{\mathrm{l}} = \frac{-3gNr_{\mathrm{e}}\eta}{\left(2\beta^2\gamma^3\right)}, \tag{3.24}$$

where $g = 0.67 + 2\ln\left(r_{\mathrm{p}}/r_{\mathrm{b}}\right)$ is the geometry factor (r_{p} and r_{b} are the radii of the beam pipe and beam, respectively), N is the number of particles in the bunch and r_{e} is the classical electron radius. κ_z^2 is the is the linearized RF focusing constant as defined in Eq. (2.61). The beam current for a parabolic particle distribution is $I = (3Nq)/(4z_{\mathrm{m}})$. It should be noted that for a non-parabolic distribution, it is necessary to use rms values for the bunch length and the emittance. Equivalent rms half-bunch length and emittance are [51]:

$$\sigma_z = \left\langle z_{\mathrm{m}}^2 \right\rangle^{1/2} = z_{\mathrm{m}}/\sqrt{5}, \quad \epsilon_{\mathrm{l}_{\mathrm{rms}}} = \epsilon_{\mathrm{l}}/5. \tag{3.25}$$

The longitudinal emittance ϵ_l is the zz' phase space area:

$$\epsilon_l = \left|\eta\right| z_m \delta_0. \tag{3.26}$$

3.4 Microbunching Instability

The microbunching instability is a pervasive occurrence in the transport beamlines of an ERL with potentially adverse effects on machine operation and performance. Irregularities in the beam density (shot noise or noise in the electron beam sources) can seed self-fields on the μm scale, which then change the energy profile along the bunch. As the beam travels through dispersive beam lines (bunch compressors, recirculation arcs) the changed energy profile causes differential longitudinal slippage and induces the formation of ripples (microbunching) in the current profile on the same μm scale, further amplifying the self-fields. The net result of this feedback loop can be an undesirable deterioration of the beam quality [52].

Accurate and efficient modeling of this instability is important for the design studies of an ERL. Particle tracking or macroparticle simulations are beneficial but using some macroparticles significantly smaller than the real bunch population introduces additional bogus noise that may outweigh the ripples of physical instability. Therefore, a careful convergence study of various numerical parameters is required to obtain reliable results, which demands extensive computational power and time [22, 53]. However, it is also challenging to analyse small ripples in the phase space. For an accurate and efficient analysis of microbunching instability amplification or gain in a transport beamline, we use a beam matrix tracking approach with space charge [30]. This approach will be further discussed in chapter 4. There are two main assumptions for our approach: first, space charge and transport optics are linear and second, the density modulations amplitude is much smaller than the average current or unperturbed bunch density amplitude. Our approach allows us to optimize the lattice with space charge and it is faster than particle tracking. Numerical noise is also not an issue in our approach because we are not directly dealing with the phase space distribution.

Further in subsection 3.4.1, the theoretical formulation of space charge induced microbunching instability is introduced. Subsection 3.4.2 gives a brief summary of the longitudinal space charge impedance models. The expression for space-charge-induced microbunching instability gain is given in subsection 3.4.3.

3.4.1 Microbunching Instability Gain Mechanism

In an ERL, the beam quality is mainly determined by the source. The high-intensity electron beams required for ERL operation are generated by a photocathode source. The typical features of this electron beam strongly depend on the laser profile used for irradiating the cathode. Since the typical laser intensity profile is not smooth, it will produce current density modulations during the photoemission process. The initial bunch current spectrum can be characterized by the bunching factor, defined as [26]:

$$b_0\left(k_0\right) = \frac{1}{Nec}\int I_0\left(z_0\right)\exp\left(-ik_0 z_0\right)\mathrm{d}z_0, \tag{3.27}$$

where $I_0(z_0)$ is the initial current profile as a function of the longitudinal position z_0 in the bunch, N is the total number of electrons in the bunch, and $k_0 = 2\pi/\lambda_0$ is the initial wave number for the corresponding initial modulation wavelength λ_0.

Microbunching instability is a single bunch instability. Shot noise is a driving source for the initial microstructures in the beam. In a relatively low energy beam, the electrons repel each other in the higher density regions and start space charge oscillations between density and energy modulations. At a scale much smaller than the bunch length, high-frequency space charge impedance or short-ranged wakefields become significant and give rise to the microbunching instability. When the bunch propagates through dipole magnets, it transforms energy modulation into density modulation with an increased magnitude of microbunching because R_{56} introduces path length dependence on energy. This density-energy conversion, if building a positive feedback, can cause an enhancement of modulation amplitudes. One of the main adverse effect of microbunching instability is growth in energy spread. At the end, there will be significant fragmentation in the longitudinal phase space of the beam and also the possibility of growth in emittance if dispersive beamlines induce significant energy modulations. Figure 3.1 illustrates the microbunching instability mechanism.

The amplitude of microbunching instability gain for different modulation wavelength grows independently under two assumptions. First, the initial modulation wavelength is shorter than the electron bunch length, and second, amplitude of modulations is much smaller than the unperturbed bunch density amplitude. The microbunching instability gain is defined as the ratio

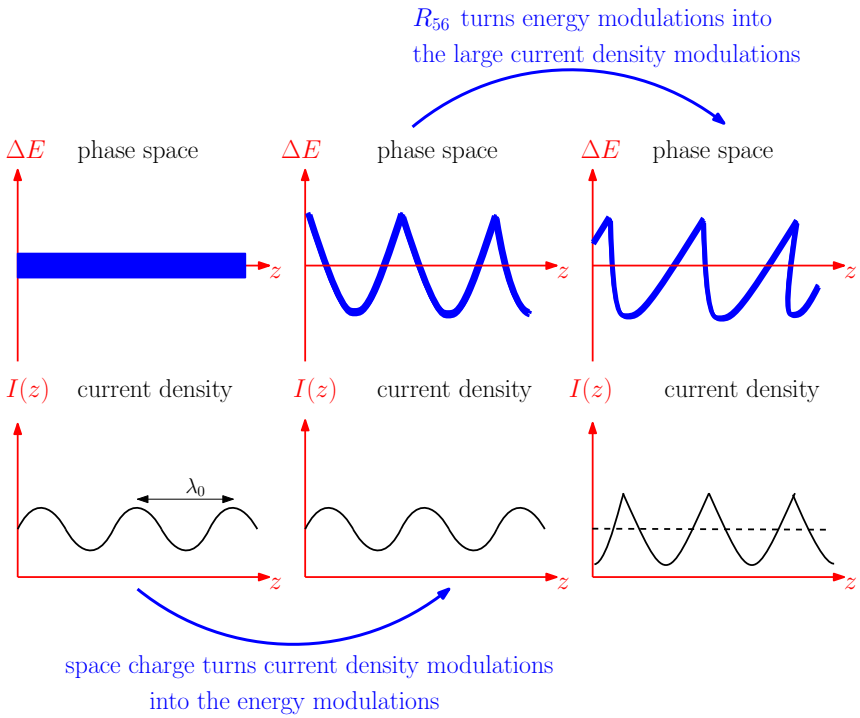

Figure 3.1.: Illustration of the microbunching instability mechanism in a dispersive arc of an ERL. The initial density modulations induce the energy modulations in the phase space because of the space charge impedance. While passing through a dispersive lattice, these energy modulations convert to additional density modulations because R_{56} introduces path length dependence on energy.

of the relative increase in amplitude of final density modulations to the relative amplitude of initial density modulations [24]:

$$G(k_0) = 1 + \left| \frac{b_f(k_f)}{b_0(k_0)} \right|, \tag{3.28}$$

where $b_f(k_f)$ is the final bunching factor for the corresponding wavenumber k_f. Note that we are not making any high-gain approximation for Eq. (3.28) as defined in [26, 54, 55].

3.4.2 Longitudinal Space Charge Impedance Model

Studies of space charge effects on a high-intensity beam stability passing through a low energy transport beamline have been a topic of discussion for a long time [25, 55, 56, 57]. Longitudinal space charge plays an important role in microbunching dynamics as shown in Fig. 3.1.

Consider a long electron beam of transverse uniform particle density λ_r with radius r_b. The transverse density is normalized as:

$$\int \lambda_r(x', y', s)\mathrm{d}x'\mathrm{d}y' = 1.$$

The electric field E_z generated by a single electron in the lab frame at $\vec{r} = (x, y, z)$ [58]:

$$E_z(x, y, z) = \frac{q}{4\pi\epsilon_0} \frac{(z - z')\gamma}{\left[(x - x')^2 + (y - y')^2 + \gamma^2(z - z')^2\right]^{3/2}},$$

where $\vec{r}' = (x', y', z')$ is the position vector of the electron.

The resultant electric field generated by a thin disk of electrons is obtained by superposition principle and written as:

$$E_z(\vec{r}, s) = \frac{q_{\mathrm{disk}}\lambda_r}{4\pi\epsilon_0} \int \mathbf{G}(\vec{r}, \vec{r}')\mathrm{d}^3\vec{r}', \tag{3.29}$$

with Green's function

$$\mathbf{G}(\vec{r}, \vec{r}') = (z - z')\gamma / \left[(x - x')^2 + (y - y')^2 + \gamma^2(z - z')^2\right]^{3/2}.$$

The wakefield potential due to the longitudinal electric field is:

$$w_z = -\frac{1}{q_{\text{disk}}} \int_0^L E_z(\vec{r}, s) \mathrm{d}s.$$

An impedance per unit length in terms of wakefield potential is defined as

$$Z(k) = \frac{1}{c} \int_{-\infty}^{\infty} \widehat{w_z}(z) e^{-ikz} \mathrm{d}z, \tag{3.30}$$

where $\widehat{w_z}(z) = w(z)/L$ is the wakefield potential per unit length.

Using Eqs. (3.29) and (3.30) and transforming Green's function into cylindrical coordinates [58], we obtain an expression for 1D longitudinal space charge impedance in a free space [56, 58]:

$$Z(k) = i \frac{Z_0}{\pi \gamma r_\text{b}} \frac{1 - \xi_\text{b} K_1(\xi_\text{b})}{\xi_\text{b}}, \tag{3.31}$$

with $\xi_\text{b} = k r_\text{b}/\gamma$. Where k is the wavenumber, γ is the relativistic factor, $Z_0 = 377\,\Omega$ is the free space impedance, K_1 is the modified Bessel function, and r_b is the beam radius. We can use this model for Gaussian beam distributions also if $r_\text{b} = 1.7(\sigma_x + \sigma_y)/2$ [25, 56].

In case of shorter wavelength limit when the initial modulation wavelength is shorter than the beam radius $k r_\text{b} >> 1$ such that we can ignore the transverse boundary conditions Eq. (3.31) yields [59]:

$$Z(k \to \infty) = \frac{i Z_0}{\pi k r_\text{b}^2},$$

as modified Bessel function decreases exponentially.

For larger wavelength limit $k r_\text{b} << 1$ Eq. (3.31) yields [56]:

$$Z(k \to 0) = -i \frac{Z_0}{4\pi} \frac{k}{\gamma^2} \left[log \frac{\xi_\text{b}^2}{4} + 2\gamma_\text{E} - 1 \right],$$

where $\gamma_E \approx 0.577$ is the Euler constant.

Consider again a beam model with transverse uniform density and round cross-section to estimate the effect of perfectly conducting boundaries of a beam pipe with radius r_p. The expression for impedance with boundaries can be obtained by repeating the same procedure as for 1D free space impedance.It is obtained as [56]:

$$Z(k) = i\frac{Z_0}{\pi\gamma r_b}\frac{1}{\xi_b}\left[1-\xi_b\left(K_1(\xi_b)+K_0\left(\xi_b r_p/r_b\right)\times\frac{I_1\left(\xi_b\right)}{I_0\left(\xi_b r_p/r_b\right)}\right)\right], \tag{3.32}$$

where I_0 and I_1 are the modified Bessel functions of the first kind, and K_0 is the modified Bessel function of the second kind.

For small wavelength limit, Eq. (3.32) takes the same form as for the free space case Eq. (3.31) because both $K_0\left(\xi_b r_p/r_b\right)$ and $I_1\left(\xi_b\right)/I_0\left(\xi_b r_p/r_b\right)$ decrease exponentially. Note that the longitudinal space charge just redistribute the beam energy with no net energy loss because it is imaginary.

Figure 3.2 shows the comparison of free space longitudinal space charge impedance Eq. (3.31) and impedance with boundary Eq. (3.32) for a beam of radius $r_b = 1.2\,\text{mm}$ at 5 MeV energy. It can be seen that the effect of boundaries become significant at longer wavelengths $\lambda = 2\pi r_p/\gamma$. For a typical beam pipe radius, this wavelength is out of the range of the microbunching region of interest. Therefore, it can be concluded that the free space impedance model is sufficient for the beam parameters in the interest of this thesis work.

3.4.3 Space Charge Induced Microbunching Gain

The microbunching gain defined as the ratio of initial and final amplitude of density modulations is used to quantify the pervasive effects of microbunching instability. Analytically, the microbunching gain due to longitudinal space charge over a beamline of length L can be described as follows [25]:

$$G = 1+\frac{I_0}{\gamma I_A}\left|k_f R_{56}\int_0^L \mathrm{d}s\,\frac{4\pi Z(k_0,s)}{Z_0}\right|\exp\left(-\frac{k_f^2 R_{56}^2\sigma_\delta^2}{2}\right), \tag{3.33}$$

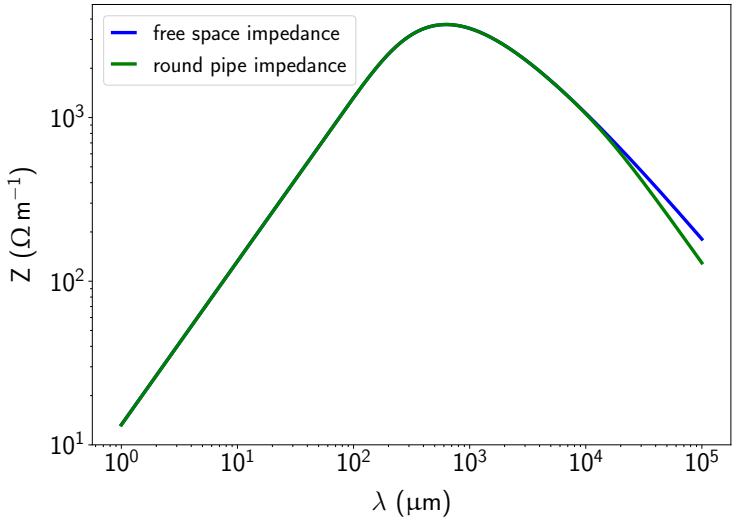

Figure 3.2.: Comparison of free space longitudinal space charge impedance Eq. (3.31) and impedance with boundary Eq. (3.32) for a beam of radius $r_b = 1.2\,\text{mm}$ at 5 MeV energy.

where σ_δ is the initial intrinsic momentum deviation. R_{56} is obtained from the transport matrix of beamline elements. It can be seen from Eq. (3.33) that the microbunching gain reduces exponentially for the Gaussian momentum deviation model in the presence of the finite slice momentum deviation σ_δ. Typically, gain has a peak value when $k_f R_{56}\sigma_\delta \approx 1$. The maximum microbunching gain, induced by longitudinal space charge depends sensitively on the intrinsic momentum deviation and R_{56} and scales as $1/\left(R_{56}{\sigma_\delta}^2\right)$ as longitudinal space charge impedance almost scales linearly with k_0.

4 Simulation Tools and Methodology

This chapter summarizes the simulation tools used in this thesis. In section 4.1, we describe how to implement the discussed beam matrix tracking formalism to study space charge effects and microbunching instability in practical beamline designs. Section 4.2 outlines the space charge models in ELEGANT [27] and steps to compute the space charge induced microbunching instability gain in ELEGANT. Finally, we compare the beam matrix approach and ELEGANT particle tracking simulations results for lattice parameters, beam envelopes, space charge, and microbunching instability gain in section 4.3.

4.1 Beam Matrix Tracking

The implemented beam matrix approach adopts inputs and outputs from the well known lattice design software MAD-X [60]. This option makes the beam matrix solver a very convenient tool for beamline design to evaluate the impact of space charge and microbunching instability. It is also very handy to improve or iterate the design strategies for beam matching with space charge when space charge is a major concern. Because MAD-X treats the RF cavities as a drift and does not involve longitudinal focusing. To treat RF cavities correctly and consider longitudinal focusing, we also implemented the transport matrices explained in chapter 2 in the beam matrix solver and compared it with the particle tracking code ELEGANT [27]. A space charge model is implemented in the beam matrix approach as discussed in Refs. [61, 62, 63]. The beam matrix approach does not account for the space charge induced emittance growth because of the assumption of linearity as discussed in section 3.2. Nevertheless, this approach is very useful for finding the Twiss parameters with space charge, and the quadrupole strength values needed to match the beam parameters.

Instead of individual particle tracking, we track the second moments in the matrix approach defined as [42, 61, 62]:

$$\sigma_{ij} = \begin{pmatrix} \langle x^2 \rangle & \langle xx' \rangle & \langle xy \rangle & \langle xy' \rangle & \langle xz \rangle & \langle x\delta \rangle \\ \langle xx' \rangle & \langle x'^2 \rangle & \langle x'y \rangle & \langle x'y' \rangle & \langle x'z \rangle & \langle x'\delta \rangle \\ \langle xy \rangle & \langle x'y \rangle & \langle y^2 \rangle & \langle yy' \rangle & \langle yz \rangle & \langle y\delta \rangle \\ \langle xy' \rangle & \langle x'y' \rangle & \langle yy' \rangle & \langle y'^2 \rangle & \langle y'z \rangle & \langle y'\delta \rangle \\ \langle xz \rangle & \langle x'z \rangle & \langle yz \rangle & \langle y'z \rangle & \langle z^2 \rangle & \langle z\delta \rangle \\ \langle x\delta \rangle & \langle x'\delta \rangle & \langle y\delta \rangle & \langle y'\delta \rangle & \langle z\delta \rangle & \langle \delta^2 \rangle \end{pmatrix}. \tag{4.1}$$

u_k stands for the distance along the k^{th} coordinate axis. Specifically,

$$\boldsymbol{u} \equiv \begin{pmatrix} u_1 \\ u_2 \\ u_3 \\ u_4 \\ u_5 \\ u_6 \end{pmatrix} = \begin{pmatrix} x \\ x' \\ y \\ y' \\ z \\ \delta \end{pmatrix}, \tag{4.2}$$

x, y and z are the horizontal, vertical, and longitudinal coordinates respectively, and prime designates the derivative with respect to s. Here, σ represents the 6×6 matrix, with elements σ_{ij}. The averages are taken over the phase space variables, and the subscripts i, j run from 1 to 6 representing x, x', y, y', z, z'. The time evolution of a beam matrix σ_s from s_0 to s_1 along the longitudinal position s is given by $\sigma_{s_1} = R(s_0 \to s_1)\, \sigma_{s_0}\, R^{\mathsf{T}}(s_0 \to s_1)$ [61, 62, 63], where R is the transport matrix. The space charge kick is implemented as

$$R\big(s_0, s_0 + \Delta s\big) = R_{\Delta s} R^{\mathrm{sc}},$$

where $R_{\Delta s}$ is a drift of length Δs and R^{sc} is the space charge kick (Eq. (A.3)) as described in Refs. [61, 62, 63]. For details see appendix A.

The Twiss parameters for a beam distribution can be expressed in terms of second moments and beam matrix elements (see also Eq. (2.42)):

$$\beta_x = \frac{\langle x_\beta^2 \rangle}{\epsilon_x} = \frac{\sigma_{11} - \sigma_{16}^2}{\epsilon_x}, \quad \alpha_x = -\frac{\langle x_\beta x'_\beta \rangle}{\epsilon_x} = -\frac{\sigma_{12} - \sigma_{16}\sigma_{26}}{\epsilon_x}, \tag{4.3}$$

where ϵ_x is the horizontal rms emittance. Similar expressions can be written along the vertical plane for β_y and α_y. The dispersion and its derivative are written in terms of beam matrix elements by comparing Eq. (4.1) with Eq. (2.41):

$$D = \frac{\sigma_{16}}{\sigma_{66}}, \quad D' = \frac{\sigma_{26}}{\sigma_{66}}. \tag{4.4}$$

For an ERL beamline, the optimization parameters are usually the quadrupole strengths. Optimization of a non-periodic lattice with multiple constraints leads to nonlinear and implicit objective functions for which numerical solutions are required. In the case of an ERL beamline, the objective function depends on the beam matrix elements corresponding to the Twiss parameters, and dispersion at the end of the arc, Eq. (4.3) and Eq. (4.4). With a search algorithm ("random walk") [64], a first trial solution is computed, and then the solution is subsequently improved, based on the corresponding objective function value until convergence, to get the matched solution.

The microbuncing instability gain (Eq. (3.33)) can be obtained at any location in a beamline by computing R_{56}, σ_δ, and r_b from the beam matrix tracking with space charge.

4.2 ELEGANT Particle Tracking

ELEGANT stands for "ELEctron Generation ANd Tracking," a somewhat out-of-date description of a fully 6D accelerator tool that now does much more than generate particle distributions and track them [27]. ELEGANT is written in the C programming language. It uses a variant of the MAD-X input format to describe the accelerator beamline and namelist-like format commands to execute the program. ELEGANT is very robust and flexible because it uses SDDS Toolkit [65] for pre- and post-processing, graphical and text output, sophisticated data analysis, and to link multiple codes and simulations.

ELEGANT can track 6-dimensional phase spaces using matrices up to third order, canonical kick elements, numerically integrated elements, or any combination thereof. A wide variety of output data is available from tracking, including centroid and sigma-matrix output along the accelerator. Besides tracking internally generated particle distributions, ELEGANT can track distributions stored in external files generated by other programs or by previous ELEGANT runs. It can also optimize the user-supplied functions obtained from matrices, particle tracking, Twiss parameters, etc. Several elements in ELEGANT support simulation of collective effects, such as the longitudinal space charge

impedance, transverse space charge kicks, wakefields, coherent synchrotron radiation.

Further in subsection 4.2.1, a brief introduction of the transverse and longitudinal space charge models in ELEGANT is given. The steps to compute the space-charge-induced microbunching instability gain in ELEGANT are explained in subsection 4.2.2.

4.2.1 Space Charge Models in ELEGANT

ELEGANT has an option to apply linear and non-linear directed transverse space-charge forces derived from Bassetti's formula [66, 67]. Transverse space charge simulations in ELEGANT are self-consistent. Therefore, they can work with other features provided by ELEGANT such as longitudinal space charge kicks and damping. Since in this work we are studying the effects of the linear space charge only, our discussions will be limited to linear space charge studies in ELEGANT. The expressions for linear space-charge force in ELEGANT are [27]:

$$\Delta x' = \frac{K_{\mathrm{sc}} L e^{-z^2/\left(2\sigma_z^2\right)}}{\sqrt{2\pi}\sigma_z} \frac{x}{\sigma_x\left(\sigma_x + \sigma_y\right)}, \tag{4.5a}$$

$$\Delta y' = \frac{K_{\mathrm{sc}} L e^{-z^2/\left(2\sigma_z^2\right)}}{\sqrt{2\pi}\sigma_z} \frac{y}{\sigma_y\left(\sigma_x + \sigma_y\right)}. \tag{4.5b}$$

Here, $\sigma_{x,y,z}$ are the rms beam sizes, L is the integrating length, and $K_{\mathrm{sc}} = \frac{2Nr_e}{\gamma^3\beta^2}$ is the space charge perveance with $r_e = 2.817\,940\,326\,2\,\mathrm{fm}$ as the classical electron radius.

These space-charge forces (Eq. (4.5)) are computed and applied on the simulated particles using a SCMULT element in ELEGANT. It is possible to add SCMULT directly into the beamline or through a command line using *insert_sceffects*. This aspect to add SCMULT elements depending on the problem allows greater flexibility in the simulations as it is easier to add the space-charge kicks anywhere in the beamline. The beam parameters and distance between the SCMULT kicks should be implemented carefully in a script, since kick strength is adjusted dynamically according to the instantaneous beam parameters.

To simulate the longitudinal space charge effects in ELEGANT, it has a drift element LSCDRIFT and an RF cavity element RFCW. The exact form of the longitudinal space charge impedance in Eq. (3.31) is used in a kick-drift-kick (or kick-accelerate-kick) algorithm. The distance between the kicks must be set properly to obtain valid results. The details can be found in Ref. [25].

The kick-drift-kick algorithm is explained as follows. Transport a bunch in the beamline and make a current histogram. Take the fast Fourier transformation (FFT) of the current histogram. Then, use the low-pass filter to remove high-frequency numerical noise. Examine the FFTs and multiply the filtered FFT by the impedance and take the inverse Fourier transformation of the result. This gives the voltage as a function of the bin in the original current histogram. Apply this voltage to each particle with interpolation between bins to make a smoother result [25, 68].

4.2.2 Microbunching Instability Computation in ELEGANT

Within this work, the microbunching instability simulations were not based on arbitrarily chosen simulation parameters but got from careful convergence tests on various simulation parameters including number of macroparticles, longitudinal space charge bins, and the number of integration kicks.

The numerical setting of the macroparticle number aims to reduce numerical noise due to a very limited number of simulation particles used in the tracking simulation. The setting of the number of integration kicks ensures the convergence of numerical error because of finite or discrete mesh. In addition, since we quantify the phase space modulation in frequency domain, i.e. Fourier transformation of the bunch current density, band-pass filtering maybe needed to ensure the suppression of undesired or nonphysical signals. It is also important to control the noise originating from the finite size of the mesh and the binning noise of a histogram [22]. We follow the numerical settings to simulate space-charge induced microbunching instability as described in Ref. [69]. The steps to compute the space charge induced microbunching instability are as follows:

1. Prepare a bunch with initial density modulations using smoothDist6 [27] for performing microbunching instability gain studies. smoothDist6 also increases the number of particles in a particle input file by sampling a simplified distribution based on the input file. The intention to increase the number of particles produced by a photoinjector simulation is to improve the stability of longitudinal space charge simulations. The detailed algo-

rithm is explained in Refs. [27, 69]. The expression for a small density modulation is defined as:

$$\lambda(t) = \lambda_0 \left(1 + d_{\mathrm{m}} \cos \frac{2\pi}{\lambda_{\mathrm{m}}} z \right),$$

where d_{m} is the modulation amplitude and λ_{m} is the modulation wavelength.

2. Insert WATCH elements to store the bunch information at specific locations in the beamline and start tracking.
3. Use sddsbunchingfactor tool to compute the bunching factors for beams from ELEGANT, for example, from previously inserted WATCH elements in coordinate mode. The bunching factor in ELEGANT is defined as:

$$B(\omega) = \frac{1}{N} \sqrt{\left(\sum_{i=1}^{N} \cos \omega t_i \right)^2 + \left(\sum_{i=1}^{N} \sin \omega t_i \right)^2},$$

where ω is the modulation angular frequency and t_i is the time coordinate of the i^{th} of N particles.

4. Compute the microbunching gain using Eq. (3.28) for a particular wavelengths density modulation at a specific location in the beamline.

To get a spectral gain curve that is $G(\lambda)$ as a function of modulation wavelength λ, one should repeat the above steps for a series of beam distributions with different initial modulation wavelengths.

4.3 Comparison of Beam Matrix and ELEGANT Particle Tracking

In this section, we compare the beam matrix tracking and particle tracking simulations in ELEGANT with and without space charge. As an example, we use a symmetrical beamline consisting of two double-bend achromats (DBA). The reason to consider a DBA structure for comparison is because of its similarity with an ERL beamline which also have zero dispersion and a finite value of momentum compaction. For comparison, we use the proposed beam parameters for MESA listed in Table 1.1.

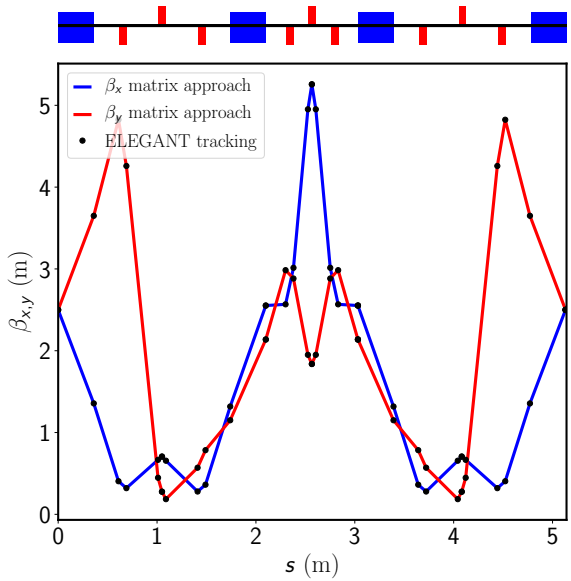

Figure 4.1.: Comparison of horizontal and vertical beta functions obtained from beam matrix approach and ELEGANT along the example beamline. Here, the blue rectangles above the plot illustrate dipole bends, and red rectangles are focusing or defocusing quadrupoles.

First, we compare the horizontal and vertical beta functions $\beta_{x,y}$ along the example beamline obtained from the beam matrix approach and particle tracking in ELEGANT as shown in Fig. 4.1. Figure 4.2 shows the comparison of horizontal dispersion D_x and momentum compaction R_{56} along the beamline. It can be concluded that there is no discrepancy between the lattice parameters obtained from the beam matrix approach and ELEGANT.

Second, we compute the horizontal and vertical beam envelopes along the example beamline for 1 mA and 10 mA current and an rms momentum deviation of 10^{-4}, accounting space charge. Figure 4.3 shows a good agreement between the beam matrix tracking results and ELEGANT particle tracking simulations with space charge.

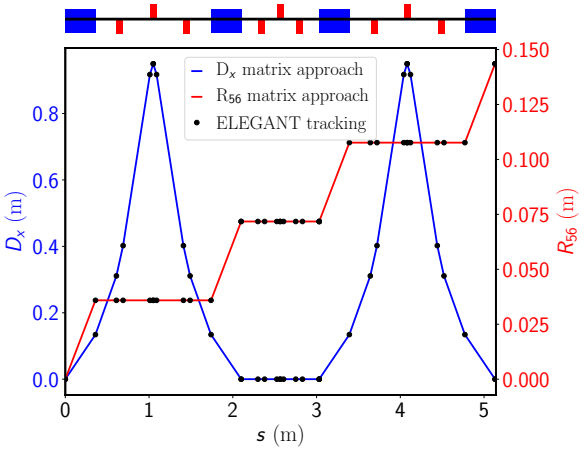

Figure 4.2.: Comparison of horizontal dispersion D_x and momentum compaction R_{56} obtained from beam matrix approach and ELEGANT particle tracking along the beamline.

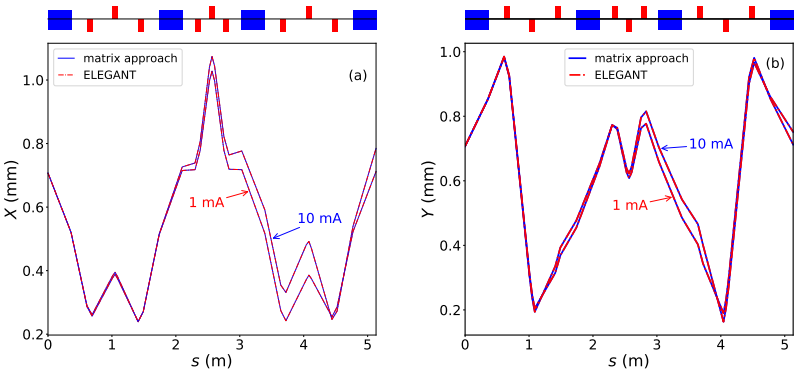

Figure 4.3.: Evolution of (a) horizontal beam envelope, and (b) vertical beam envelope along the beamline obtained from the beam matrix approach and ELEGANT for 1 mA and 10 mA current for $\sigma_\delta = 10^{-4}$.

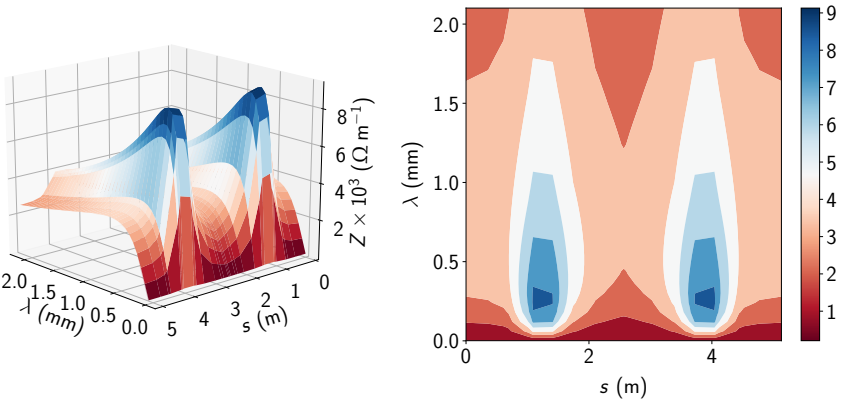

Figure 4.4.: Longitudinal space charge impedance as a function of modulation wavelength (3D view on left and top view on right) along the example beamline.

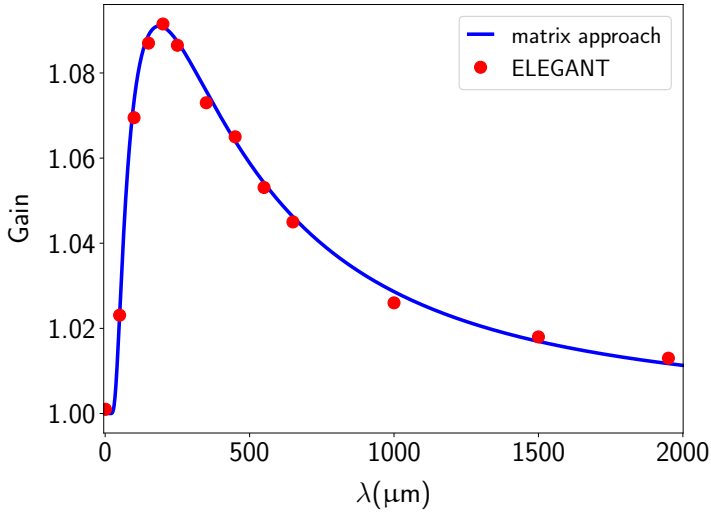

Figure 4.5.: Comparison of space charge induced microbunching instability gain spectrum obtained from matrix approach using Eq. (3.33) and ELEGANT using 3 M particles for I = 10 mA at the end of the example beamline.

Third, we obtain the longitudinal space charge impedance using Eq. (3.31) as a function of initial modulation wavelength λ along the example beamline as shown in Fig. (4.4). Since impedance is a function of modulation wavelength (see Eq. (3.31)), an accurate gain analysis requires scanning of the spectral range of modulation wavelengths. It can be seen that the impedance has maximum values for $\lambda = 200 - 300\,\mu$m at the location of the smallest beam radius r_b. It can be expected that gain will be maximal between this wavelength limit because there is no momentum chirp and compression in the beamline. Figure 4.5 shows the comparison of space charge induced microbunching instability gain spectrum obtained using Eq. (3.33) and ELEGANT using 3 M particles for I = 10 mA at the end of the example beamline. Our elaborations demonstrate a good agreement between the theoretical model and ELEGANT.

5 Beam Matching with Space Charge in Energy Recovery Linacs

It is essential to understand the details of space-charge-induced effects to maintain beam quality throughout the machine for intense electron bunches at low to medium energy traversing through bends. Particularly, current dependent matching of an arc into the subsequent RF structure has been found to be essential to preserve the beam quality. Figure 5.1 shows the matching lattice section of an accelerator which transforms the "input" beam parameters from one section of the accelerator into the specified "output" beam parameters for the next section of the accelerator. Beam matching with space charge has been discussed mostly in the context of high intensity beams in conventional linacs and synchrotrons [2, 36]. For example, the effect of transverse space charge on the dispersion function has been a topic of very active research for many years [46, 47, 70]. Current dependent non-zero dispersion might lead to emittance growth in the RF structure because of longitudinal-transverse phase space coupling.

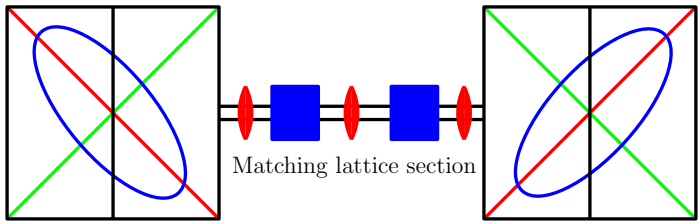

Figure 5.1.: Matching lattice section transforms the "input" beam parameters from one section of the accelerator into the specified "output" beam parameters for the next section of the accelerator.

Beam dynamics studies including dispersion and space charge has been studied by VR [46] and LO [47]. They independently derived equations, describing the beam envelopes together with the dispersion function under the influence of linear space charge forces as discussed in subsection 3.3.2. Theoretical aspects of beam matching with space charge and dispersion have been discussed in [49, 61, 71, 72]. For example, [61, 71] outlined the concept of two different dispersion functions, one for the beam center, which is not affected by space charge, and one for the off-center particles. Experiments related to space charge and dispersion with low energy proton beams were performed in the CERN PS Booster, matching the beam from the linac into the synchrotron. Although the space charge was found to be relevant, it was sufficient to use the zero-intensity dispersion for the matching of the beam center, in order to improve the injection efficiency [73].

An important role of the recirculation arc in an ERL is to provide path length adjustment options to set the accurate required RF phase of 0° to 180° for acceleration and deceleration. Transverse space charge modifies the dispersion function along the arc and so the momentum compaction which is the transport matrix element R_{56} for the individual particles. In case the arc settings are chosen for zero-intensity, one would end up with a dispersion and bunch length different from the design values at a subsequent RF structure. It is therefore necessary to understand the modification of dispersion due to space charge along the arc in order to do proper matching into the next lattice section. Longitudinal space charge also plays an important role, especially for short bunches and small momentum deviations. Longitudinal space-charge-induced variations in the bunch length or momentum deviation also affect the transverse space charge force by varying the local current density and the transverse beam size through the dispersion.

Because internal target experiments at MESA demand small momentum deviation ($\approx 10^{-4}$), and moderate β functions ($\approx 0.5\,\mathrm{m}$) with very small transverse emittance at the interaction point (IP), we need a coupled transverse-longitudinal beam matrix approach to optimize the lattice settings for the given intensity parameters. In this chapter, we focus on the optimized settings for the MESA low energy (5 MeV) injection arc (MARC0), used also as a bunch compressor, which will be crucial to achieve the desired beam parameters at the IP. We optimized the injection arc for two different cases, first case with small initial momentum deviation 1×10^{-4} and bunch length of 4.2 ps, and second case with an initial momentum chirp -7% and the much larger initial momentum deviation of 4×10^{-3}. In subsequent recirculation arcs of MESA, the beam energy is much higher than the injection energy. Therefore, space

charge defocusing reduces accordingly. Thus, we will limit our discussions in this chapter to the MARC0 optimization only and discuss the further effects in chapter 6.

In this chapter, it is shown that the space-charge-modified dispersion plays a key role for the adjustment of the R_{56} required for both the isochronous and the non-isochronous recirculation mode of an ERL. A longitudinal bunch envelope equation has been derived by Neuffer [44]. In Refs. [36, 51, 74] this equation has been used to predict bunch lengths with space charge and momentum compaction in synchrotrons. For simplified estimates we use this approach to predict the momentum deviation evolution along the arc, which in turn affects the transverse beam size, dispersion, and R_{56}.

This chapter is organized as follows: the basic relations for the beam centroid, rms beam size, and dispersion are explained with and without space charge in section 5.1. Section 5.2 outlines the transverse envelope-dispersion equations and transverse smooth approximation applied to the different operation modes of MESA, respectively, followed by a longitudinal analytical model to obtain an analytical expression for the final momentum deviation in terms of initial beam and machine parameters in section 5.3. Results and parameter adjustments for beam matching with space charge from the MESA injection arc (MARC0) into the first RF structure (section 1.3) are discussed in sections 5.4–5.5 with the presented beam matrix approach and ELEGANT particle tracking [27]. The content of this chapter is partially adapted from the author's publication [7].

5.1 Dispersion with Space Charge

In the presence of bending magnets, the horizontal displacement x of a particle from the reference particle in Eq. (2.36) with space charge is written as

$$x_{\mathrm{sc}}(s) = x_{\mathrm{sc},\beta}(s) + D\delta, \tag{5.1}$$

where $D \equiv D_x(s)$ is the dispersion function with space charge.

Taking the average of Eq. (2.36) and Eq. (5.1) and subtracting them over the symmetrical phase space distribution, such that $\langle x_\beta \rangle = \langle x_{\mathrm{sc},\beta} \rangle = 0$, we obtain (see also [71]):

$$\langle x_{\mathrm{sc}} \rangle - \langle x \rangle = (D - D_0)\langle \delta \rangle. \tag{5.2}$$

For a beam with a momentum distribution centered at the design momentum the dispersion describing the position of the beam centroid is space charge independent. This also explains the experimental results obtained in the CERN PS Booster [73]. There the dispersion was measured and matched by changing the beam momentum and recording the displacement of the beam center.

To observe the effect of space charge on the individual particle dispersion, we have to compute the second moments of the beam distribution. Using the assumption that the momentum deviation is uncorrelated to the betatron oscillations, such that $\langle x_\beta \delta \rangle = \langle x_{sc,\beta} \delta \rangle = 0$, we get the expression for D by multiplying Eq. (5.1) by δ and taking the average over the phase space. Following a similar procedure for D', one can derive:

$$D = \frac{\langle x_{sc} \delta \rangle}{\langle \delta^2 \rangle}, \quad D' = \frac{\langle x'_{sc} \delta \rangle}{\langle \delta^2 \rangle}. \tag{5.3}$$

Equation (5.3) gives the dispersion with space charge and is equivalent to Eq. (2.41) which gives the dispersion without space charge. Similarly, we can get the expressions for path length with space charge by inserting space charge dispersion Eq. (5.3) in Eq. (2.49):

$$R_{56} = \frac{\Delta L}{\delta} = \int_0^L \frac{D}{\rho} \mathrm{d}s. \tag{5.4}$$

The above expressions define the modification of dispersion and path length for individual particles in a beam affected by space charge. In this work, we use a beam matrix approach as well as particle tracking to obtain the optical functions along a beamline with bends, including the self-consistent space charge force. However, for a qualitative analysis and to obtain approximate scaling laws with intensity, it is convenient to derive simplified expressions from the envelope equations with space charge.

5.2 Smooth Approximation with Dispersion and Space Charge

The envelope equations discussed in subsection 3.3.2 are used in this section to obtain simplified scaling laws for the beam radii and dispersion as a function of the space charge parameter.

First, the system of envelope-dispersion equations is written in the smooth approximation (see also [72, 71]). In smooth approximation $\kappa_{x,y}$ as well as the lattice functions are independent of s. One can obtain the simplified scaling laws for the beam radii and dispersion as a function of the space charge parameter. Assuming a matched beam $\sigma^{''}_{x,y}, D^{''} = 0$, the envelope-dispersion equations are:

$$\left(\kappa_0 - \frac{K_{\rm sc}}{2a(a+b)}\right) D - \frac{1}{\rho} = 0, \tag{5.5a}$$

$$\left(\kappa_0 - \frac{K_{\rm sc}}{2a(a+b)}\right) \sigma_{x_0} - \frac{\epsilon_x^2}{\sigma_{x_0}^3} = 0, \tag{5.5b}$$

$$\left(\kappa_0 - \frac{K_{\rm sc}}{2b(a+b)}\right) \sigma_{y_0} - \frac{\epsilon_y^2}{\sigma_{y_0}^3} = 0, \tag{5.5c}$$

where κ_0 is the averaged constant focusing strength, D is the average horizontal dispersion, ρ is the average bending radius, σ_{x_0,y_0} are the average rms betatron amplitudes, a, b are the average effective rms beam radii, and ϵ_x is the horizontal emittance which is conserved in the presence of linear dispersion.

By defining horizontal and vertical space charge intensity parameters as follows:

$$\chi_{x\sigma_\delta} \equiv \sqrt{1 - \frac{K_{\rm sc}}{2a(a+b)\kappa_0}}, \quad \chi_{y\sigma_\delta} \equiv \sqrt{1 - \frac{K_{\rm sc}}{2b(a+b)\kappa_0}}. \tag{5.6}$$

The range of space charge intensity parameters is between 0 and 1. It has value 1 for zero intensity and 0 for space charge dominated limit.

Equations (5.5a)–(5.5c) can now be rewritten in a more compact form by using Eq. (5.6):

$$\chi_{x\sigma_\delta}^2 \kappa_0 D - \frac{1}{\rho} = 0 \implies D = \frac{D_0}{\chi_{x\sigma_\delta}^2}, \tag{5.7a}$$

$$\chi_{x\sigma_\delta}^2 \sigma_{x_0} - \frac{\epsilon_x^2}{\kappa_0 \sigma_{x_0}^3} = 0 \implies \sigma_{x_0}^2 = \frac{a_0^2}{\chi_{x\sigma_\delta}}, \tag{5.7b}$$

$$\chi_{y\sigma_\delta}^2 \sigma_{y_0} - \frac{\epsilon_y^2}{\kappa_0 \sigma_{y_0}^3} = 0 \implies \sigma_{y_0}^2 = \frac{a_0^2}{\chi_{y\sigma_\delta}}, \tag{5.7c}$$

where $a = \sqrt{\sigma_{x_0}^2 + (D\sigma_\delta)^2}$ and $a_0 = \sqrt{\epsilon_x/\sqrt{\kappa_0}}$. Assuming a round beam (a $\approx$ b) in the limit of small momentum deviation and arbitrary space charge $\left(D\sigma_\delta\right)/\sigma_{x_0} \ll 1$ results in $\chi_{x\sigma_\delta} = \chi_{y\sigma_\delta} = \chi$.

An expression for momentum compaction in the presence of space charge is obtained by substituting the obtained expression for the dispersion from Eq. (5.7a) into Eq. (2.49):

$$R_{56} = \frac{D_0 L_d}{\chi^2 \rho}, \tag{5.8}$$

where L_d is the total length of the dispersive element. The last equation is important for the ERL design, since it gives the scaling of momentum compaction with intensity. We illustrate Equations (5.7) and (5.8) for parameters relevant to the MESA injection arc. The first three columns in Table 5.1 list the main beam parameters after the injector at 5 MeV [75]. The last four columns list the obtained horizontal beam radii, normalized to a_0, and the momentum compaction for two rms momentum deviations $\sigma_\delta = 0, 0.4\,\%$ (see section 5.5 for a discussion of the MESA beam parameters).

Figure 5.2 shows the results for the normalized horizontal beam radius a/a_0 (using Eq. (5.7b)) and momentum compaction Eq. (5.8) as a function of space charge parameter χ for four values of a dimensionless parameter $\xi_0 = D_0\sigma_\delta/a_0 = 0$ (no momentum deviation), 1.59, 2.10 or 2.76 for 0.4 % momentum deviation. Also results shown by dots on Fig. 5.2 are obtained using the matrix approach (explained in section 5.5) for three different cases of MESA beams ($\sigma_\delta = 0.4\,\%$) referred to in Table 5.1. The results using the smooth approximation are in good agreement with the matrix approach results for the listed values of momentum deviation. In conclusion, the full solution

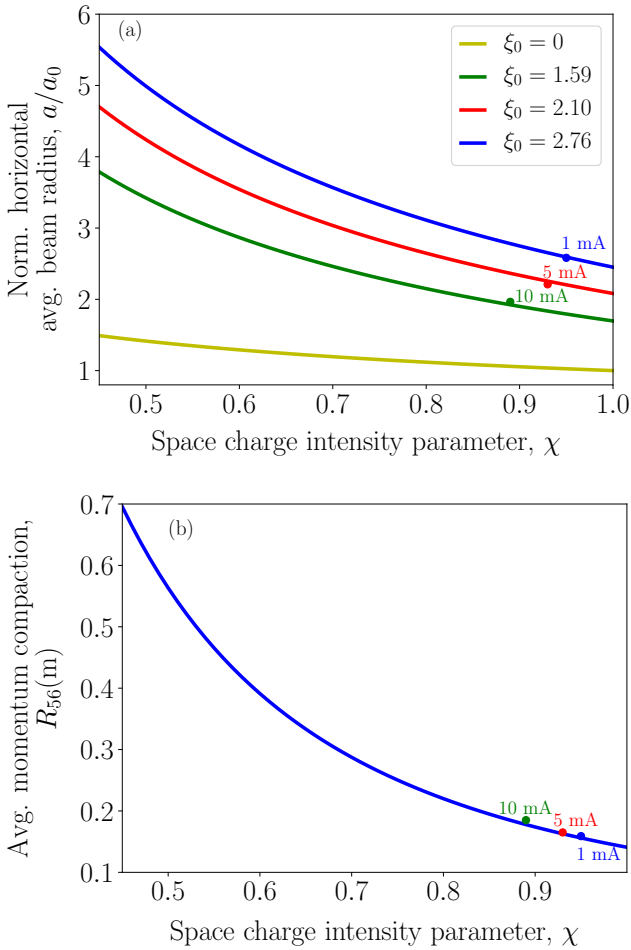

Figure 5.2.: (a) Horizontal beam radius, and (b) momentum compaction as a function of the space charge intensity parameter χ for four values of $\xi_0 = D_0\sigma_\delta/a_0$. $\sigma_\delta = 0$ for first case (yellow line) and $\sigma_\delta = 0.4\,\%$ for the other three cases in the presence of space charge.

I (mA)	$\epsilon_{nx}(\mu\text{m})$	χ	a/a_0	R_{56} (m)	a/a_0	R_{56} (m)
			$\sigma_\delta = 0$		$\sigma_\delta = 0.4\,\%$	
0.0	2.0	1.00	1.0	0.140	2.45	0.140
1.0	2.0	0.95	1.025	0.159	2.58	0.140
5.0	3.5	0.92	1.042	0.165	2.21	0.138
10.0	6.0	0.89	1.059	0.185	1.97	0.134

Table 5.1.: Example current, normalized emittance and space charge parameter after the MESA injector at 5 MeV together with the beam radii and momentum compaction from Eq. (5.7b) and Eq. (5.8) for different momentum deviations.

with discrete focusing agrees with the smooth approximation for the MARC0 optics.

If the longitudinal space charge force can be neglected (see next section and section 5.5), the half bunch length at the end of the beamline, including the transverse space charge, can be obtained using Eq. (5.8) as

$$z_\mathrm{f} = z_\mathrm{i} + R_{56}\sigma_\delta, \tag{5.9}$$

where z_f and z_i are the initial and final half-bunch length, respectively.

5.3 Longitudinal Envelope Model

In an ERL beamline one can expect longitudinal-transverse coupling due to the space charge force and dispersion. In our numerical beam matrix and particle tracking approaches, coupling effects are taken into account. A simplified approach within a longitudinal envelope model is complicated by the variation of the local phase slip factor $\eta(s)$. However, if we use the constant η obtained from the smooth focusing approximation, discussed in the previous section, we can employ the well established longitudinal envelope equation (see for example [44]) with the slowly varying momentum compaction:

$$\eta = \frac{D_0}{\chi^2\rho}. \tag{5.10}$$

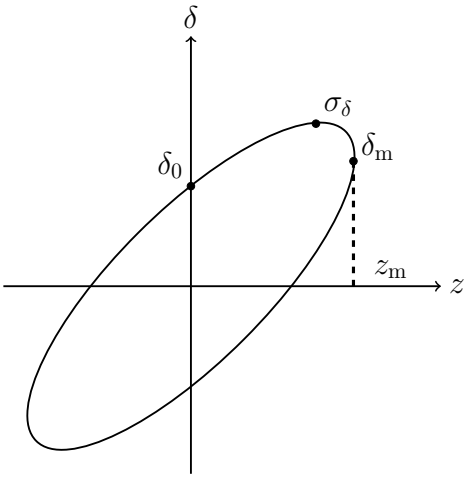

Figure 5.3.: Description of rotated ellipse of longitudinal phase space z, δ. $\delta_0 = (\delta p/p_0)_0$ is the maximum momentum deviation at the center, $\delta_\mathrm{m} = (\delta p/p_0)_\mathrm{m}$ is the momentum deviation at the bunch ends, and $\sigma_\delta = (\delta p/p_0)$ is the maximum momentum deviation of the bunch.

The longitudinal envelope equation for half-bunch length $z_\mathrm{m}(s)$ (Eq. (3.23)) without RF focusing is then:

$$z_\mathrm{m}'' - \frac{K_\mathrm{l}}{z_\mathrm{m}^2} - \frac{\epsilon_\mathrm{l}^2}{z_\mathrm{m}^3} = 0. \tag{5.11}$$

For an arbitrary ellipse of the longitudinal phase space (z, δ), where $\delta_0 = (\delta p/p_0)_0$ is the maximum momentum deviation at the bunch center, and $\delta_\mathrm{m} = (\delta p/p)_\mathrm{m}$ is the momentum deviation at the bunch ends as shown in Fig. 5.3. By using

$$z' = -\eta\left(\delta p/p_0\right),$$

the total momentum deviation $\sigma_\delta = \delta p/p_0$ is [51]:

$$\sigma_\delta = \delta_0^2 + \delta_\mathrm{m}^2 = \sqrt{\left(\frac{\epsilon_\mathrm{l}}{\eta z_\mathrm{m}}\right)^2 + \left(\frac{z_\mathrm{m}'}{\eta}\right)^2}. \tag{5.12}$$

In the absence of RF kicks $\kappa_{z_0} = 0$ in a beamline, a longitudinal invariant I_l is obtained by multiplying Eq. (5.11) by z'_m and integrating with respect to s:

$$I_\mathrm{l} = \frac{{z'_\mathrm{m}}^2}{2} + \frac{K_\mathrm{l}}{z_\mathrm{m}} + \frac{\epsilon_\mathrm{l}^2}{2z_\mathrm{m}^2}. \tag{5.13}$$

Using Eq. (5.12), the longitudinal invariant I_l can now be written in terms of total momentum deviation as

$$I_\mathrm{l} = \frac{1}{2}\eta^2{\sigma_\delta}^2 + \frac{K_\mathrm{l}}{z_\mathrm{m}} \tag{5.14}$$

If $z_\mathrm{m,i}$ and $z_\mathrm{m,f}$ are the bunch lengths at the start and at the end of the beamline, respectively, then the conservation of I_l results in

$$\sigma_{\delta\mathrm{i}}^2 + \frac{2K_\mathrm{l}}{\eta^2 z_\mathrm{m,i}} = \sigma_{\delta\mathrm{f}}^2 + \frac{2K_\mathrm{l}}{\eta^2 z_\mathrm{m,f}}, \tag{5.15}$$

with $\sigma_{\delta\mathrm{i}}$ as the initial total momentum deviation at the start of the beamline and $\sigma_{\delta\mathrm{f}}$ as the final total momentum deviation at the end of the beamline. Rearranging Eq. (5.15), we find:

$$\frac{\sigma_{\delta\mathrm{f}}^2}{\sigma_{\delta\mathrm{i}}^2} = 1 + \frac{2K_\mathrm{l}}{\eta^2 z_\mathrm{m,i}\sigma_{\delta\mathrm{i}}^2}\left(1 - \frac{z_\mathrm{m,i}}{z_\mathrm{m,f}}\right). \tag{5.16}$$

Because space charge stretches the bunch length accordingly, we can neglect the $z_\mathrm{m,i}/z_\mathrm{m,f}$ on the right-hand side in Eq. (5.16) such that $z_\mathrm{m,f} >> z_\mathrm{m,i}$. The final expression for the total momentum deviation in terms of longitudinal space charge perveance, initial bunch length, and phase slip factor is obtained by rearranging Eq. (5.16):

$$\sigma_{\delta\mathrm{f}} = \sqrt{\sigma_{\delta\mathrm{i}}^2 + \frac{2K_\mathrm{l}}{\eta^2 z_\mathrm{m,i}}}. \tag{5.17}$$

In Section 5.4 Eq. (5.17) is compared to results obtained with beam matrix tracking (see solid blue line in Fig. 5.5).

5.4 Comparison of Analytical Models, Beam Matrix and Particle Tracking

In this section, the solutions for beam envelopes, dispersion and momentum compaction are presented with space charge. We compare beam matrix tracking results with particle tracking in ELEGANT. The implementation of transverse space charge in ELEGANT is briefly described in Ref. [67].

The MESA injection arc (MARC0) is used as an example case. An overview of the MESA facilities is shown in Fig. 1.2, for details see Section 1.3. MARC0 is a 5 MeV, 180°, first-order double bend achromat with flexible 1st order momentum compaction R_{56}, which is required for non-isochronous recirculating schemes and also to support the two different operation modes of MESA. By accelerating off-crest in the injector linac and adjusting R_{56} in the injector arc MARC0 is designed as a bunch compressor. Estimation of space charge effects is done for a typical set of beam parameters listed in Table 1.1. Note that we are using an idealized lattice for the MARC0 ignoring magnet misalignments and multipole errors for the simulations. Additional studies are required to include these effects.

First, we compute the horizontal beam envelope, dispersion, and momentum compaction profile along the MARC0 arc for "zero" and 10 mA current and an rms momentum deviation of 10^{-4}, accounting for transverse space charge only. Figure 5.4 shows a good agreement between the beam matrix tracking results and ELEGANT particle tracking. As expected from Eq. (2.49), the variation in the dispersion due to space charge leads to a variation in the momentum compaction in Fig. 5.4(b)–(c).

Second, simulations are performed with longitudinal space charge to show the variation of the momentum deviation with current as shown in Fig. 5.5. The momentum deviation is computed from the beam matrix as $\sigma_\delta = \sqrt{\sigma_{66}}$. It can be seen that longitudinal space charge does not have much impact on the momentum deviation below I = 1 mA. At high beam current (I = 10 mA), there is a significant increase in momentum deviation by a factor of 5 at the end of the arc. The space-charge induced changes in the momentum deviation also affect the dispersion computed from second moments of beam distribution (see Eq. (4.4)). Therefore, it is important to consider the coupled transverse-longitudinal simulations to match the beam-based dispersion at high beam currents.

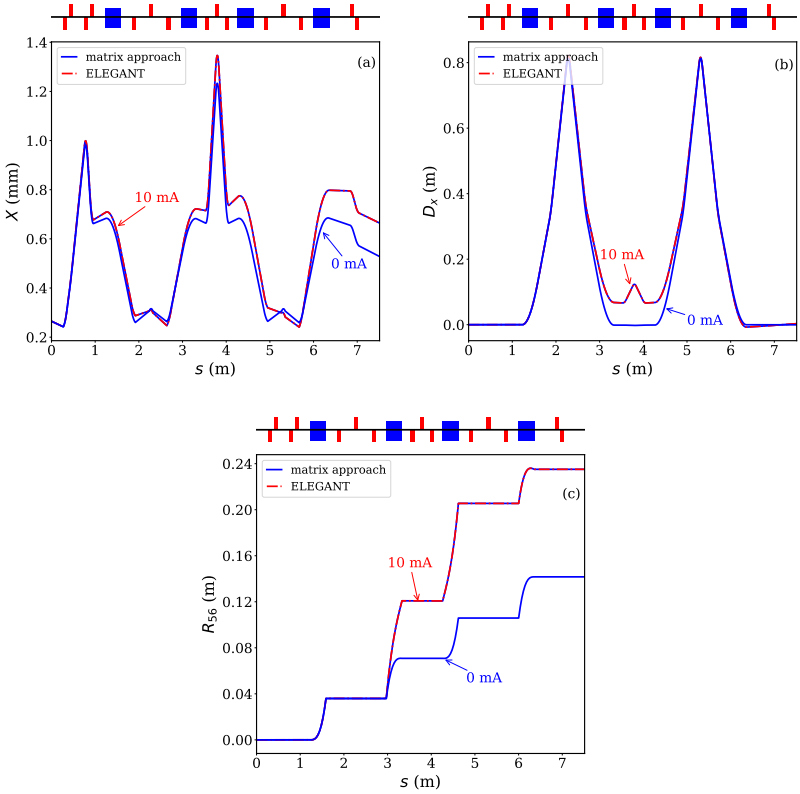

Figure 5.4.: Horizontal beam envelopes (a), dispersion (b), and momentum compaction (c) along the MARC0 beamline obtained from the matrix approach and ELEGANT for "zero" and 10 mA current for $\sigma_\delta = 10^{-4}$. Here, the blue rectangles illustrate dipole bends, and red rectangles are focusing or defocusing quadrupoles.

Figure 5.5 also shows reasonable agreement for the evolution of the momentum deviation between our simplified model Eq. (5.17) and beam matrix tracking Eq. (4.4). The small deviation between the simplified model and beam matrix tracking can be explained by the geometry factor in K_1. In our matrix tracking model, the beam radius is $r_b \equiv 1.7(\sigma_x + \sigma_y)/2$, and in the simplified

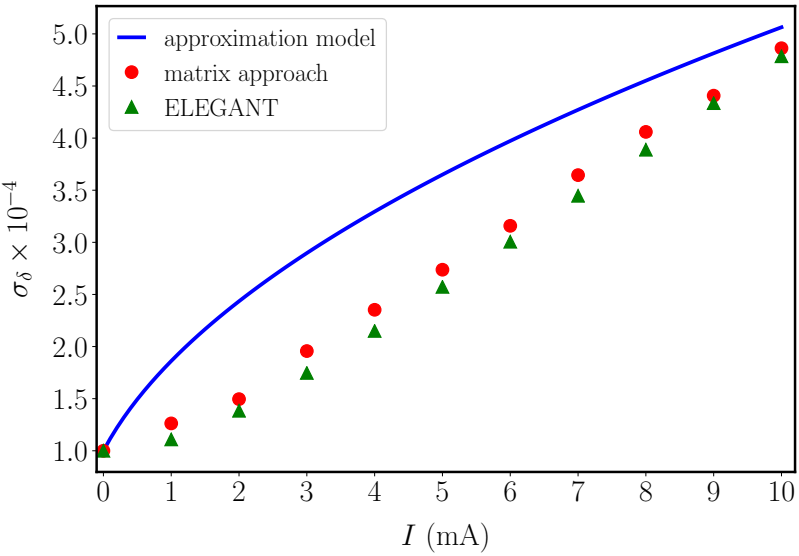

Figure 5.5.: The final total momentum deviation at the end of the MARC0 as a function of the beam current. A reasonable agreement between the matrix approach (red dots) and the approximation model following Eq. (5.17) (blue solid line) can be observed.

model an average value computed by smooth approximation Eq. (5.7) is used for the average beam radius a.

Equation (2.49) shows that the path length varies with D_x along the beamline. The variation of peak current with the bunch length modifies the transverse space charge perveance Eq. (3.16), and the longitudinal space charge perveance Eq. (3.24) depends weakly on the beam radius r_b. The transverse and longitudinal envelopes are therefore coupled. In the previous sections the simplified expressions are derived, without coupling.

Figures 5.6 (a)–(b) show the variation of horizontal and vertical transverse envelopes along s, for $I = 1$, and 10 mA in MARC0. It can be seen from Fig. 5.6 (c) that with longitudinal and transverse space charge the dispersion is significantly modified for non-zero currents. The sign reversal of D_x may contribute to phase mismatch at the entrance of the RF structure due

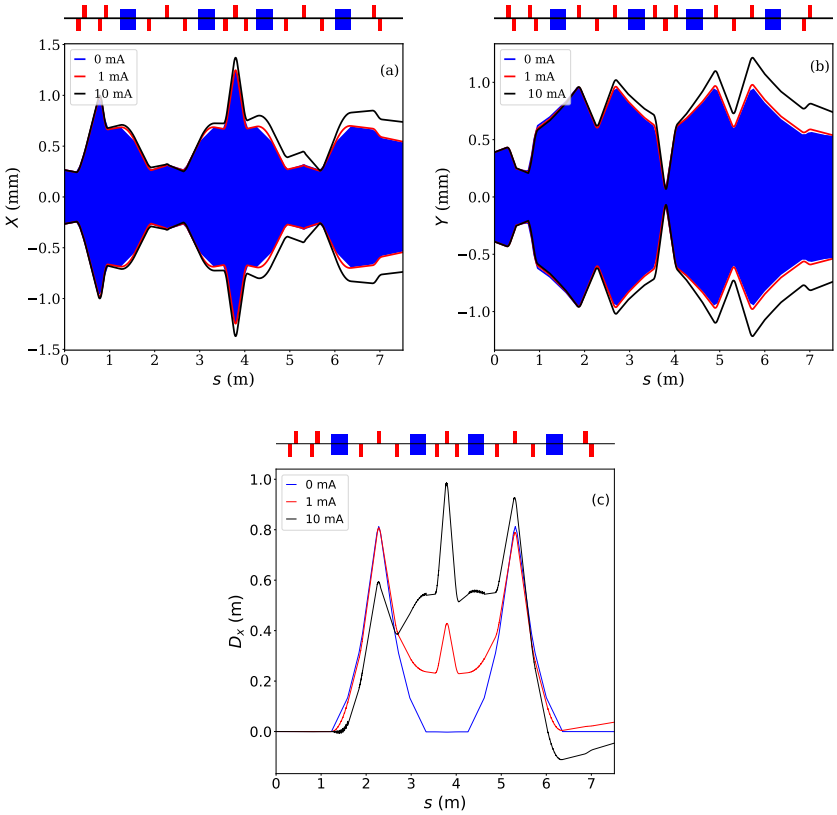

Figure 5.6.: Evolution of (a) horizontal beam envelope, (b) vertical beam envelope, and (c) dispersion along the MARC0 beamline for I = 0, 1, 10 mA including transverse and longitudinal space charge.

to changes in the time of flight of particles (see Eq. (2.49)). Thus, it is important to consider both longitudinal and transverse space charge for optimal matching.

5.5 Lattice Optimization and Discussions

In this work, we optimize the lattice parameters of MARC0 to get fixed values of $\beta_{x,y}, \alpha_{x,y}, D_x, D'_x$ and R_{56} at the end. While the transverse dispersion functions D_x and D'_x need to be zero at the end of the arc, the longitudinal dispersion is fixed at a finite value of $R_{56} = 0.14\,\text{m}$ in order to use the arc as part of a bunch compressor to achieve a short bunch length at the start of the first superconducting RF structure.

A multi-turn ERL with a split linac like MESA, explicitly demands that both the accelerating and the decelerating beams share the individual return arcs. This condition imposes symmetry about the RF structures. The return arcs accept two beams of the same energy — one will be accelerated and the other one will be decelerated — which requires a lattice with its symmetry axes in the middle of the RF structure. Additionally, the beta functions at the position of the RF structure need to be as small as possible to achieve maximum beam current. The main reason for this second requirement on the beam optics is to control the transverse beam break-up. Beam break-up is related to the excitation of unwanted dipole higher-order modes, which can be diminished by minimizing the beta functions and thus the beam size inside the RF structure [76].

For ER operation, the nominal design of the arc should deliver fixed beam parameters with zero transverse dispersion at the start of the RF structure. As can be seen in Fig. 1.2, only about 3.8 m of space is available for the 180° arc. This limits the number of knobs to adjust dispersion and Twiss parameters.

As can be seen from Fig. 5.6, MARC0 consists of two DBA [35]. It controls both transverse beam confinement and longitudinal phase space to compress the bunch. A set of four quadrupoles at the start of the arc matches the first DBA to the MAMBO injector. The central part of the arc between the two DBAs contains three quadrupoles to again match the Twiss parameters. A total of 15 quadrupole gradients are available knobs to optimize the lattice.

Table 5.2 illustrates the horizontal beta function mismatch $\Delta\beta_x/\beta_x$ and the vertical beta function $\Delta\beta_y/\beta_y$ mismatch from the design value respectively, and the horizontal dispersion mismatch ΔD_x from the design value at the end of MARC0 with space charge for 1, 5 and 10 mA. Here, $\Delta\beta_x = \beta_{\text{sc},x} - \beta_x$, $\Delta\beta_y = \beta_{\text{sc},y} - \beta_y$, and $\Delta D_x = D_{\text{sc},x} - D_x$. We can see from the last column of Table 5.2 that current dependent dispersion is non-zero at the end of MARC0 which might lead to emittance growth in the RF structure because of longitudinal-transverse phase space coupling.

I (mA)	$\frac{\Delta\beta_x}{\beta_x}$ (%)	$\frac{\Delta\beta_y}{\beta_y}$ (%)	ΔD_x(m)
1	3.0	2.6	0.037
5	17.5	17.3	-0.017
10	39.7	41.0	-0.046
10 (matched)	0	0	0

Table 5.2.: Example current, the horizontal and vertical beta functions mismatch respectively, and the horizontal dispersion mismatch from the design value at the end of MARC0 with space charge.

If all the lattice parameters of the beamline are set properly in the presence of space charge, the bunch length is 2 ps at the entrance of the RF structure.

A simple "random walk" routine is used to optimize all lattice parameters to get the matched solution of MARC0 with space charge. Note that D' should be considered for optimization of D in the beamline with space charge. D' must be zero at the central quadrupole of the achromat to achieve zero dispersion at the end of the last dipole. A new set of quadrupole strengths is obtained with corrections of up to 15% in the original quadrupole strengths to get the matched solution as shown in Fig. 5.7 which shows the variation of optimized quadrupole strengths for 10 mA to the original quadrupole strengths for 10 mA along the beamline. Here $\Delta\kappa = \kappa_{\text{original}} - \kappa_{\text{optimized}}$, and $\kappa \equiv \kappa_{x,y}$. As expected Fig. 5.7 shows that we need to focus against space charge more in the non-zero dispersion region. Afterwards matching the end of the MARC0 to the subsequent RF structure also demands to re-evaluate the quadrupole strengths.

In the second case, the longitudinal phase space is shaped within the MAMBO injector to achieve a linear correlation between the phase and energy of the particles. As discussed in section 1.3, the MESA ER mode is planned to be used for electron scattering experiments at an internal gas target for high-precision experiments. The final momentum deviation of less than 2×10^{-4} can be achieved in either isochronous or non-isochronous operation when the bunch length at injection into the first RF structure is small [4, 76].

Particle tracking simulations in Ref. [75] show that for a given longitudinal emittance in the presence of space charge, a beam optimized for a shorter bunch length with an increased momentum deviation at the start of the first RF structure yields a better momentum deviation at the internal target experiment energy (105 MeV) than vice versa. Therefore, the target rms values for

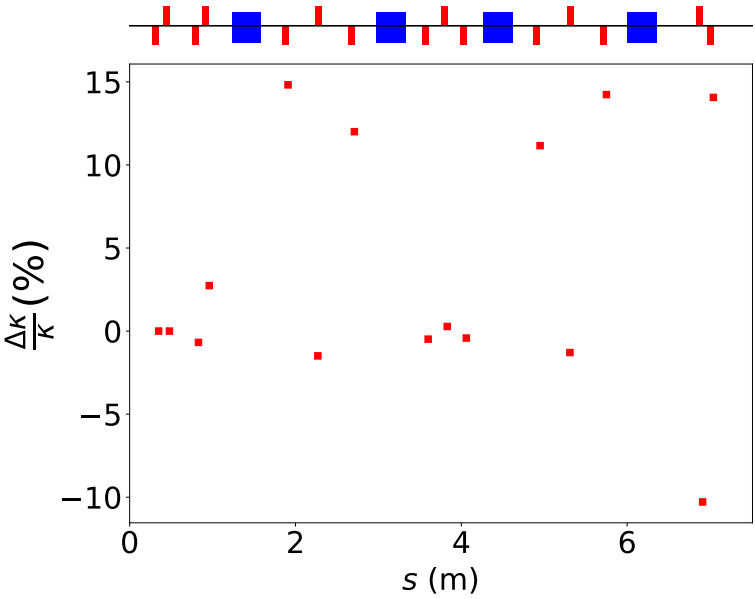

Figure 5.7.: Variation of optimized quadrupole strengths for 10 mA to the original quadrupole strengths for 0 mA along the beamline. Here $\Delta\kappa = \kappa_{\text{original}} - \kappa_{\text{optimized}}$, and $\kappa \equiv \kappa_{x,y}$.

longitudinal properties of the 5 MeV beam behind MARC0 can be defined to be less than 5×10^{-3} in momentum deviation and 2 ps in bunch length [75]. Thus, we use the bunch distribution with a momentum chirp of −7 % and a momentum deviation of 0.4 % at 1 mA, and 10 mA at the start of MARC0.

Figure 5.8 shows the momentum compaction has the designed value of around 0.14 m to get short bunch at the start of the first RF structure with space charge along the MARC0 beamline for a bunch with momentum chirp -7% and momentum deviation of 0.4% at 1 mA and 10 mA.

It can be concluded that by accelerating off-crest in the injector linac and adjusting R56 in the injection arc (MARC0) successfully works as a bunch compressor in the presence of linear space charge forces even at the highest peak beam current of 10 mA as can be seen in Fig. 5.9(b)–(c).

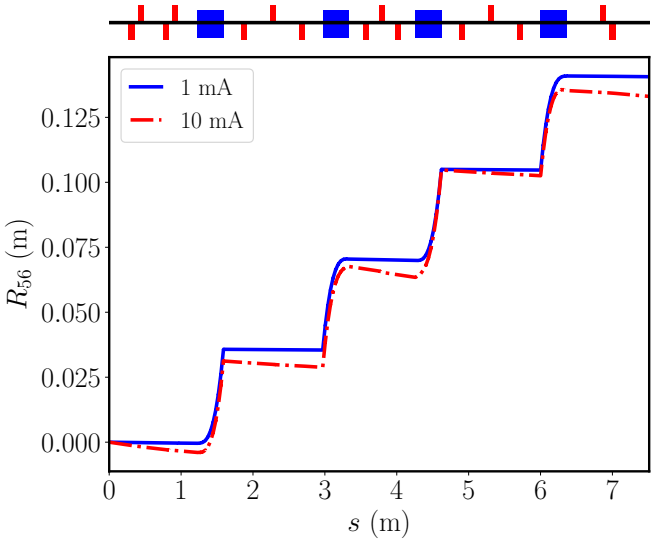

Figure 5.8.: Momentum compaction with space charge along the MARC0 beamline for a bunch with momentum chirp -7% and momentum deviation of 0.4% at 1 mA and 10 mA.

The nonlinearities outside the rms beam ellipse from matrix tracking (red ellipses) are expected from the fact that the red ellipses are obtained from the matrix approach with a linear space charge, which is assumed to be consistent for all beam particles.

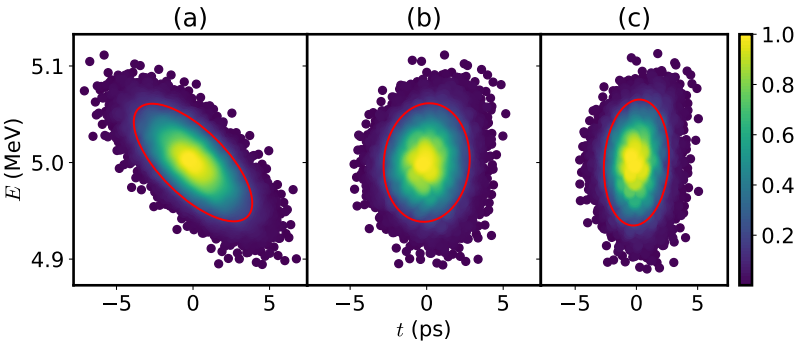

Figure 5.9.: Longitudinal phase spaces at (a) the start of MARC0, (b) the end of MARC0 for 1 mA of current, and (c) at the end of MARC0 for 10 mA. The red ellipses indicate the rms beam ellipse from matrix tracking.

Our relatively simple beam matrix tracking scheme, including space charge kicks, provides a valuable understanding of the beam envelopes, dispersion, and momentum compaction. We focused on the example of the MARC0 arc, but the same scheme applies to the MESA recirculation arcs and also to other ERLs for a qualitative analysis.

6 Application: Intensity Limitations in MESA

In this chapter, we briefly demonstrate the MESA facility and address the corresponding lattice design and beam dynamics challenges in section 6.1. The studies of intensity limitations due to space charge and microbunching instability are discussed in section 6.2 and section 6.3, respectively.

6.1 MESA Lattice and Challenges

The MESA lattice is designed symmetrical around the mirror plane of the main RF structures. As a result, a 5 MeV dump beamline on one side of the second RF structure is placed which is analogous to the 5 MeV injection arc placed next to the first RF structure. Spreaders and mergers are located directly after the RF structures to guide different energy beams to the same RF structure and then sent them back to the beamlines according to their energy after acceleration/deceleration. Each spreader starts with a vertical bending magnet to start the separation of the three beams. This vertical dispersion is suppressed by the quadrupoles located appropriately in the vertical stacking. Optimization of the MESA lattice is an ongoing process, as presented in Refs [29, 30]. Figure 6.1 shows the horizontal and vertical beta functions along the MESA beamline. The present lattice of MESA has the promising values of horizontal and vertical beam envelopes below 2 mm and 1.2 mm. In addition, Fig. 6.1 points out the location of the internal target experiment PIT with symmetrical beta functions β^*.

MESA lattice is designed and optimized to get the flexible momentum compaction because it is an important parameter to control the path length for ER mode and a factor that leads to the microbunching instability in the presence of initial shot noise and space charge [30]. Therefore, all 180° recirculation arcs are set up as achromats with the flexible momentum compaction optics. Figure 6.2 shows the horizontal and the vertical dispersion D_x and D_y respectively, and the momentum compaction R_{56} along the MESA beamline. The MESA lattice is set up to achieve the desired $R_{56} = 0.14\,\mathrm{m}$ for different opera-

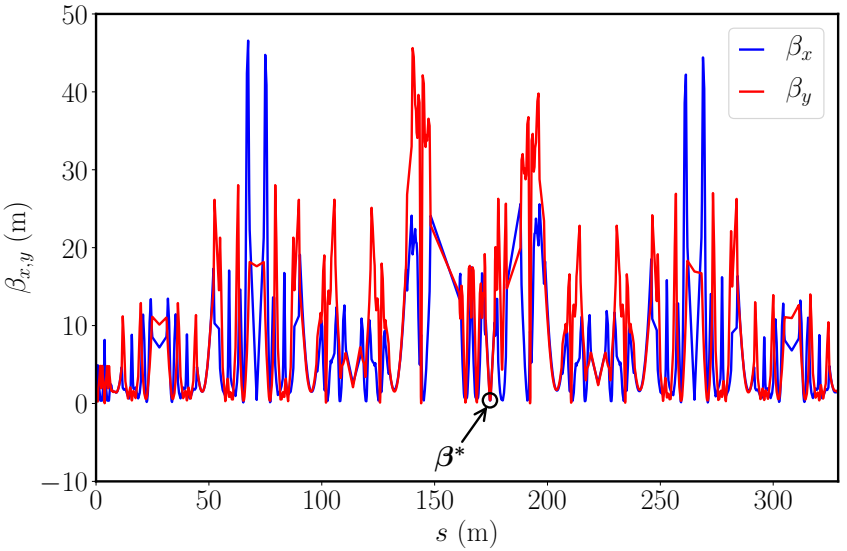

Figure 6.1.: Beta functions for the MESA full beamline operating in energy recovery mode. β^* is the location of the internal target experiment with symmetrical and small beta functions.

tional modes. It can also be seen from Fig. 6.2 that there is non-zero vertical dispersion due to the spreaders and mergers in the recirculation arcs next to the RF structures.

The path length of each recirculation arc in MESA is an integer number of RF wavelengths, except for the 105 MeV highest energy arc, whose length is longer by half of the RF wavelength to change the RF phase from accelerating to decelerating for energy recovery mode.

The first step to validate the machine design is the transport of a single bunch from the injector to the beam dump. Therefore, it is necessary to study the effect of space charge and intensity limitations throughout the machine. As discussed in chapter 5 space-charge-modified dispersion plays an important role in achieving the required beam parameters. In the previous chapter we consider an arc with horizontal dispersion only, but for full MESA beamline there is also non-zero vertical dispersion which also effects the R_{56} (Eq. (2.50)) required for both the isochronous and non-isochronous recirculation mode of

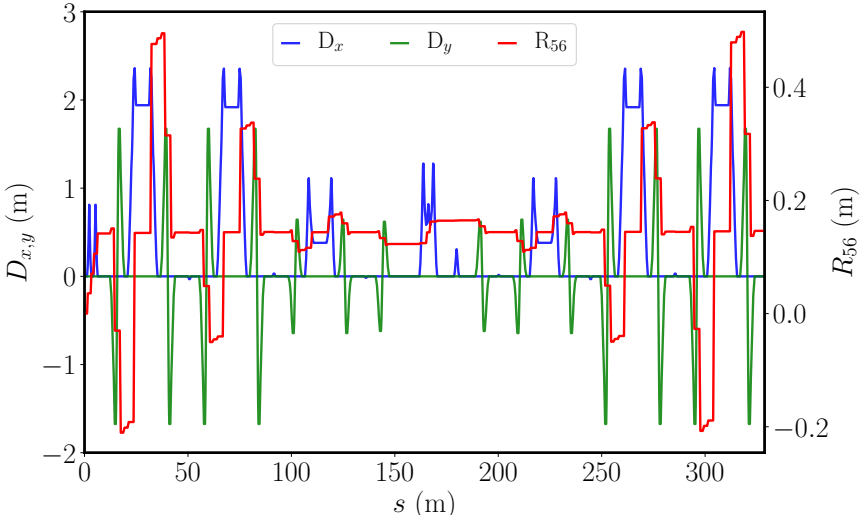

Figure 6.2.: The horizontal dispersion D_x, vertical dispersion D_y, and the momentum compaction R_{56} along the MESA beamline.

MESA. On the other hand, longitudinal space charge together with dispersion can lead to the microbunching instability which strongly depends on the R_{56} and initial uncorrelated energy spread. Thus, it is necessary to study the intensity limitations in MESA due to space charge and microbunching instability.

MESA is designed as a non-isochronous recirculating lattice for better energy stability [77, 78]. It can be seen from Fig. 6.3 that the minimum momentum deviation at the IP within the maximum acceptance limit of momentum deviation 0.5 % [75] is achievable if the beam is injected at low momentum deviation 0.01 % without any chirp or the other case if the beam is injected with initial momentum deviation of 0.4 % with momentum chirp of −7 %. Thus, MESA can flexibly provides the beam parameters for internal target experiments with and without momentum chirp. As concluded in chapter 5 that by accelerating off-crest in the injector linac and adjusting R_{56} in MARC0 successfully works as a bunch compressor including space charge. In the subsequent arcs of MESA, the beam energy is much higher than the MARC0. Thus, space charge effects are weaker and have no intensity limitations due to these effects for large initial deviation. In this chapter, we outline the intensity limitations in the case of small initial deviation.

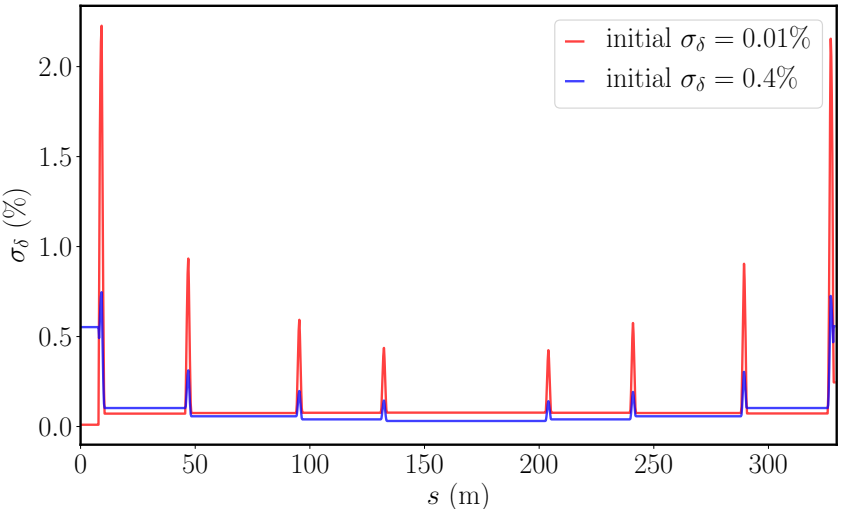

Figure 6.3.: Comparison of momentum deviation σ_δ along the MESA beamline for two different operation modes. In the first case initial momentum deviation is 0.01 % without momentum chirp and second case is with initial momentum deviation of 0.4 % with momentum chirp of −7 %.

6.2 Space Charge in MESA

In this section, the solutions for the beam envelopes and dispersion with space charge along the MESA beamline are presented. Estimation of space charge effects in MESA is done by using the beam matrix approach for a typical set of beam parameters listed in Table 1.1.

Figure 6.4 shows the horizontal and vertical beam envelopes with space charge for I = "zero", 1, 5, and 10 mA in MESA. It can be seen from Fig. 6.5 that with space charge the dispersion is significantly modified for non-zero currents. The sign reversal of D_x and D_y may contribute to the phase mismatch at the entrance of the RF structure due to changes in the time of flight. Also, there appears to be a strong mismatch in the beam envelopes and dispersion near PIT experiment at s = 175 m (as depicted in Fig. 6.1 for 105 MeV beam energy) and in the further arcs. This strong effect of space charge at 105 MeV can be expected from previous chapter results that space charge induces a mismatch

between the beam envelopes and non-zero dispersion at the end of the MARC0 which leads to the strong mismatch in the beam envelopes in the further arcs during acceleration and deceleration and distorts the phase space.

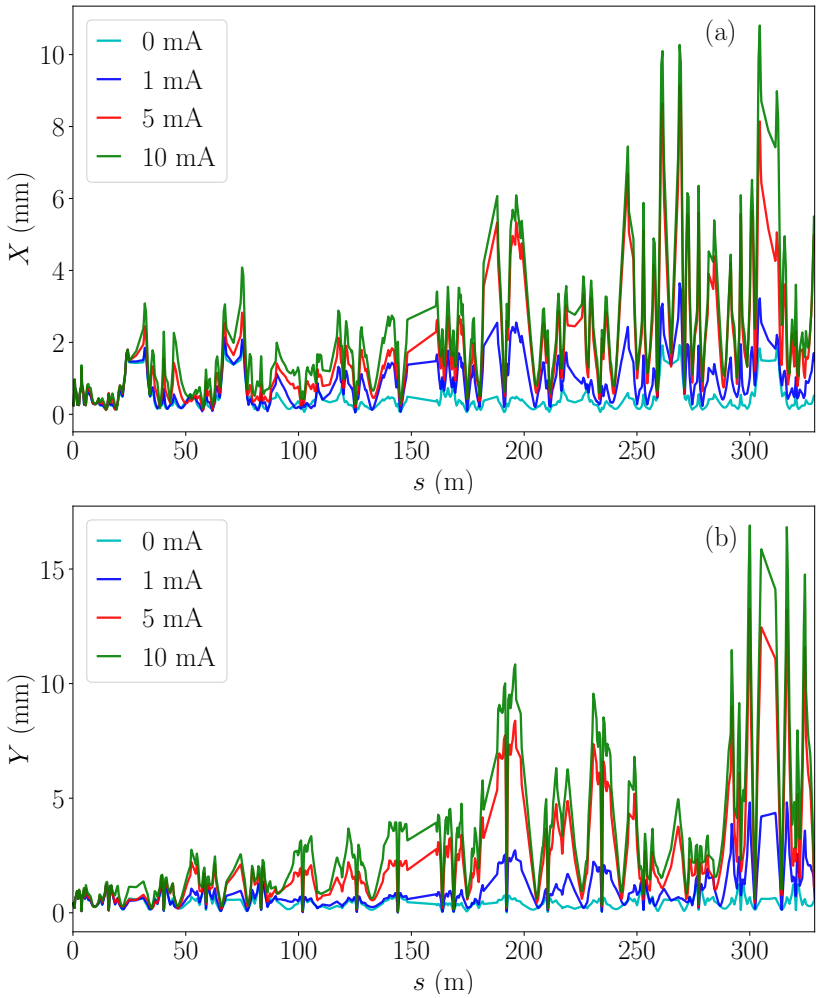

Figure 6.4.: Evolution of (a) horizontal beam envelope, and (b) vertical beam envelope along the MESA beamline for I = 0, 1, 5, 10 mA including transverse and longitudinal space charge.

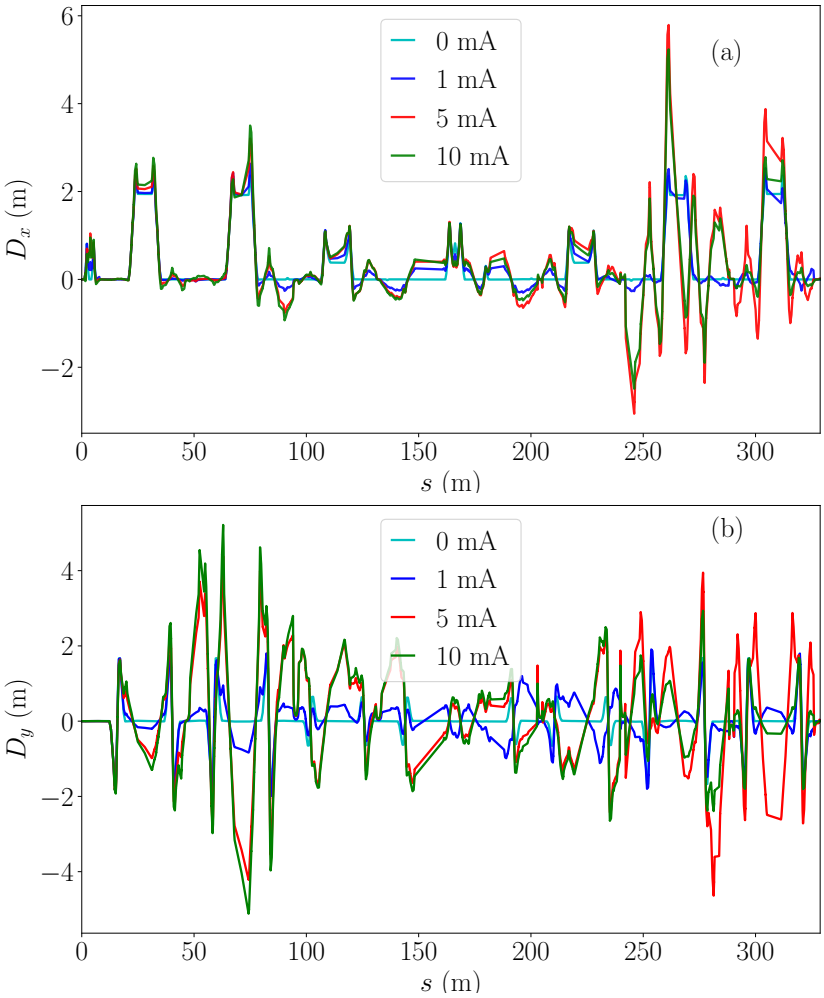

Figure 6.5.: Evolution of (a) horizontal dispersion, and (b) vertical dispersion along the MESA beamline for I = 0, 1, 5, 10 mA including transverse and longitudinal space charge.

Figure 6.6 shows the longitudinal space charge impedance as a function of initial modulation wavelength λ (3D view on the left and 2D top view on the right) along the MESA beamline with space charge for I = "zero", and 10 mA. It

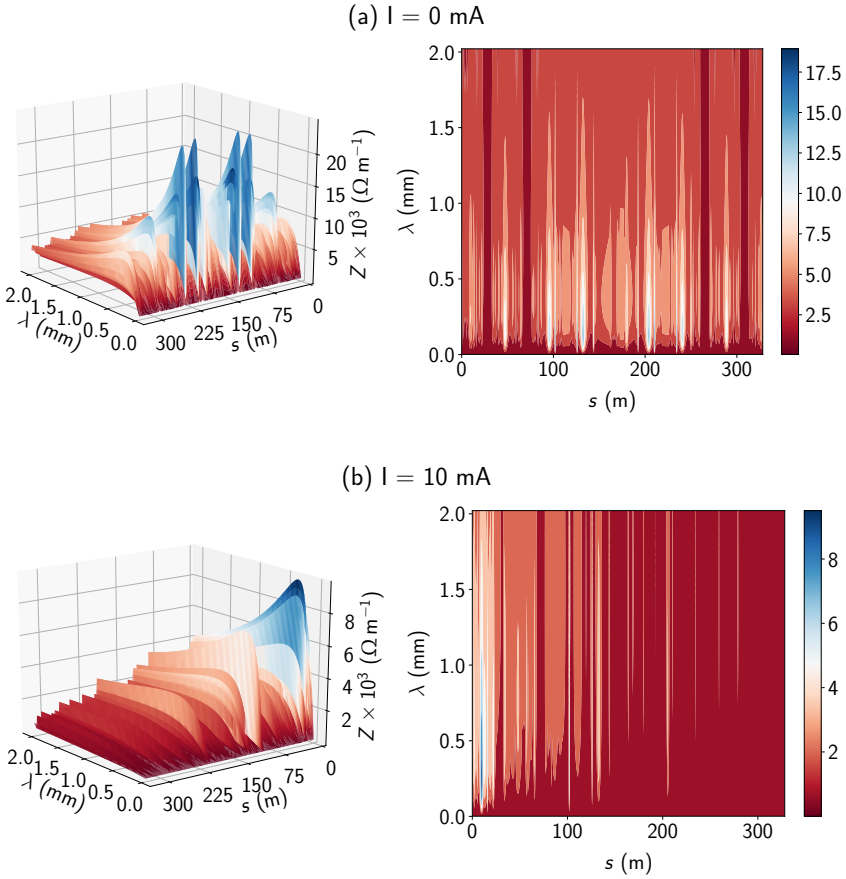

Figure 6.6.: Longitudinal space charge impedance as a function of initial modulation wavelength λ (3D view on the left and 2D top view on the right) for (a) I = "zero" mA, and (b) 10 mA along the MESA beamline.

can be seen from Fig. 6.6 (a) that for "zero" current, longitudinal space charge impedance has the maximum value for initial modulation wavelength range $\lambda = 200-300\,\mu$m at the location of the PIT experiment because beam radius is small there (Eq. (3.31)). On the other hand, as can be seen from Fig 6.6 (b) that

for 10 mA current, impedance has the maximum value for initial modulation wavelength range $\lambda = 100 - 1200\,\mu$m near the injection arc as impedance is inversely proportional to the beam radius and due to space charge beam radius gets larger due to the mismatch of envelopes in the further arcs as shown in Fig 6.4.

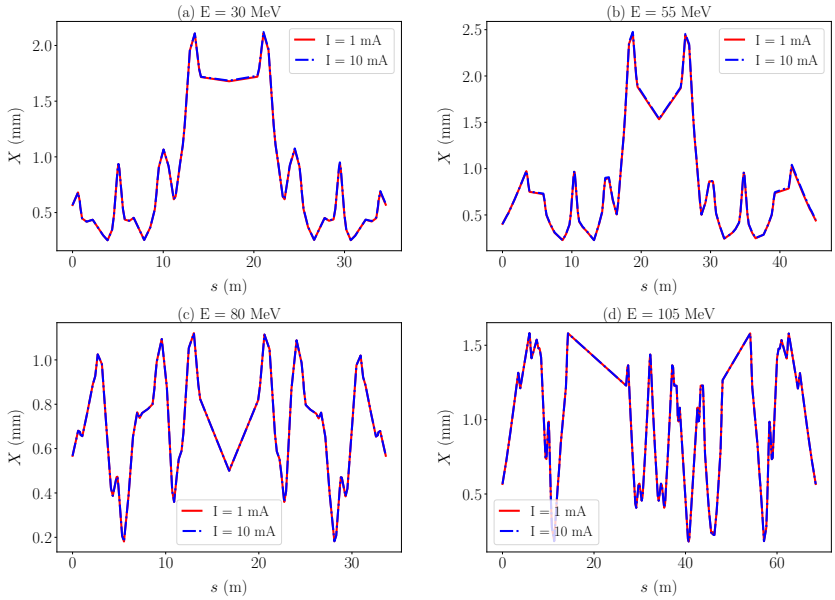

Figure 6.7.: Horizontal beam envelopes along the (a) 30 MeV recirculation arc, (b) 55 MeV recirculation arc, (c) 80 MeV recirculation arc, and (d) 105 MeV internal arc of MESA for I = 1, 10 mA when the beam is matched with space charge in the 5 MeV injection arc MARC0.

The above results show the beam envelopes and dispersion mismatch from the design values due to space charge effects. Thus, to estimate the intensity limitations due to space charge in MESA, first match the beam in the MARC0 using the random walk scheme as discussed in chapter 5, and then track that matched beam through high energy recirculation arcs.

Figure 6.7 shows the horizontal beam envelopes along the 30, 55, 80, and 105 MeV recirculation arcs of MESA for I = 1, 10 mA when the beam is matched with space charge in the MARC0. It can be seen that if all the lattice parameters

of the beamline are matched properly with the subsequent RF structure in the presence of space charge at the injection, there is no mismatch between the beam envelopes due to space charge in the high energy recirculations arcs of MESA. Thus, it can be concluded from space-charge simulations that MESA has no intensity limitations due to space charge if the beam is matched properly with space charge at the injection.

6.3 Microbunching Instability Gain Computation in MESA

The overall microbunching gain for a multi-pass recirculation beamline or a long beamline is computed by an intuitive method in literature [79, 68], where one first compute the instability gain for a single recirculation arc or a sub-beamline section, and then multiply the gain of individual sections to get the total gain. Mathematically, it is written as

$$G_{\text{total}} = \prod_{i=1}^{n} G_i = G_1 G_2 G_3 ... G_n, \tag{6.1}$$

where G_i is the microbunching gain factor for the i^{th} section of the beamline as defined in Eq. (3.28). Note that Eq. (6.1) idea typically comes from the circuit electronics for cascaded systems. The successive multiplication of individual arcs or sub-beamlines gain gives the total microbunching gain G_{total}.

As MESA is a multi-turn machine, we compute the microbunching instability gain due to initial density modulations for the individual arcs using Eq. (3.33) and applying Eq. (6.1) to obtain the total microbunching gain at the beam dump. Figure 6.8 shows the microbunching instability gain spectrum for I = 1 mA and 10 mA at the end of 5, 30, 55, 80, and 105 MeV recirculation arcs of MESA matched with space charge. Using Eq. (6.1), the gain factor for MESA is:

$$G_{\text{total}} = \begin{cases} 1.061 & \text{for I} = 1\,\text{mA} \\ 1.462 & \text{for I} = 10\,\text{mA}. \end{cases} \tag{6.2}$$

It can be seen from Fig 6.8 and Eq. (6.2) that microbunching instability gain is approximately 1 for I = 1 mA and 1.5 for I = 10 mA which is not severe as compare to the high gains in FELs. Thus, we can conclude that there is no microbunching instability in MESA due to space charge for the reference beam parameters listed in Table 1.1 and it has negligible impact on the beam quality.

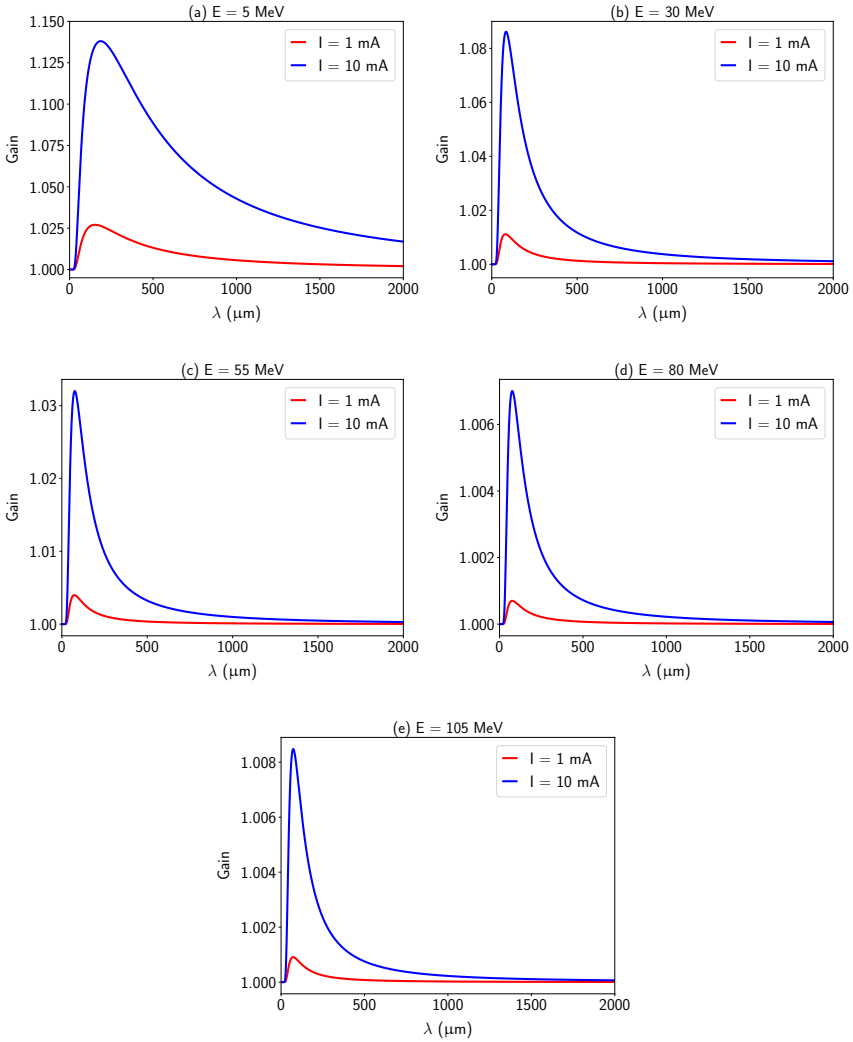

Figure 6.8.: Microbunching gain spectrum for I = 1 mA and 10 mA at the end of (a) 5 MeV injection arc s = 7.51 m, (b) 30 MeV recirculation arc s = 45.3 m, (c) 55 MeV recirculation arc s = 93.751 m, (d) 80 MeV recirculation arc s = 130.65 m, and (e) 105 MeV recirculation arc s = 202.36 m of MESA.

7 Conclusion and Outlook

For intense electron bunches at low to medium energy traversing through bends, it is essential to understand the details of space-charge-induced effects to maintain beam quality throughout the ERL operation. Particularly, current dependent matching of an arc into the subsequent RF structure is essential to preserve beam quality. Previous studies on beam matching with space charge have been discussed mostly in high intensity beams in conventional linacs and synchrotrons. This study concentrates on the analytic estimations and numerical simulations of the space charge effects in ERLs.

The importance of correct beam matching is shown using beam matrix tracking and particle tracking. It is shown how space charge modifies the dispersion function along the arc thereby affecting the momentum compaction which leads to change in the path length of electrons. Momentum compaction needs to be controlled in an ERL to control the bunch length and to avoid the phase mismatch at the RF structure because of changes in path length. In case the arc optics settings are chosen for zero current, then one would end up with a dispersion and bunch length different from the design values at a subsequent RF structure. A "random walk" scheme was employed to get matched parameters with space charge at the subsequent RF structure of an arc. Further, longitudinal space-charge-induced microbunching instability is studied in ERLs, which depends on the details of the dispersion function along the arcs.

For a qualitative analysis, analytic expressions for the beam radius, dispersion, and momentum compaction within the smooth approximation were obtained. Further, an analytical expression for the momentum deviation with space charge was obtained, under the assumption of slowly varying momentum compaction along an arc. The analytical models, beam matrix tracking results, and particle tracking simulations are compared using a low energy injection arc of MESA. The beam matrix approach and particle tracking simulations show good agreement. The results agree well with analytical predictions, although in this simplified model average values of beam radius, dispersion, and momentum compaction computed by smooth approximation are considered.

The above models are applied to the low energy (5 MeV) injection arc (MARC0) of MESA, which also compresses to a bunch at the start of the subsequent RF structure. These results are compared with simulations done using the beam matrix approach, smooth approximation and ELEGANT particle tracking. It was found that space charge is prominent at low energy during beam injection. It was therefore necessary to include transverse-longitudinal space charge in start-to-end simulations along the MESA beamline. Since precisely adjusted beam envelopes and momentum deviation are a key component of the pseudo internal target experiment, the effect of space charge which can create a global mismatch of beam envelopes at different energies, should be well controlled. In the subsequent recirculation arcs of MESA, the beam energy is much higher than the injection energy. Thus, it was found that space charge effects are weaker. In conclusion, if the beam is matched at the injection, then there is no space charge defocusing in the high-energy arcs. Additionally, investigation of the microbunching instability showed that in the operating range of the accelerator beam parameters of MESA, there is no impact of space-charge-induced microbunching instability in the MESA.

The model of space-charge envelope equations used in this work to predict the dispersion and momentum compaction with space charge is not applicable to the non-relativistic bunches which have shorter length than the beam radius. This is due to the additional occurrence of transverse-longitudinal phenomena in non-relativistic bunches. Another interesting possibility to extend this work is to study the wake field effects in the RF cavities along with beam matching with space charge [80]. Finally, the calculations of dispersion and higher-order momentum compaction with non-linear space charge can be considered and systematically compared with particle-in-cell simulations.

A Space Charge Matrix Formalism

Following the formalism of Refs. [61, 62, 63], consider a uniformly charged ellipsoid representing a bunched beam. The electric field components due to a uniformly charged ellipsoid are as follows:

$$E_x = \frac{1}{4\pi\epsilon_0}\frac{3I\lambda_{\mathrm{rf}}}{c\gamma^2}\frac{1-f}{\sigma_x\left(\sigma_x+\sigma_y\right)\sigma_z}x, \tag{A.1a}$$

$$E_y = \frac{1}{4\pi\epsilon_0}\frac{3I\lambda_{\mathrm{rf}}}{c\gamma^2}\frac{1-f}{\sigma_y\left(\sigma_x+\sigma_y\right)\sigma_z}y, \tag{A.1b}$$

$$E_z = \frac{1}{4\pi\epsilon_0}\frac{3I\lambda_{\mathrm{rf}}}{c}\frac{f}{\sigma_x\sigma_y\sigma_z}z, \tag{A.1c}$$

where σ_x, σ_y, and σ_z are the semi-axes of an ellipsoid, I is the average current over one RF period, λ_{rf} is the free-space RF wavelength, c is speed of light, and ϵ_0 is the permittivity of free space. The form factor f is the function of $p = \frac{\gamma\sigma_z}{\sqrt{\sigma_x\sigma_y}}$ given as [81]

$$f\left(p\right) = \begin{cases} \frac{1}{1-p^2} - \frac{p}{\left(1-p\right)^{3/2}}\cos^{-1}p & \text{if } p<1, \\ \frac{p\cosh^{-1}p}{\left(p^2-1\right)^{3/2}} - \frac{1}{\left(p^2-1\right)} & \text{if } p>1, \\ \frac{1}{3} & \text{if } p=1, \end{cases} \tag{A.2}$$

where $\cosh^{-1}p = ln\left(p+\sqrt{p^2+1}\right)$.

The space charge is implemented in the kick approximation as a change in the normalized momentum components as the beam traverse Δs distance is

$$\Delta\left(\beta\gamma\right)_u = \frac{qE_u\Delta s}{\beta mc^2},$$

where u denotes x, y, or z, and m is the electron rest mass. This formulation is valid as long as the ellipsoid is upright with respect to local coordinate system as explained in Ref. [62]. The transfer matrix R^{sc} for the space-charge kick:

$$R^{\mathrm{sc}} = \begin{pmatrix} 1 & 0 & 0 & 0 & 0 & 0 \\ \Delta s/f_{\mathrm{sc},x} & 1 & 0 & 0 & 0 & 0 \\ 0 & 0 & 1 & 0 & 0 & 0 \\ 0 & 0 & \Delta s/f_{\mathrm{sc},y} & 1 & 0 & 0 \\ 0 & 0 & 0 & 0 & 1 & 0 \\ 0 & 0 & 0 & 0 & \Delta s/f_{\mathrm{sc},z} & 1 \end{pmatrix}, \tag{A.3}$$

with $\frac{1}{f_{\mathrm{sc},x}} = \frac{qE_x}{\beta mc^2}$, $\frac{1}{f_{\mathrm{sc},y}} = \frac{qE_y}{\beta mc^2}$, and $\frac{1}{f_{\mathrm{sc},z}} = \frac{qE_z}{\beta mc^2}$. Note that step size Δs should be small enough to converge the physical results in the presence of space charge.

Acknowledgement

This dissertation is without doubt the most rewarding project I have ever undertaken. It is also the most fulfilling, and one I could not have completed alone. I have been intensely fortuitous to have had great teachers, mentors, friends, and family to encourage me and I am grateful for their generosity in sharing their knowledge and consistent support.

First, I would like to thank my PhD advisor, Professor Oliver Boine-Frankenheim. I have been fortunate to have an advisor who gave me the freedom to explore on my own and at the same time the guidance to recover when my steps faltered. He taught me how to question thoughts and express ideas. His patience and support helped me overcome many critical situations and finish this dissertation. I shall always hold him as a standard for maintaining the precise balance of professionalism with candour. My second advisor, Professor Kurt Aulenbacher, has always been happy to provide mentorship, advice, and guidance. I'm also thankful for his thorough editing of my papers, which helped my work to shape well. I would also like to thank Professor Irina Munteanu for supporting me through my teaching duties.

If this dissertation had a second author, it would have to be Christian Stoll. As my graduate school colleague, internship-project partner, and a good friend who helped me to solve every kind of problem on telegram, Christian has had a sight in every aspect of the work presented here. His work has been an amazing compliment to my own, ensuring that all our joint efforts for lattice design/optimization were ready and optimized for success.

My heartiest gratitude goes to my TEMF and AccelencE colleagues for providing a nice working environment. During these years at TEMF, I have had the privilege of working with wonderful and helpful people, especially thanks to fellows from office no. 217, Rado, Will, Dalyana and Daria for listening endless distressing stories.

I would like to thank Uwe Niedermayer and Florian Hug for their valuable edits, comments, and feedback on my work. I would like to acknowledge Sabrina Appel from GSI for her support to resolve technical glitches at the very initial stage of my project. I am also thankful to Christian, Erika, Nipun, and Saurabh for constructive criticism and proofreading of this dissertation

by pointing out subtle details. I am also grateful for the financial support provided by DFG through GRK 2128 Accelence project D-3 to study the effect of space charge and wake fields in MESA.

Last and most importantly, I thank all my friends and family who have continually supported and encouraged me. Thank you to my longest, unwavering supporters: my parents Aziz and Nazreena, my brother Salik, my sisters Ravia and Diya, my niece Innaya and my besties Nipun, Payal, and the RARARAA. In addition, to my friends who have kept me sane: Sunpreet, Raman, Pranjal for philosophical discussions, "Original Darmstadt Family" group, and all other amazing and admiring people. I am lucky to have you all.

List of Symbols

An arrow denotes a vector quantity. x and y in the subscript denote the horizontal and the vertical components of a physical quantity, respectively. Note that this list of symbols only specifies the most important ones.

Term	Unit	Description
a, b	m	Average effective rms beam radii
$\vec{A}$	Vs/m	Vector potential
α_x, α_y	rad	Alpha functions
$\vec{B}$	T	Magnetic flux density
$B\rho$	Tm	Magnetic rigidity
b_0		Bunching factor
β, γ		Relativistic factors
β_x,β_y	m	Beta functions
c	m/s	Speed of light in vacuum
$\chi_{x\sigma_\delta}$, $\chi_{y\sigma_\delta}$		Space charge intensity parameter
D_x,D_y	m	Dispersion functions
d_m		Amplitude of density modulations
δ		Fractional momentum deviation
E	MeV	Total beam energy
E_rf	V/m	Peak RF electric field
e	C	Electron charge
ΔE	MeV	Energy gain
ϵ	m rad	RMS emittance
$\vec{F}$	N	Force
G		Microbunching insatbility gain
γ_E		Euler's constant
γ_x,γ_y	1/m	Gamma functions
h	1/m	Momentum chirp
I	A	Beam current
η		Phase slip factor
J	m	Action variable
K_sc		Transverse space charge perveance

Term	Unit	Description
K_l		Longitudinal space charge perveance
κ	$1/\mathrm{m}^2$	Focusing strength
L	m	Length of the arc
λ_r	$1/\mathrm{m}^2$	Transverse uniform particle density
$\lambda(r)$	C/m	Linear charge density
λ_{rf}	m	RF wavelength
m	kg	Rest mass of the particle
N		Total number of particles in a bunch
n		An integer
ω_{rf}	rad	RF angular frequency
$\vec{p}$	kg m/s	Particle momentum
ϕ	rad	RF phase
ϕ_{s}	rad	Synchronous particle phase
ϕ_x	rad	Phase advance
Ψ	$1/\mathrm{m}^3$	Particle density function
q	C	Particle charge
R		Transport matrix
R_{56}	m	Momentum compaction
r_{b}	m	Beam radius
r_{e}	m	Classical electron radius
r_{p}	m	Pipe radius
ρ	m	Bending radius
σ_δ		RMS momentum deviation
$\sigma_{x,y}$	m	RMS betatron amplitude
σ_z	m	RMS half bunch length
Σ		Second moments of the beam distribution
T	s	Time of flight of particles
$u_{i,j}$		Canonical Variables
$\vec{v}$	m/s	Velocity of the particle
X, Y	m	Effective rms beam radii
x_β	m	Betatron oscillation amplitude
$x_{\mathrm{sc},\beta}$	m	Betatron oscillation amplitude with space charge
Z	Ω	Longitudinal space charge impedance
Z_0	Ω	Free space impedance
z_{m}	m	half bunch length

List of Acronyms

BERLinPro Berlin Energy Recovery Linac Project.

CBETA Cornell-BNL ERL Test Accelerator.

cERL Compact Energy Recovery Linac.

CERN Conseil Européen pour la Recherche Nucléaire.

CW Continuous Wave.

DBA Double Bend Achromat.

EB External Beam.

ELEGANT ELEectron Generation ANd Tracking.

ER Energy Recovery.

ERL Energy Recovery Linac.

FEL Free Electron Laser.

FFT Fast Fourier Transformation.

IP Interaction Point.

IR Infrared.

JAEA Japan Atomic Energy Agency.

JLab Jefferson Laboratory.

KV Kapchinsky-Vladimirsky.

LINAC Linear Accelerator.

L-O Lee-Okamoto.

MAD Methodical Accelerator Design.

MARC0 MESA Arc0.

MAMBO MilliAMpere BOoster.

MESA Mainz Energy-recovering Superconducting Accelerator.

PERLE Powerful Energy Recovery Linac for Experiments.

PIT Pseudo-Internal Target.

PS Proton Synchrotron.

RF Radio Frequency.

RMS Root Mean Square.

SDDS Self Describing Data Sets.

SRF Superconducting Radio Frequency.

TM Transverse Magnetic.

V-R Venturini-Reiser.

List of Figures

List of Tables

Bibliography

[1] S.-Y. Lee, *Accelerator physics*. World scientific publishing, 2018. 1

[2] T. P. Wangler, *RF Linear accelerators*. John Wiley & Sons, 2008. 1, 21, 27, 29, 34, 36, 61

[3] L. Merminga, D. R. Douglas, and G. A. Krafft, "High-current energy-recovering electron linacs," *Annual Review of Nuclear and Particle Science*, vol. 53, no. 1, pp. 387–429, 2003. 2, 4

[4] K. Aulenbacher, "Opportunities for parity violating electron scattering experiments at the planned MESA facility," *Hyperfine Interactions*, vol. 200, no. 1-3, pp. 3–7, 2011. 2, 6, 76

[5] S. M. Gruner and D. H. Bilderback, "Energy recovery linacs as synchrotron light sources," *Nuclear Instruments and Methods in Physics Research, Section A: Accelerators, Spectrometers, Detectors and Associated Equipment*, vol. 500, no. 1-3, pp. 25–32, 2003. 2

[6] S. Smith, "ERL 2015," in *56th ICFA Advanced Beam Dynamics Workshop on Energy Recovery Linacs (ERL'15)*, 2015. 2, 4

[7] A. Khan, O. Boine-Frankenheim, F. Hug, and C. Stoll, "Beam matching with space charge in energy recovery linacs," *Nuclear Instruments and Methods in Physics Research Section A: Accelerators, Spectrometers, Detectors and Associated Equipment*, vol. 948, p. 162822, 2019. 2, 5, 26, 63

[8] E. L. Saldin, E. A. Schneidmiller, and M. Yurkov, "Longitudinal space charge-driven microbunching instability in the tesla test facility linac," in *Free Electron Lasers 2003*, pp. 355–359, Elsevier, 2004. 2, 5

[9] A. Khan, O. Boine-Frankenheim, and C. Stoll, "Space charge and microbunching studies for the injection arc of MESA," *Journal of Physics: Conference Series*, vol. 1067, no. 6, 2018. 2

[10] M. Tigner, "A possible apparatus for electron clashing-beam experiments," *Il Nuovo Cimento (1955-1965)*, vol. 37, no. 3, pp. 1228–1231,

1965. 2

[11] A. Arnold and J. Teichert, "Overview on superconducting photoinjectors," *Physical Review Special Topics-Accelerators and Beams*, vol. 14, no. 2, p. 024801, 2011. 4

[12] S. Ramberger, M. Draper, and V. R. W. Schaa, eds., *Proceedings, 59th ICFA Advanced Beam Dynamics Workshop on Energy Recovery Linacs, ERL2017*, (JACoW), Geneva, Switzerland, Geneva, Switzerland, 2018. 4

[13] S. Sakanaka, "ERL 2013," in *Proceedings of the 53th ICFA Advanced Beam Dynamics Workshop on Energy Recovery Linacs, ERL-2013, Novosibirsk, Russia, 2013*, 2013. 4

[14] S. Smith, B. Muratori, H. Owen, G. Hoffstaetter, V. Litvinenko, I. Ben-Zvi, M. Bai, J. Beebe-Wang, M. Blaskiewicz, R. Calaga, *et al.*, "Optic issues in ongoing ERL projects," *Nuclear Instruments and Methods in Physics Research Section A: Accelerators, Spectrometers, Detectors and Associated Equipment*, vol. 557, no. 1, pp. 145–164, 2006. 4

[15] D. Douglas, "Design considerations for recirculating and energy recovering linacs," *JLAB-TN-00-027*, 2000. 4

[16] K. Aulenbacher, J. Diefenbach, F. Fichtner, S. Friederich, R. Heine, C. Matejcek, F. Schlander, and D. Simon, "Elementary design report for the Mainz Energy Recovering Superconducting Accelerator MESA," tech. rep., internal report, 2014. 4, 8

[17] D. Angal-Kalinin, G. Arduini, B. Auchmann, J. Bernauer, A. Bogacz, F. Bordry, S. Bousson, C. Bracco, O. Brüning, R. Calaga, *et al.*, "PERLE: Powerful energy recovery linac for experiments conceptual design report," *Journal of Physics G: Nuclear and Particle Physics*, vol. 45, no. 6, p. 065003, 2018. 4

[18] A. Jankowiak, M. Abo-Bakr, and A. Matveenko, "Beam dynamics of energy recovery linacs," *CERN Yellow Reports: School Proceedings*, vol. 1, p. 439, 2018. 4

[19] J.-G. Hwang, E.-S. Kim, and T. Miyajima, "Effects of space charge in a compact superconducting energy recovery linac with a low energy," *Nuclear Instruments and Methods in Physics Research Section A: Accelerators, Spectrometers, Detectors and Associated Equipment*, vol. 684, pp. 18–26, 2012. 5, 35

[20] B. Muratori, C. Gerth, and N. Vinokurov, "Space charge effects for the ERL prototype at Daresbury Laboratory," in *Proceedings of EPAC04*, 2004. 5

[21] S. Heifets, G. Stupakov, and S. Krinsky, "Coherent synchrotron radiation instability in a bunch compressor," *Physical Review Special Topics-Accelerators and Beams*, vol. 5, no. 6, p. 064401, 2002. 5

[22] M. Borland, "Modeling of the microbunching instability," *Physical Review Special Topics-Accelerators and Beams*, vol. 11, no. 3, p. 030701, 2008. 5, 43, 55

[23] E. L. Saldin, E. A. Schneidmiller, and M. Yurkov, "Klystron instability of a relativistic electron beam in a bunch compressor," *Nuclear Instruments and Methods in Physics Research Section A: Accelerators, Spectrometers, Detectors and Associated Equipment*, vol. 490, no. 1-2, pp. 1–8, 2002. 5

[24] Z. Huang and K.-J. Kim, "Formulas for coherent synchrotron radiation microbunching in a bunch compressor chicane," *Physical Review Special Topics-Accelerators and Beams*, vol. 5, no. 7, p. 074401, 2002. 5, 45

[25] Z. Huang, M. Borland, P. Emma, J. Wu, C. Limborg, G. Stupakov, and J. Welch, "Suppression of microbunching instability in the linac coherent light source," *Physical Review Special Topics-Accelerators and Beams*, vol. 7, no. 7, p. 074401, 2004. 5, 46, 47, 48, 55

[26] Z. Huang, J. Wu, T. Shaftan, *et al.*, "Microbunching instability due to bunch compression," *ICFA beam dynamics newsletter*, vol. 38, no. SLAC-PUB-11597, 2005. 5, 44, 46

[27] M. Borland, "User 's manual for ELEGANT," 2006. 5, 36, 51, 53, 54, 55, 56, 63

[28] K. Aulenbacher and A. Jankowiak, "Polarized electrons and positrons at the MESA accelerator," in *Polarized Sources, Targets And Polarimetry*, pp. 45–53, World Scientific, 2011. 5

[29] K. Aulenbacher, R. Heine, and R. Eichhorn, "MESA-Sketch of an energy recovery linac for nuclear physics experiments at Mainz," in *Conf. Proc. IPAC-2012-TUPPR073*, vol. 1205201, pp. 1993–1995, 2012. 5, 81

[30] A. Khan, K. Aulenbacher, and O. Boine-Frankenheim, "Study of microbunching instability in MESA," in *59th ICFA Advanced Beam Dynamics Workshop on Energy Recovery Linacs (ERL'17)*, 2018. 5, 34, 43, 81

[31] J. Teichert, A. Büchner, H. Büttig, F. Gabriel, P. Michel, K. Möller, U. Lehnert, C. Schneider, J. Stephan, and A. Winter, "RF status of superconducting module development suitable for CW operation: ELBE cryostats," *Nuclear Instruments and Methods in Physics Research Section A: Accelerators, Spectrometers, Detectors and Associated Equipment*, vol. 557, no. 1, pp. 239–242, 2006. 6

[32] D. Becker, R. Bucoveanu, C. Grzesik, and et al., "The P2 experiment," *The European Physical Journal A*, vol. 54, p. 208, Nov 2018. 6

[33] A. Denig, "Recent results from the Mainz Microtron MAMI and an outlook for the future," *AIP Conf. Proc.*, vol. 1735, p. 020006, 2016. 6

[34] W. Andrzej, *Beam dynamics in high energy particle accelerators*. World Scientific, 2014. 12, 13, 16, 17, 18, 37, 38, 40, 42

[35] H. Wiedemann, *Particle accelerator physics*. Springer, 2015. 13, 17, 18, 33, 75

[36] M. Reiser, *Theory and design of charged particle beams*. John Wiley & Sons, 2008. 23, 27, 29, 37, 39, 40, 42, 61, 63

[37] M. Venturini and M. Reiser, "Self-consistent beam distributions with space charge and dispersion in a circular ring lattice," *Physical Review E*, vol. 57, no. 4, p. 4725, 1998. 23

[38] M. Dohlus, T. Limberg, and P. Emma, "Bunch compression for linac-based FELs," *ICFA Beam Dynamics Newsletter*, vol. 38, pp. 15–50, 2005. 30

[39] D. C. Nguyen, J. W. Lewellen IV, and L. D. Duffy, "RF linac for high-gain fel bunch compression," tech. rep., Los Alamos National Lab.(LANL), Los Alamos, NM (United States), 2014. 30

[40] R. C. Davidson, *Physics of nonneutral plasmas*. World Scientific Publishing Company, 2001. 34

[41] D. J. Griffiths, "Introduction to electrodynamics," 2005. 34, 35

[42] F. J. Sacherer, "Rms envelope equations with space charge," *IEEE Transactions on Nuclear Science*, vol. 18, no. 3, pp. 1105–1107, 1971. 36, 41, 51

[43] I. Kapchinskij and V. Vladimirskij, "Limitations of proton beam current in a strong focusing linear accelerator associated with the beam space charge," *Proceedings of the International Conference on High Energy Accel-*

erators and Instrumentation, p. 274, 1959. 36

[44] D. Neuffer, "Longitudinal motion in high current ion beams-a self-consistent phase space distribution with an envelope equation," *IEEE Transactions on Nuclear Science*, vol. 26, no. 3, pp. 3031–3033, 1979. 37, 42, 63, 68

[45] O. D. Kellogg, *Foundations of potential theory*, vol. 31. Courier Corporation, 1953. 39

[46] M. Venturini and M. Reiser, "Self-consistent beam distributions with space charge and dispersion in a circular ring lattice," *Physical Review E - Statistical Physics, Plasmas, Fluids, and Related Interdisciplinary Topics*, vol. 57, no. 4, pp. 4725–4732, 1998. 41, 61, 62

[47] S.-Y. Lee and H. Okamoto, "Space-charge dominated beams in synchrotrons," *Physical review letters*, vol. 80, no. 23, p. 5133, 1998. 41, 61, 62

[48] M. Venturini, R. A. Kishek, and M. Reiser, "The problem of dispersion matching in space charge dominated beams," in *Particle Accelerator Conference, 1999. Proceedings of the 1999*, vol. 5, pp. 3274–3276, IEEE, 1999. 41

[49] H. Okamoto and S. Machida, "Particle beam resonances driven by dispersion and space charge," *Nuclear Instruments and Methods in Physics Research Section A: Accelerators, Spectrometers, Detectors and Associated Equipment*, vol. 482, no. 1-2, pp. 65–78, 2002. 41, 62

[50] S. Bernal, *A Practical Introduction to Beam Physics and Particle Accelerators*. Morgan & Claypool Publishers, 2016. 42

[51] G. Franchetti, I. Hofmann, and G. Rumolo, "Effect of space charge on bunch compression near the transition," *Physical Review Special Topics-Accelerators and Beams*, vol. 3, no. 8, p. 084201, 2000. 42, 63, 69

[52] M. Venturini, "Microbunching instability in single-pass systems using a direct two-dimensional vlasov solver," *Physical Review Special Topics-Accelerators and Beams*, vol. 10, no. 10, p. 104401, 2007. 43

[53] M. Venturini and J. Qiang, "Transverse space-charge induced microbunching instability in high-brightness electron bunches," *Physical Review Special Topics-Accelerators and Beams*, vol. 18, no. 5, p. 054401, 2015. 43

[54] M. Venturini, "USPAS lecture notes of linear accelerator design for free electron lasers," June 2015. 46

[55] E. Saldin, E. Schneidmiller, and M. Yurkov, "An analytical description of longitudinal phase space distortions in magnetic bunch compressors," *Nuclear Instruments and Methods in Physics Research Section A: Accelerators, Spectrometers, Detectors and Associated Equipment*, vol. 483, no. 1-2, pp. 516–520, 2002. 46

[56] M. Venturini, "Models of longitudinal space-charge impedance for microbunching instability," *Physical Review Special Topics-Accelerators and Beams*, vol. 11, no. 3, p. 034401, 2008. 46, 47, 48

[57] R. Ryne, C. Mitchell, J. Qiang, B. Carlsten, and N. Yampolsky, "Large scale simulation of synchrotron radiation using a Lienard-Wiechert approach," *Proc. IPAC*, 2012. 46

[58] J. D. Jackson, *Classical electrodynamics*. AAPT, 1999. 46, 47

[59] I. Hofmann, "Filamentation of phase space and coherent noise for beams injected into storage rings," *Part. Accel.*, vol. 34, no. GSI-89-32, pp. 211–220, 1989. 47

[60] L. Deniau, H. Grote, G. Roy, and F. Schmidt, "User's reference manual MAD-X," 2018. 51

[61] T. Ohkawa and M. Ikegami, "Dispersion matching at the injection from a high-intensity linac to a circular accelerator," *Nuclear Instruments and Methods in Physics Research Section A: Accelerators, Spectrometers, Detectors and Associated Equipment*, vol. 576, no. 2-3, pp. 274–286, 2007. 51, 52, 62, 93

[62] K. R. Crandall, "Trace 3-D documentation," tech. rep., Los Alamos National Lab, 1987. 51, 52, 93, 94

[63] C. K. Allen and N. Pattengale, "Theory and technique of beam envelope simulation," *Los Alamos National Laboratory Internal Report LA-UR-02-4979*, 2002. 51, 52, 93

[64] S. Vakili and Q. Zhao, "A random walk approach to first-order stochastic convex optimization," *arXiv preprint arXiv:1901.05947*, 2019. 53

[65] M. Borland, "A universal postprocessing toolkit for accelerator simulation and data analysis," tech. rep., Argonne National Lab., 1998. 53

[66] M. Bassetti and G. Erskine, "CERN-ISR-TH/80-06," *CERN Report, Geneva*, 1980. 54

[67] A. Xiaot, M. Borland, L. Emery, Y. Wang, and K. Y. Ng, "Direct space-charge calculation in ELEGANT and its application to the ILC damping ring," in *2007 IEEE Particle Accelerator Conference (PAC)*, pp. 3456–3458, IEEE, 2007. 54, 71

[68] C. Tsai, "Investigation of microbunching instabilities in modern recirculating accelerators," tech. rep., Thomas Jefferson National Accelerator Facility, Newport News, VA (United States), 2017. 55, 89

[69] M. Borland, "Controlling noise and choosing binning parameters for reliable csr and lsc simulation in elegant," tech. rep., Report No. OAG-TN-2005-027, 2005. 55, 56

[70] J. Barnard, F. Deadrick, A. Friedman, D. Grote, L. Griffith, H. Kirbie, V. Neil, M. Newton, A. Paul, W. Sharp, *et al.*, "Recirculating induction accelerators as drivers for heavy ion fusion," *Physics of Fluids B: Plasma Physics*, vol. 5, no. 7, pp. 2698–2706, 1993. 61

[71] S. Bernal, B. Beaudoin, T. Koeth, and P. G. O'Shea, "Smooth approximation model of dispersion with strong space charge for continuous beams," *Physical Review Special Topics - Accelerators and Beams*, vol. 14, no. 10, pp. 1–15, 2011. 62, 63, 65

[72] M. Ikegami, S. Machida, and T. Uesugi, "Particle-core analysis of dispersion effects on beam halo formation," *Physical Review Special Topics-Accelerators and Beams*, vol. 2, no. 12, p. 124201, 1999. 62, 65

[73] K. Hanke, J. Sanchez-Conejo, and R. Scrivens, "Dispersion matching of a space charge dominated beam at injection into the CERN PS Booster," *Proceedings of the 2005 Particle Accelerator Conference*, 2005. 62, 64

[74] S. Appel and O. Boine-Frankenheim, "Microbunch dynamics and multistream instability in a heavy-ion synchrotron," *Physical Review Special Topics-Accelerators and Beams*, vol. 15, no. 5, p. 054201, 2012. 63

[75] F. Hug and R. Heine, "Injector linac stability requirements for high precision experiments at MESA," *Journal of Physics: Conference Series*, vol. 874, no. 1, p. 012012, 2017. 66, 76, 77, 83

[76] D. Simon, K. Aulenbacher, R. Heine, and F. Schlander, "Lattice and Beam Dynamics of the Energy Recovery Mode of the Mainz Energy-Recovering

Superconducting Accelerator MESA," *Proceedings of the 6th International Particle Accelerator Conference*, pp. 220–222, 2015. 75, 76

[77] H. Herminghaus, "The polytron as a cw electron accelerator in the 10 GeV range," *Nuclear Instruments and Methods in Physics Research Section A: Accelerators, Spectrometers, Detectors and Associated Equipment*, vol. 305, no. 1, pp. 1–9, 1991. 83

[78] H. Herminghaus, "On the inherent stability of non-isochronous recirculating accelerators," *Nuclear Instruments and Methods in Physics Research Section A: Accelerators, Spectrometers, Detectors and Associated Equipment*, vol. 314, no. 1, pp. 209–211, 1992. 83

[79] E. Schneidmiller and M. Yurkov, "Using the longitudinal space charge instability for generation of vacuum ultraviolet and x-ray radiation," *Physical Review Special Topics-Accelerators and Beams*, vol. 13, no. 11, p. 110701, 2010. 89

[80] G. H. Hoffstaetter and Y. H. Lau, "Compensation of wakefield-driven energy spread in energy recovery linacs," *Physical Review Special Topics-Accelerators and Beams*, vol. 11, no. 7, p. 070701, 2008. 92

[81] D. Raparia, J. Alessi, Y. Lee, and W. Weng, "Achromat with linear space charge for bunched beams," in *AIP Conference Proceedings*, vol. 448, pp. 271–277, 1998. 93

Aamna Khan

khan@temf.tu-darmstadt.de
https://www.linkedin.com/in/aamna-khan-943991150/

Education

- October 2019 – present: **PostDoc, TEMF, TU Darmstadt**
  Beam Dynamics of Dielectric Laser Accelerators
- October 2016 – October 2019: **Ph.D, TEMF, TU Darmstadt** in Accelerator Physics.
  Thesis title: *Space Charge Effects in Energy Recovery Linacs*
- September 2017: **Advanced CERN Accelerator School, Royal Holloway, University of London, London**
- June 2014 – June 2016: **M.Sc Physics, Indian Institute of Technology Roorkee, India**
  Thesis title: *Analysis of Multipacting in a Pill Box Cavity*
  CGPA: 8.156
- January 2016 – February 2016: **US Particle Accelerator School "Applied Electromagnetism: Magnet and RF-Cavity Design", UT Austin, USA**
  Grade: Outstanding
- May 2011– May 2014: **B.Sc (Hons) Physics, Panjab University Chandigarh, India**
  CGPA: 9.1 (Gold Medalist)

Academic Projects

- October 2016 – present: **Research Assistant at TEMF, TU Darmstadt, Germany**
- September 2017 – December 2017: **Internship at KPH, Johannes Gutenberg University of Mainz, Germany**
- October 2016 – October 2018: **Teaching Assistant at TEMF, TU Darmstadt, Germany**
- July 2015 – May 2016: **Master's Thesis at IIT Roorkee, India**
- May 2015 – June 2015: **Summer internship at IIT Roorkee, India**

Skills

- Accelerator Physics Codes: ELEGANT, MAD-X, CST, FEMM 2D, Superfish.
- Programming: Python, Fortran, C, MATLAB, Mathematica, LaTeX.
- Designing Softwares: Adobe Photoshop, Origin, Microsoft PowerPoint, Ipe
- Languages: English (Professional proficiency), Hindi/Punjabi (Native proficiency), German (Elementary proficiency).

Fellowships and Awards

- April 2018: **European Physical Society (EPS) student grant** to attend 9^{th} International Particle Accelerator Conference (IPAC18), Vancouver, Canada.
- October 2017: **Best poster award**, Wilhelm Und Else Heraeus-Stiftung Physics of Energy-Recovery Linacs, Germany.
- 2016: **US particle accelerator school (USPAS) fellowship**, University of Texas, Austin.
- June 2014 – June 2016: **Central wakf council scholarship** to top 0.1% students in the batch and to consider science as a career, Government of India, India.
- 2014: **Gold medalist**, Panjab University Chandigarh, India.
- 2011–2016: **5 year Merit Scholarship** from Punjab School Education Board Mohali, India. Ranked in top 0.1% students in Punjab.

Research Publications

Journal Articles

1. Khan, A., Boine-Frankenheim, O., Hug, F., & Stoll, C. (2019). Beam matching with space charge in energy recovery linacs. *Nuclear Instruments and Methods in Physics Research Section A: Accelerators, Spectrometers, Detectors and Associated Equipment*, *948*, 162822.
2. Khan, A., Boine-Frankenheim, O., & Stoll, C. (2018). Space charge and microbunching studies for the injection arc of MESA. *Journal of Physics: Conference Series*, *1067*(6). doi:10.1088/1742-6596/1067/6/062022

Conference Proceedings

1. Khan, A., Aulenbacher, K., & Boine-Frankenheim, O. (2019). Dispersion matching with space charge in mesa. ERL19 proceedings.
2. Khan, A., Aulenbacher, K., & Boine-Frankenheim, O. (2018). Study of microbunching instability in MESA. In *59th ICFA advanced beam dynamics workshop on energy recovery linacs (ERL'17)*.